DEVELOPMENT OF A CONDENSED PHASE VELOCITY MAP IMAGING APPARATUS: DISSOCIATION PHOTODYNAMICS OF NITROGEN DIOXIDE AT 355 NM

by

Stephen W. C. Walker

A thesis submitted to the Department of Chemistry

In conformity with the requirements for

the degree of Doctor of Philosophy

Queen's University

Kingston, Ontario, Canada

(August, 2016)

Abstract

The photochemistry of the polar regions of Earth, as well as the interstellar medium, is driven by the effect of ultraviolet radiation on ice surfaces and on the materials trapped within them. While the area of ice photochemistry is vast and much research has been completed, it has only recently been possible to study the dynamics of these processes on a microscopic level. One of the leading techniques for studying photoreaction dynamics is Velocity Map Imaging (VMI). This technique has been used extensively to study several types of reaction dynamics processes. Although the majority of these studies have utilized molecular beams as the main medium for reactants, new studies showed the versatility of the technique when applied to molecular dynamics of molecules adsorbed on metal surfaces. Herein the development of a velocity map imaging apparatus capable of studying the photochemistry of condensed phase materials is described. The apparatus is used to study of the photo-reactivity of NO_2 condensed within argon matrices to illustrate its capabilities. A doped ice surface is formed by condensing Ar and NO_2 gas onto a sapphire rod which is cooled using a helium compressor to 20 K. The matrix is irradiated using an Nd:YAG laser at 355 nm, and the resulting NO fragment is state-selectively ionized using an excimer-pumped dye laser. In all, we are able to detect transient photochemically generated species and can collect information on their quantum state and kinetic energy distribution. It is found that the REMPI spectra changes as different sections of the dissociating cloud are probed. The rotational and translational energy populations are found to be bimodal with a low temperature component roughly at the temperature of the matrix, and a second component with much higher temperature, the rotational temperature showing a possible population inversion, and the translational temperature of 100-200 K.

The low temperature translational component is found to dominate at long delay times between dissociation and ionization, while at short time delays the high temperature component plays a larger role. The velocity map imaging technique allows for the detection of both the axial and radial components of the translational energy. The distribution of excess energy over the rotational, electronic and translational states of the NO photofragments provides evidence for collisional quenching of the fragments in the Ar-matrix prior to their desorption.

Acknowledgements

I would like to start by thanking my supervisor Dr. Hans-Peter Loock, his tireless efforts for all of his graduate students is inspiring. He enabled me to grow as a scientist by getting me to present at several conferences and to work abroad. His help has made me a better writer and I could not have finished this thesis without his guidance.

I would like to thank my supervisory committee, Dr. R. Oleschuk and Dr. J. H. Horton for all of their helpful thoughts and discussions. I would also like to thank my internal readers and my examining committee. And I would like to thank all of my chemistry teachers throughout the years. Dr. Mark Parnis, my MSc supervisor, who taught me much about life as well as chemistry. I would also like to thank Dr. Scott Hopkins and Dr. Terry McMahon, with whom I have had several interesting conversations.

Of course, I could not have completed this thesis without the help of all of my friends and colleagues in the Loock lab. Specifically, I feel I must mention Mr. Jeff Crouse and Dr. Jack Barnes whose helpful discussions and assistance in building the apparatus made this project a reality. A big thank you goes to all other members past and present of the Loock lab who didn't directly work on the VMI project but whose helpful discussions were invaluable. Additionally, I would like to thank all of the students in the Hopkins group for letting me bounce ideas off them.

Finally, I would like to thank my family. My parents' dedication to working hard has always been an inspiration and my sister Kate for all of your friendly advice over the years. My dad, thank you for reading over parts of this thesis and all of your helpful advice and, to my mom thank you, for all of your love and encouragement. Last but certainly not least

to my wife Carolyn, thank you so much, your love and patience over the last few years has made this possible. Without your help I could not have done this, thank you so much.

Statement of Originality

I hereby certify that all of the work described within this thesis is the original work of the author. Any published (or unpublished) ideas and/or techniques from the work of others are fully acknowledged in accordance with the standard referencing practices.

Chapter 2 describes the general equipment needed to build a conventional molecular beam velocity map imaging apparatus, and is not intended to imply that I designed these systems.

Chapter 3 describes the design and testing of the condensed phase velocity map imaging apparatus. This system I designed along with the help of my supervisor Dr. Hans-Peter Loock, another graduate student Mr. Jeff Crouse, and Dr. Jack Barnes.

Stephen W. C. Walker

August, 2016

Table of Contents

List of Figures

List of Tables

List of Abbreviations

Velocity Map Imaging	VMI
Interstellar Medium	ISM
Resonance Enhanced Multiphoton Ionization	REMPI
Kinetic Energy Release	KER
Laser Induced Fluorescence	LIF
Microchannel Plate	MCP
Time Resolved Photoelectron Imaging	TRPEI
Time Of Flight	TOF
Optical Parametric Oscillator	OPO
Titanium Sapphire	Ti-Sapph
Molecular Beam Valve	MBV
Complementary Metal–Oxide–Semiconductor	CMOS
Matrix Assisted Laser Desorption Ionization	MALDI
Random Access Memory	RAM
Potential Energy Surface	PES
Highest Occupied Molecular Orbital	HOMO
Singly Occupied Molecular Orbital	SOMO
Conical Intersection	CI
Condensed-Phase Velocity Map Imaging	CP-VMI
Phase Space Theory	PST
Rice–Ramsperger–Kassel–Marcus	RRKM

Chapter 1

Introduction

The central and fundamental aspect of chemistry has been described as "the fact that molecules react".[1] The most fundamental studies of how and why molecules react are the subject of reaction dynamics. The dynamics of species when reacting with light, in particular, is known as photodynamics, and is one of the two important fields of light-matter interactions. The second, optical spectroscopy, has been used to identify and characterize molecules and their electronic states since the beginning of the 20^{th} century. The interplay between spectroscopy and dynamics is considerable and together they yield information about the fundamental nature of the electronic structure, chemical bonds, and geometry of molecules as well as their interactions with each other and with radiation. Photodynamic studies can address very fundamental questions. For example, the formation of many organic and inorganic molecules in Earth's atmosphere or in space has photochemical causes.[2-4] Among these photochemical reactions, the most frequently (and easily) studied reactions are the photolysis of molecules in the gas phase and the subsequent reaction of the light-generated molecular fragments with other compounds. [5-9]

Photochemical reactions that occur inside transparent solid or liquid matrices are also well-known but cannot be studied with the same, quantum-state resolved degree of detail. Reactions within these media have been studied mainly using techniques such as infrared reflection absorption spectroscopy [10] which focuses on changes within the bulk, and

glancing angle Raman techniques to study effects at the interface between the atmosphere and the condensed surface.[11] Researchers have also investigated the photoproducts following irradiation of condensed phase species using several techniques. [12, 13, 14] For example, within the interstellar medium (ISM), ice matrices made from water or other compounds, play an important role in astrochemistry. Ice films serve as sinks for volatile molecules including CH_4, CO_2, NH_3, and NO_2 along with several others,[15] removing them from the gas phase. As the concentration of species on the surface and within the ice matrix increases, they may act as reaction sites leading to formation of species which would not normally be present within these systems. [4, 16] Additionally, light radiation from nearby stars can initiate reactions both with the ice matrix and with the species trapped within them. The dynamics of the reaction, the energies of the fragments, and the amount of energy transferred to the matrix material, along with the energy states of the fragments, all impact the chemical evolution in the universe. While the dynamics of photoinitiated reactions have been studied thoroughly in the gas phase,[17] studies of the respective photochemistry of trapped molecules in the condensed phase are limited in number and in detail. In order to build better astro(bio)chemical models we require more information on quantum-state-resolved reactions of photoinitiated reactions in the condensed state.

Similarly, in the polar regions of Earth, stratospheric clouds contain dust grains which are covered with a layer of water ice and can trap co-condensed molecular species in a similar manner as that found in the ISM.[18, 19] In order to address and improve current atmospheric chemistry models and climate models, these condensed phase reactions need to be included. Recent reports suggest that photoinitiated reactions of NO_2 are the source of the high concentrations of hydroxyl radical found in the Polar Regions.[20, 21] By

including only gas phase reaction dynamics in models for the polar atmosphere, critical information about the true origin of the species is lost. It is likely that future work on the quantum state-resolved photochemistry of water ice and the subsequent quenching reactions of the OH fragment may give further insights into the formation and reactivity of OH in the polar regions of Earth.

This thesis focuses on the interaction of light with NO_2 co-condensed in an inert argon matrix. The system was selected since NO_2 photochemistry is well-understood and the Ar-matrix does not react with light or with the photofragments. We therefore expect that the quantum state distributions can be readily understood as outcomes of the primary photodissociation process and subsequent matrix collision processes.

In order to address the spectroscopy and dynamics following the interaction in a meaningful way it is important to first review quantum mechanics of atomic and molecular structure. In this section the principles of atomic and polyatomic structure will be discussed. This is followed by a discussion of the underlying molecular dynamics as well as a short review of the experimental techniques used to understand them.

1.1 Electronic Structure of Atomic Systems

Following excitation of light with energy above the dissociation threshold, 398 nm, nitrogen dioxide dissociates by forming nitric oxide and atomic oxygen in a variety of quantum states.

$$\mathrm{NO_2} \xrightarrow{h\nu} \mathrm{NO}\left(v, J, \Omega, \Lambda, S\right) + \mathrm{O}\left(J, L, S\right) \tag{1.1}$$

The different atomic states are described by term symbols of the type

$$^{2S+1}L_J \tag{1.2}$$

where, *S*, *L* and *J* are the spin, orbital and overall angular momenta, respectively. In order to describe these term symbols properly, a brief description of quantum numbers may be necessary.

1.1.1 Hydrogenic Atoms

We view the electron as a particle wave which follows the Schrödinger equation.

$$\hat{H}\psi_i(\vec{r}) = E_i\psi_i(\vec{r}) \tag{1.3}$$

Where $\hat{H}$ is the Hamiltonian operator, $\psi_i(\vec{r})$ are the wavefunctions of the system in question, and E_i is the corresponding energy eigenvalue associated with $\psi_i(\vec{r})$ for the system and $\vec{r}$ stands for all coordinates.

The wave function can be used to determine the other electronic properties of the system. This can be seen in the solution to the Schrödinger equation for the hydrogen atom.

$$\psi_n(\vec{r}) = f\left(\frac{r}{a_o}\right)e^{\left(\frac{\nu}{na_o}\right)}Y_l^{m_l}(\theta,\phi) \tag{1.4}$$

Here *n* is the principal quantum number, *r* is the radial distance from the nucleus, a_o is the Bohr radius $a_o = \frac{h^2}{4\pi m_e e^2}$, the frequency, *ν,* is the energy divided by Planck's constant $\frac{\Delta E}{h}$, $f\left(\frac{r}{a_o}\right)$ is a power series of degree (*n*-1), and $Y_l^{m_l}(\theta,\phi)$ are the spherical harmonics.

The principle quantum number, *n*, designates the energy level. The state of a given electron is determined by *n* and three additional quantum numbers, *l*, m_l, and m_s. The combination

of the three quantum numbers, n, l, m_l, determine the electron's orbital, and m_s describes the spin state of the electron.

An electron in a given orbital will have two forms of angular momentum, i.e. spin and orbital angular momentum, which may be described as vectors with magnitudes

$$\begin{aligned} \left|\vec{l}\right| &= \hbar\sqrt{l(l+1)} \\ \left|\vec{s}\right| &= \hbar\sqrt{s(s+1)} \end{aligned} \tag{1.5}$$

The vector addition of $\vec{l}$ and $\vec{s}$ yield the total angular momentum $\vec{j}$, which has a magnitude of:

$$\left|\vec{j}\right| = \hbar\sqrt{j(j+1)} \tag{1.6}$$

The quantum number j can have integer and half-integer values of:

$$j = \left|l+s\right|, \left|l+s-1\right|, ..., \left|l-s\right| \tag{1.7}$$

1.1.2 Many-Electron Atoms

The above description is for systems of only one electron. In atoms with more than one electron, the orbital and angular momentum of the many electrons can be combined to give the total angular momentum J. There are two commonly used methods to couple the angular momenta known as Russell-Saunders (also known as LS coupling) and jj-coupling. In the LS coupling the individual orbital angular momenta of the electrons and the spin angular momenta are added separately to form total L and S, respectively, and are then added to yield J.

$$\begin{aligned} \vec{L} &= \vec{l}_a + \vec{l}_b + ... \\ \vec{S} &= \vec{s}_a + \vec{s}_b + ... \\ \vec{J} &= \vec{L} + \vec{S} \end{aligned} \tag{1.8}$$

This coupling scheme is used mostly with light atoms, which are of relevance in this thesis.

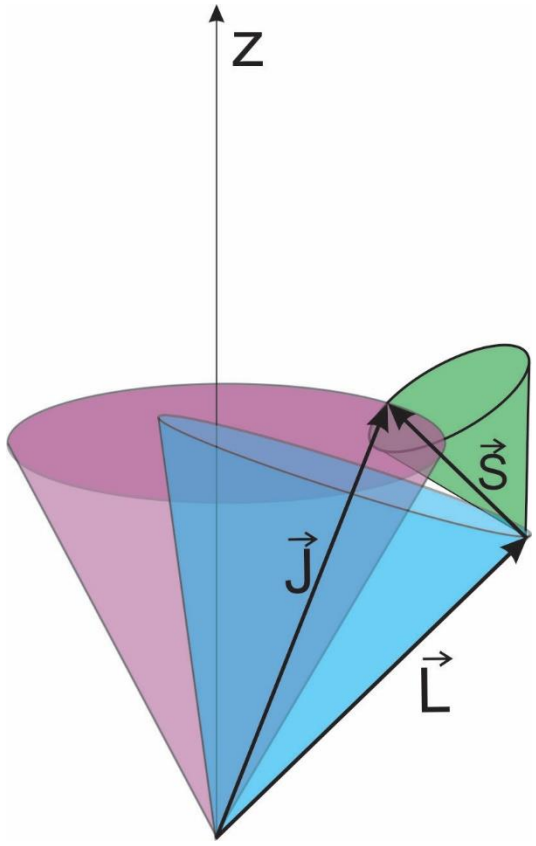

Figure 1.1:Russell-Saunders coupling scheme, individual spin and orbital angular momenta are summed separately, then combined to form J.

In the *jj*-coupling scheme the individual orbital and spin angular momenta are combined first to produce *j* quantum numbers for each of the electrons which are then combined to form the total angular momentum vector $\vec{J}$. This scheme is used for heavier elements or highly excited states of light atoms. The *LS* or *jj* coupling schemes can be taken as limiting cases, and for all atoms other than hydrogen and one-electron ions the, l, m_l, m_s and j quantum numbers are to a larger or lesser extent ill-defined.

1.1.2.1 Atomic Term Symbols for Oxygen

The oxygen atomic fragment can have a variety of different states depending on the fragmentation process. In determining the term symbol for the different states we start from Equation 1.1 and first determine the possible total orbital angular momentum *L*. For ground state oxygen, we have *L*=1 and *S*=1, and this yields three possible *J* values of 2, 1, and 0. The corresponding term symbols are $^3P_0$, $^3P_1$, $^3P_2$. The $^3P_1$ state and $^3P_0$ states lie 158.265 cm^{-1} and 226.977 cm^{-1} above the $^3P_2$ ground state. Higher lying excited states of oxygen may be formed when NO_2 is excited with light at wavelengths shorter than 243 nm, where it is possible to form atomic oxygen with *L*=2 and *S*=0, corresponding to the term symbol $^1D_2$ (15867.862 cm^{-1} above the $^3P_2$ ground state)[22] The higher atomic fragment states require that a large amount of energy is transferred from the photon to the electronic energy of the oxygen fragment. Consequently, less energy will be available as kinetic energy of the fragments and the matrix bulk. Identifying the energy partitioning into the different fragments in the condensed phase is an important aspect of this research, as different electronic states of the fragments may have drastically different chemistry.

1.2 Structure of Diatomic and Polyatomic Molecules

1.2.1 The Electronic Structure of Diatomic Molecules

Aside from atomic oxygen, the photodissociation of NO_2 also produces nitric oxide, NO. In order to identify the energy partitioning in this diatomic molecule, the rovibrational states of the NO fragment are state-selectively ionized. A description of the electronic,

vibrational, and rotational structure of diatomic molecules is needed to describe the experimental and chemical processes within this thesis.

1.2.1.1 Hund's Cases

In order to describe the electronic structure of diatomic molecules we use, again, term symbols. As was the case with atoms, the resultant orbital angular momentum of all the electrons in a molecule is the sum of the all the individual orbital angular momenta. However, unlike in an atom where the electrons' motions occur in a spherically symmetrical field, in diatomic molecules the symmetry is reduced to an axial symmetry about the internuclear axis. This results in a precession of $\vec{L}$ about the internuclear axis, thus the total orbital angular momentum $\vec{L}$ is not well defined and is therefore not a "good" quantum number. Electronic states of diatomic molecules, are instead labeled according to the projection of this vector onto the internuclear axis, which is a constant of motion, the resulting vector is known as $\vec{\Lambda}$.[23] This new quantum number is analogous to $\vec{L}$ in atomic systems and can take on values of 0,1,2,3... with the values labeled with Greek letters, σ, π, δ, ϕ instead. Similarly, the total electron spin, $\vec{S}$ is projected onto the axis forming the vector $\vec{\Sigma}$ (not to be confused with the $\vec{\Lambda}$ orbital, Σ). The sum of the two projected vectors form $\vec{\Omega}$, and the states are labeled with term symbols similar to those of atoms.

$$^{2S+1}\Lambda_{\Omega} \tag{1.9}$$

The two electronic states of NO which are of interest in this thesis are the ground state, and the first excited state which is accessed during the ionization process. The ground state consists of $S = 1/2$, and $\Lambda = 1$ which yields term symbols of $^2\Pi_{1/2}$ and $^2\Pi_{3/2}$, corresponding

to two states which differ only by their spin-orbit coupling. In order to identify the populations of the rovibrational states of these two electronic states, the molecules are excited to a much higher lying electronic state, from which ionization then follows after absorption of a second photon. This excited state has S = 1/2, and Λ = 0 which yields a term symbol of $^2\sum^+$. The plus sign indicates the parity property of the electronic wavefunction, indicating that the wavefunction does not change sign upon reflection. This is described in more detail in Section 1.2.4.

There are five ways of coupling the angular momenta in diatomic molecules that were proposed by Hund, which make up the so-called Hund's cases. The $^2\Pi$ ground state of nitric oxide is primarily known as a Hund's Case (a) state, however, it can also be treated as an intermediate between Case (a) and (b). The excited $^2\sum^+$, state falls under Hund's Case (b). Only these two cases will be discussed in detail in this thesis. In Case (a) the coupling between the electronic and rotational motion of the molecule is weak, this leaves $\vec{L}$ and $\vec{S}$ uncoupled to one another, instead they both couple to the internuclear axis.

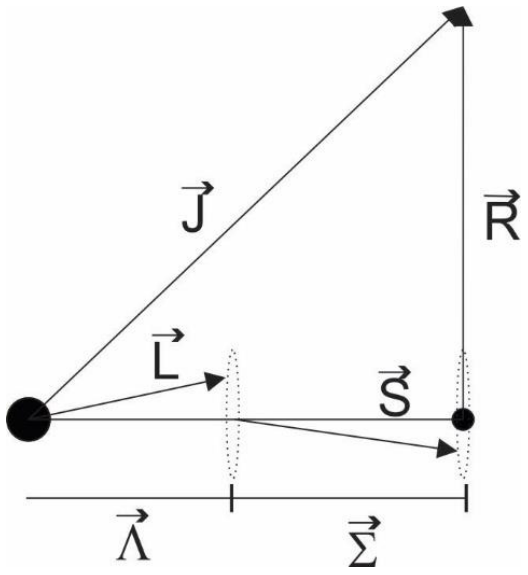

Figure 1.2: Hund's Case (A), the precession of $\vec{L}$ and $\vec{S}$ about the internuclear axis are indicated by the dashed ellipses. Both spin and orbital angular momentum are coupled to the internuclear axis. The coupling of these to the rotation of the molecule forms the total angular momentum $\vec{J}$. Using the notation of Bernath.[24]

The electric field along the internuclear axis couples first the orbital angular momentum to the bond axis. The "clockwise" and "counterclockwise" motion of the electron around the axis produces the projection vector $\pm\vec{\Lambda}$. The electron's motion additionally creates a magnetic field, which orients the spin angular momentum $\vec{S}$ to produce a projection vector $\vec{\Sigma}$ – analogous to $\vec{\Lambda}$. The sum of the two projection vectors is the vector $\vec{\Omega}$, which in turn couples to the rotation of the molecule $\vec{R}$ to give the total angular momentum vector, $\vec{J}$. This scheme is shown in Figure 1.2. The total angular momentum can be seen as a vector with the value, $\vec{J} = \vec{R} + \vec{L} + \vec{S}$. Hund's case (a) occurs in situations where the coupling between the total orbital angular momentum and total spin angular momentum is weak and both $\vec{L}$ and $\vec{S}$ are coupled to the bond axis. However, as the rotational angular momentum of the molecule increases the molecules switches from Hund's case (a) to (b). In Hund's

case (b) the spin angular momentum decouples from the bond axis. As the orbital angular momentum, $\vec{L}$, is still coupled to the axis the projection vector, $\vec{\Lambda}$, again couples to the rotation of the molecule, and this produces a new vector $\vec{N}$. It is this new vector with which $\vec{S}$ couples to give the total angular momentum $\vec{J}$. This is shown in Figure 1.3. For states where $\Lambda = 0$ are automatically described by Hund's Case (b), i.e. trivially the (non-existent) orbital angular momentum cannot couple to the spin momentum.

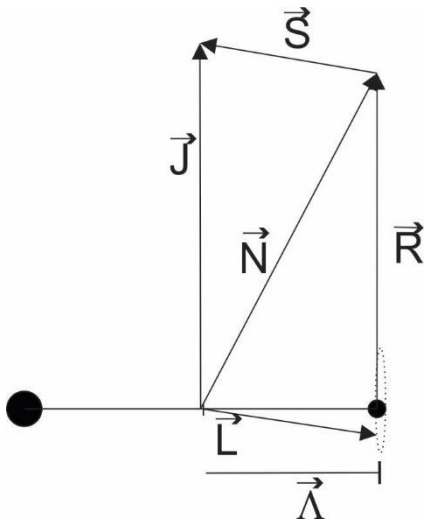

Figure 1.3: Hund's Case (B). Only the orbital angular momentum is coupled to the internuclear axis, which couples to the rotation of the molecule to form $\vec{N}$, the total angular momentum apart from spin. The spin angular momentum then couples to $\vec{N}$, to form $\vec{J}$.

1.2.2 The Vibrational Structure of Diatomics

In the Born-Oppenheimer limit, the electronic and nuclear wavefunctions can be separated, likewise the vibrational and rotational wavefunctions can be separated and the total energy becomes a sum of these individual contributions.

$$\begin{aligned} \psi &= \psi_{el} \cdot \psi_{vib} \cdot \psi_{rot} \\ E &= E_{el} + E_{vib} + E_{rot} \end{aligned} \tag{1.10}$$

The potential energy of the vibrating diatomic molecule can be written as a function of the nuclear separation, (r):

$$V(r) = E_{el}(r) + V_{NN}(r) \tag{1.11}$$

where, $E_{el}(r)$ is the electronic energy and is found by solving the electronic Schrödinger equation. However, there is no simple analytic form of $E_{el}(r)$. $V_{NN}(r)$ is the potential energy corresponding to the nuclear-nuclear repulsion. The shape of the overall potential $V(r)$ may be fit to experimental data using different equations, such as the Dunham and Morse potentials. For example, when the potential energy is described as a Dunham expansion, the vibrational energy of a diatomic molecule along the internuclear axis is given by:

$$E_{vib} = (v + 1/2)\omega_e - (v + 1/2)^2 \omega_e \chi_e + \ldots \tag{1.12}$$

Here the constants, $\omega_e = \beta\left(\frac{Dh \times 10^2}{2\pi^2 c\mu}\right)$ and $\omega_e\chi_e = \frac{h\beta^2 \times 10^2}{8\pi^2 c\mu}$ are the vibrational wavenumber for a classical oscillator, and the first anharmonic constant respectively. The fundamental constants and state-specific parameters are as follows: The Morse potential constant β (cm^{-1}), the dissociation energy D (cm^{-1}), Planck's constant h, the speed of light c, and the reduced mass μ. The Morse potential is able to account for dissociation. Additional rotational terms can be included if the molecule rotates. After including higher order terms, the vibrational energy expression can be written with the effect of rotational components on the vibrational energies as:

$$E_{vib} = (v + 1/2)\omega_e - (v + 1/2)^2 \omega_e \chi_e + B_e J(J+1) - D_e (J(J+1))^2 - \alpha(v + 1/2)J(J+1) \tag{1.13}$$

Where the new terms $B_e = \frac{h \times 10^2}{8\pi^2 c\mu r_e^{\,2}}$ and $\alpha = \frac{6(\omega_e \chi_e B_e^{\,3})^{1/2}}{\omega_e} - \frac{6B_e^2}{\omega_e}$ are the rigid rotor rotational constant (cm^{-1}) and the Perkeris relationship (cm^{-1}), which describes the coupling

between the vibrational and rotational motions, through their effect on the bond length. The equilibrium bond length is given as r_e, and $D_e = \frac{4B_e^3}{\omega_e^2}$ (cm^{-1}) is the centrifugal distortion correction for the zero point energy.

1.2.3 Rotational Motion of Diatomic Molecules

It can be shown through the use of the rotational Hamiltonian and the Schrödinger wave equation that the allowed rotational energies for a rigid diatomic molecule depend on both the moment of inertia of the rotation and the total angular momentum quantum number, giving an energy expression:

$$E_J = \frac{h^2}{8\pi^2 I} J(J+1) \tag{1.14}$$

For all molecules there are three principal axes in the molecular frame. For molecules with C_s symmetry the three rotation axes are associated with their own moment of inertia, labeled I_a, I_b and I_c, with I_a being the smallest and I_c being the largest moment of inertia. Linear molecules are a special case: for linear point groups, $I_a = 0$, as rotating about the bond has no moment of inertia. Additionally, the two end-over-end rotations are degenerate and $I_b = I_c$.[24]

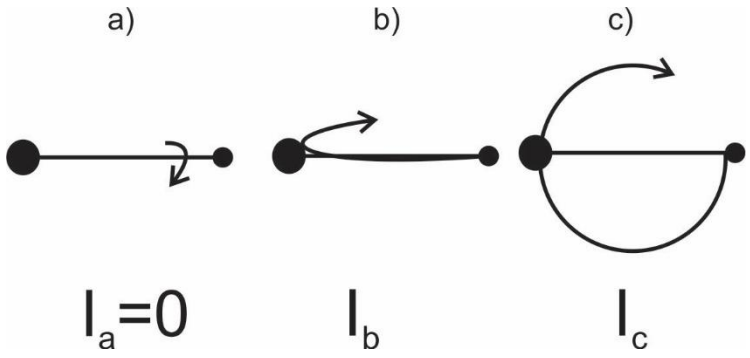

Figure 1.4:Moments of inertia for the three different rotations of a diatomic molecule

Because I_b and I_c are equal we use I_b by convention and Equation 1.14 becomes simply

$$E_J = \frac{h}{8\pi^2 I_b c} J(J+1) \tag{1.15}$$

where c is the speed of light and is expressed in [cm/s] - this change expresses the energy in wavenumbers with units of reciprocal centimeters, cm^{-1}. As mentioned in the previous section, the collection of constants on the right is usually given the symbol B, and is known as the rotational constant.

By measuring the population of the many rotational states of the NO fragment following dissociation, we are able to determine the amount of energy that is partitioned into the NO molecule's rotational motion. The chemistry of the NO fragment may vary depending on the rotational states activated through the dissociation process. While a purely rotational spectrum of a closed shell molecule shows only two branches corresponding to the $\Delta J = \pm 1$ selection rule, J'-J'' = +1 (R-branch) and J'-J'' = -1 (P-branch), open-shell molecules having a net spin show more complicated spectra. In addition, simultaneous excitation of vibrational motion and population of electronically excited states produce increasingly complex spectra. Additionally, there are several degeneracy lifting effects due to coupling

of electron spin momenta, orbital momenta and the molecules' rotation. These effects are discussed in the following sections.

1.2.4 Parity and Degeneracy Lifting Effects

Parity is a measure of the symmetry of the wavefunction with respect to inversion or reflection in the lab frame and it plays a large role in labeling the energy states of molecules. For example, the permutation-inversion operator ($\hat{E}^*$) inverts the atoms in a molecule, but leaves $|\psi|^2$ unchanged. Changes in the sign of the wavefunction is denoted with either a (-) or (+), where (-) signifies a change in sign and (+) means that the sign is not changed.[24] When applied to rotational wavefunctions, rotational states are therefore either labelled (+) or (-) to indicate their parity. The total parity of a linear molecule's wavefunction alternates with *J*, and one can factor out the sign of the rotational wavefunction by designating those rotational levels with a total parity of $+(-1)^J$ as having *e* parity and those with total parity of $-(-1)^J$ as having *f* parity. Half-integer values of *J* are treated similarly:

$$\text{States with total parity} + (-1)^{J-\frac{1}{2}} \text{ are labeled e parity}$$
$$\text{States with total parity} - (-1)^{J-\frac{1}{2}} \text{ are labeled f parity}$$

This e/f parity labeling system is then *J* independent, but still gives an indication of the parity of any given rotational level. The effect of parity on the electric dipole moment $\vec{\mu}$ which transforms as -1 under (+/-) parity, results in a parity selection rule, since the parity of the transition moment, shown below, must be equal to +1 for an allowed transition.

$$\int \psi_i^* \vec{\mu} \psi_i d\tau \tag{1.16}$$

This means that for even changes in J, such as the Q branch transitions where $\Delta J = 0$, the parity of the rotational states must change from e ↔ f or f ↔ e during the transition; correspondingly, for odd changes of J, the P and R branches ($\Delta J = \pm 1$) must retain their parity, e ↔ e or f ↔ f. In a closed-shell molecule, the two rotational levels of opposite parity are degenerate. However, for open-shell molecules there are two interactions, spin-rotation interactions and Λ doubling, which lift this degeneracy. Both of these effects are present in the rovibrational spectrum of NO, and are discussed in detail below.

1.2.5 Spin-Rotation Interactions

As mentioned in 1.1.2.1 in a Hund's Case (b) molecule the spin angular momentum decouples from the internuclear axis. This occurs when the orbital angular momentum does not have a well-defined precession about the internuclear axis, or is not present at all (i.e. for a Σ -state $\Lambda = 0$). In these cases the remaining angular momenta form the vector $\vec{N}$ and the total angular momentum $\vec{J}$ is the sum of $\vec{N} + \vec{S}$. The possible values of J for a given N are then given by:

$$J = (N+S), (N+S-1) \ldots |N-S| \tag{1.17}$$

For each value of N there are $(2S+1)$, spin components, and although the parity levels are no longer degenerate, the spin components are. This (2S+1) term has a large amount of significance in spectroscopy and the term spin multiplicity is used to denote it. As mentioned above in Section 1.2.1.1 the upper state of NO used in the ionization process is a $^2\Sigma$ state and is a simple state to use to illustrate this effect.

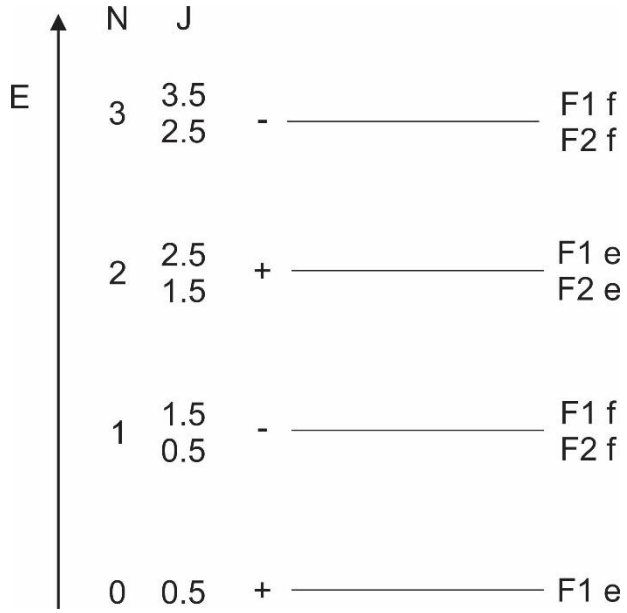

Figure 1.5:The rotational energy levels of a $^2\sum$ state, with e and f parity splitting, the F1 and F2 designations denote the spin-rotation splitting, 0 in this case.

While in Figure 1.5 the spin components are degenerate, if the angular momentum of the electron spin can couple to the magnetic field of the rotation of the molecule, there will be a splitting between the two *J* values for each value of *N* as $\vec{S}$ can couple with $\vec{N}$ in different ways. This is known as a spin-rotation interaction, and for a doublet state it is commonly known as spin doubling or doublet splitting.[24]

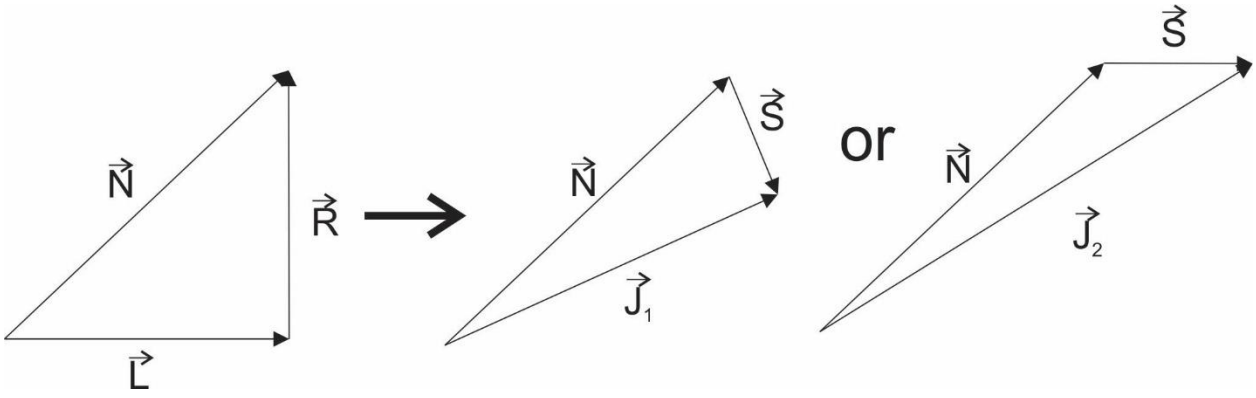

Figure 1.6: Vector diagrams of doublet splitting for $\vec{N}$ and $\vec{S}$.

The spin-rotation interaction, which is usually given the symbol γ removes the degeneracy in the two *F* states for each *N*, as $\vec{S}$ can go with, or against $\vec{N}$. The rotational energy levels for a doublet state are described by:

$$F_1(N) = BN(N+1) - D(N(N+1))^2 + \frac{\gamma N}{2}$$
$$F_2(N) = BN(N+1) - D(N(N+1))^2 - \frac{\gamma N}{2} \qquad (1.18)$$

This difference leads to a new set of features that would be seen in an experimental spectrum and can be shown in an energy level diagram.[24]

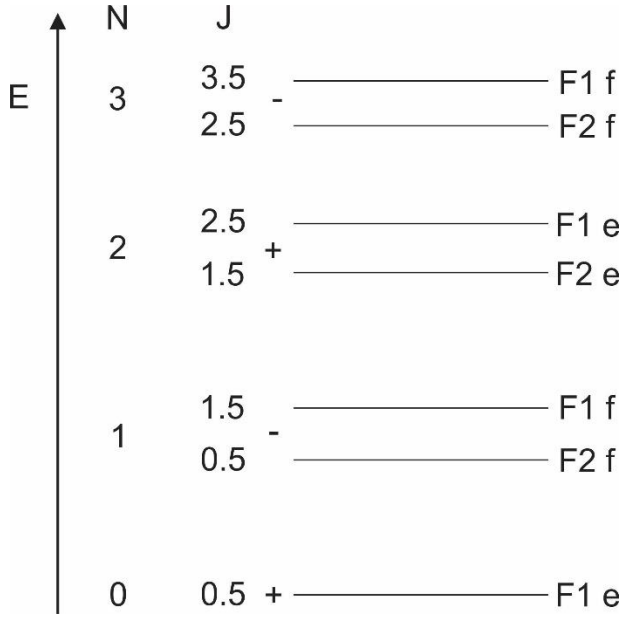

Figure 1.7:Doublet splitting interaction of $\vec{N}$ with $\vec{S}$

In states where $\Lambda \neq 0$, $\vec{S}$ can couple to Λ in a similar way that it coupled to *N* in the case above. This interaction can then yield two states which are either shifted up or down, Ω = Λ + S and Ω = Λ - S. The resulting split levels have the same *N* quantum number but

different J values. This electron angular momentum coupling is independent of rotation and is known as spin-orbit doubling as the coupling is between the electron spin and the orbital angular momentum. The splitting can be seen in the energy level diagram of a doublet Π state such as the ground state of NO and is shown in Figure 1.8 which also includes another form of splitting known as Λ-doubling.

1.2.6 Λ-doubling

The coupling of the total electron orbital angular momentum (Λ) with rotation of the molecule $\vec{R}$ creates two possible values of $\pm\Lambda$ when $\Lambda \neq 0$. Thereby producing two values of e and f parity for each value of J. In the absence of rotation these are degenerate and have a splitting in the presence of rotation which increases with J. It is present in all states with $\Lambda \neq 0$ and is known as Λ-doubling. Λ doubling is most commonly found in Π states, so it is of particular interest for the lower two states of NO. The splitting, known as lambda-type splitting can be approximated by:

$$\Delta\nu_{cd}(J) = F_c(J) - F_d(J) = qJ(J+1) \tag{1.19}$$

Where F_c and F_d are the energy levels of two states which formed due to the Λ-doubling, and q is the splitting factor given by:

$$q = B_{v_c} - B_{v_d} \tag{1.20}$$

The figure below shows the energy levels of doublet Π state. It is used to illustrate both the lambda doubling and the spin-orbit splitting.

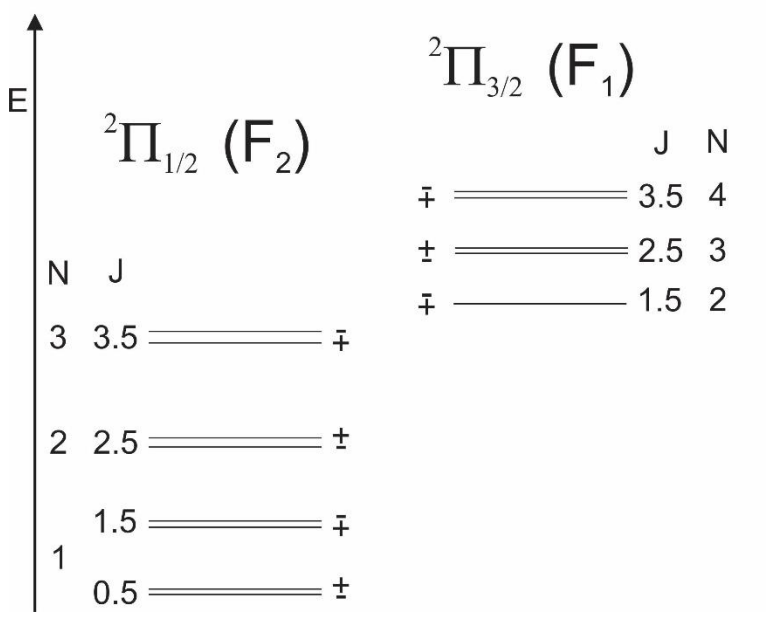

Figure 1.8: Energy level diagram for a $^2\Pi$ system. The energy difference between the states with different Ω values (3/2 and ½) represents the spin-orbit splitting, while the smaller splitting separating the different +/- states with equivalent J is due to the Λ doubling. Note that the energies are not to scale and the spin-orbit splitting is usually much larger than shown.

All these different energy levels may be populated by the NO fragment following dissociation depending on how the energy is partitioned to the fragment. By using techniques such as Resonance-Enhanced-MultiPhoton-Ionization (REMPI) (Section 2.5) we are able to probe the relative population of each of these energy levels.

1.3 Spectroscopic Structure of Polyatomics

1.3.1 Electronic States of Polyatomics

The electronic states of polyatomic molecules can be classified similarly to those of diatomic molecules, but due to the extra nuclei the potential energy surfaces become increasingly complex. A simple convention is used when dealing with well-known electronic states of molecules. Here the ground state is labeled *X* and, the second lowest

electronic state having the same multiplicity, $2S+1$, is labelled by *A*. For higher electronic states of this multiplicity the labels continue alphabetically. A second ladder of *a*, *b*, *c*, etc. states is created for states that have a different multiplicity than the ground (*X*-)state. While this system is convenient when identifying different electronic states, it does not give any information about the particular state of interest. The states are therefore also labelled using symmetry labels that describe the transformation of the total electronic wavefunction in the point group of the molecular frame. The method uses the point group of the molecule when it is in its equilibrium geometry - for instance C_{2v} for water or for nitrogen dioxide. The point group is associated with a character table such as the one shown below, and the electronic eigenfunctions of each electronic state are described by one of the irreducible representations.

Table 1.1: Character table for C_{2v} point group

Irreducible Representation (Symmetry Type)	Symmetry Operator			
	E	C_2	$\sigma_v(xz)$	$\sigma'_v(yz)$
A_1	1	1	1	1
A_2	1	1	-1	-1
B_1	1	-1	1	-1
B_2	1	-1	-1	1

The terms show the effect on the wavefunction following the effect of the symmetry operator, with 1 indicating no change and -1 representing a change in sign of the wavefunction. The electronic states of NO_2 can be used as an example. Here, the ground electronic state of NO_2 is an A_1 state, and the electronic eigenfunction remains unchanged for all four symmetry operations as all terms are equal to 1. The next lowest electronic state

is a B_1 state. In this case there is a sign change in the eigenfunctions when the operators C_2 and $\sigma'_v(yz)$ are applied.

Additionally the multiplicity of the state, $2S+1$, is used to describe any given state, just as it was for diatomic molecules, thus a C_{2v} molecule with $S = 0$ would give rise to $^1A_1$, $^1A_2$, $^1B_1$, or $^1B_2$, states and if $S=1/2$ we obtain $^2A_1$, $^2A_2$, $^2B_1$, $^2B_2$. For example as NO_2 has one unpaired electron, the two states described above can be specified further as states $X\ ^2A_1$ -state and $A\ ^2B_1$ -state respectively.

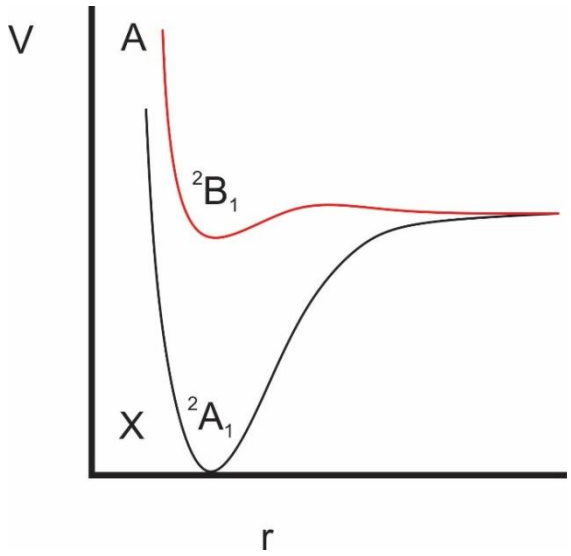

Figure 1.9:Sketch of the first two electronic states of NO_2 labeled using the generic labeling scheme (left of each potential) and using C_{2v} symmetry labels (above each potential).

1.3.2 Excitation of Electronic States

The interaction of light with matter plays two important roles within this thesis; the first is the excitation of a polyatomic molecule to a dissociative state, and the consequent condensed phase dynamics – the main goal of this thesis. The second aspect is the selective ionization of the fragments following the dissociation process, i.e. the process allowing us to state-selectively detect the molecular NO fragments.

The interaction of light with matter can be seen as a perturbation of the system Hamiltonian symbolized as $\hat{H}'$;

$$\begin{aligned} \hat{H} &= \hat{H}^{o} + \hat{H}^{'} \\ H^{'} &= -\vec{\mu}_{e}(n,\alpha)\cdot\vec{E}(r,t) \end{aligned} \tag{1.21}$$

Where, $\vec{E}(r,t)$ is the electric field and $\vec{\mu}_e$ is the electric dipole moment operator and is composed of *n* electrons and α nuclei.[24]

The absorption cross section, σ(ω) is proportional to the square of the transition dipole moment, $\vec{\mu}$, and $\vec{E}$, the electric field component of the (linearly polarized) light.

$$\sigma_{a}(\omega) \propto (\vec{E}\cdot\vec{\mu})^{2} \tag{1.22}$$

As the cross section is proportional to the dot product of these two vectors when the photochemical process is induced by polarized light, the probability that a molecule absorbs the light depends on the orientation of the transition dipole moment with respect to the E-vector. While this plays a large role in excitation of species, it has an even larger impact with respect to the dynamics of the species which dissociate following photon absorption and will be discussed in more detail in Section 1.4.

1.3.3 Franck-Condon Principle

The classical Franck-Condon principle can be seen as an experimental consequence of the Born-Oppenheimer approximation. If we treat the electronic rearrangement following the absorption of a photon to be fast compared to that of the nuclei, then the nuclei retain their positions and momenta throughout the absorption process and have the same coordinates on the excited surface as they had on the ground state potential energy surface. Consequently, the likelihood of a transition is governed by how similar the nuclear positions are in the upper and lower states.

The quantum mechanical treatment of the Franck-Condon principle is that the probability of a transition from one potential surface to another is highest, given all other aspects are equal, when the square of the transition overlap integral of the two wavefunctions is highest.

$$\left|\langle \psi_{el',v'}(\vec{R}) \middle| \vec{\mu}(\vec{R}) \middle| \psi_{el'',v''}(\vec{R}) \rangle\right|^2 \tag{1.23}$$

Here $\vec{\mu}(\vec{R})$ is the dipole moment. In most cases a second approximation may be made and the transition dipole moment is expanded, i.e. as independent of the nuclear coordinates, and the dipole moment is then factored out. The probability of the transition is then related directly to the square overlap integral.

$$\left|\langle \psi_{v'}(\vec{R}) \middle| \psi_{v''}(\vec{R}) \rangle\right|^2 \tag{1.24}$$

The resulting values of this integral are known as Frank-Condon factors.

The position and shape of the two potential curves of the states involved greatly impact the transition. If the two curves are very similar, and the nuclei are in a given vibrational state *v*, then the vibrational selection rule $\Delta v = 0$, is held rather strictly. In this case the overlap

integral is largest between a given vibrational state on the lower electronic state and a vibrational state with the same quantum number in the higher electronic state; this can be seen in the figure below. If on the other hand, the two electronic potential curves are very different, the vibrational states may have quite different quantum numbers, v', and the excitation probability is governed by the vibrational overlap.[25]

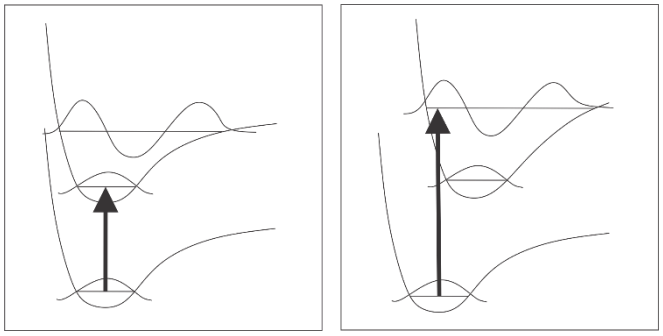

Figure 1.10:Franck-Condon Principle, the population of the upper electronic state following excitation from the ground is governed by the overlap of the two vibrational states.

1.3.4 Decay Pathways

Decay pathways for excited states of molecules, play an ever-present role within this thesis. The study of the dynamics of the dissociating excited NO_2 molecules within condensed phase media is the aim of the thesis. The ionization technique, used to detect the fragments relies on excitation to a bound electronic state prior to ionization. Even the laser which is used to ionize the fragments relies on the fluorescence of organic molecules used as the gain medium.

There are several decay pathways in which molecules shed excess energy - either through radiative transitions, such as fluorescence and phosphorescence, or through non-radiative decay processes, such as collisional deactivation, dissociation and others. Figure 1.11

displays many of these processes. In this thesis, predissociation of NO_2 (Process 3 in Figure 1.11) and fluorescence of the organic dye used in the ionization laser (Process 7) are of importance. The other potential decay pathways may be important to other molecules which could be probed by the same apparatus and are thus described as well.

Unfortunately, the dynamics of these decay processes are frequently not governed by a single excited state potential, and it is likely that the molecules will traverse two or more excited state potentials during the photofragmentation process. The corresponding electronic states are usually described as either being diabatic or adiabatic. In the adiabatic description, the electrons are allowed to adjust to every configuration of the nuclei, akin to the Born-Oppenheimer approximation of a complete decoupling of electronic and nuclear motion. In this description the adiabatic curves never cross and "avoided crossings" occur at the point where the diabatic curves would cross. The diabatic description states that the electrons do not adjust while the nuclei move. This is more appropriate for fast moving nuclei (e.g. protons) while processes with slowly moving (heavy) nuclei are better described adiabatically. Both descriptions are used within the literature when dealing with NO_2.

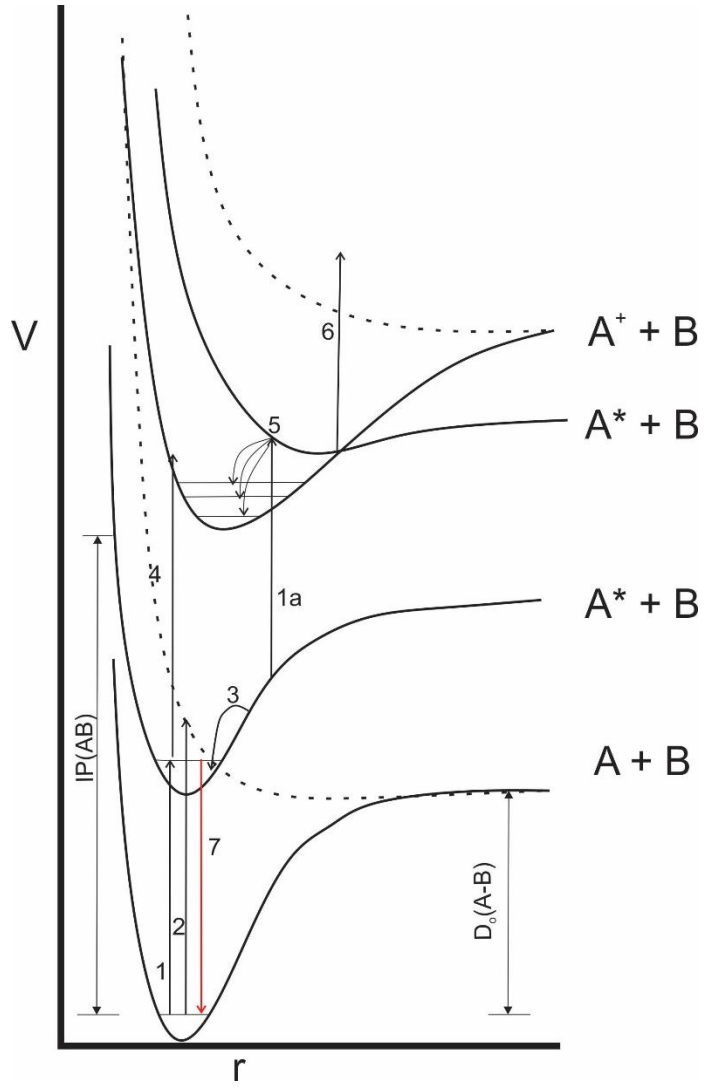

Figure 1.11:Decay pathways of excited electronic states. Descriptions of the events are explained in detail in the text. In the text the transitions are placed within parenthesis to distinguish them (vide infra).

1.3.4.1 Direct Dissociation

If the wavelength of the incoming photon has the equivalent energy corresponding to excitation to a bound state (Process 1 in Figure 1.11), an excited state of the molecule is formed. For excitation to occur, the wavelength must exactly match the energy difference between the rovibrational levels of the lower and upper states. If instead the wavelength is such that the excited state is unbound (2), the excitation results in dissociation. This is

known as a direct dissociation. In the latter case the excitation is possible over a large range of frequencies of light. The absorption cross section is therefore broad, and excess energy will be converted to kinetic energy of the fragments. The absorption spectrum can be approximated by the reflection principle, where the wavefunction of the lower state is projected onto the upper state.

1.3.4.2 Predissociation

It is also possible that a molecule in a bound excited state can cross onto a dissociative potential if the potentials cross at a lower level than the rovibrational state of the excited molecule. This process (3) in Figure 1.11 is known as indirect or predissociation. Predissociation can be described in three different ways based on the three forms of energy within the molecule (electronic, vibrational, or rotational) as proposed by Herzberg.[23, 26]

1.3.4.2.1 Herzberg Case I: Electronic Predissociation

Electronic predissociation – named Herzberg type I predissociation - is the most important form of predissociation for diatomic molecules. The other types are vibrational predissociation (type II) which does not occur for diatomics, and rotational predissociation (type III) which occurs much more seldomly.[23] As discussed in the Section 1.3.4.2 electronic predissociation occurs when the ro-vibrational levels of two near-degenerate electronic states overlap, and one of the electronic states is purely dissociative, forming a dissociation continuum.

The selection rules for predissociation can be summarized by the Kronig selection rules.[27]

$$\Delta J = 0,\ + \nleftrightarrow -,\ \mathrm{s} \nleftrightarrow a \tag{1.25}$$

The third condition insures that the symmetry of the two states is the same. For the molecules that are of interest in this thesis which are all Hund's case (a) or (b), we have the additional conditions:

$$\Delta S = 0 \text{ and } \Delta\Lambda = 0, \pm 1. \tag{1.26}$$

Finally, if the perturbation between the dissociative and bound states involved are both Hund's case (a) or are both involves Hund's (b), the following rules also apply respectively:[26]

$$\Delta\Sigma = 0 \text{ or } \Delta N = 0. \tag{1.27}$$

This form of predissociation is present in the gas phase dissociation of the first $^2B_2$ electronic state of NO_2. At a bond angle of approximately 108°, the first $^2B_2$ and the ground, $^2A_1$, states cross, thereby generating an intersection where electronic predissociation occurs. This is described more fully in the NO_2 literature review given in Chapter 4.

The probability of the transition from one state to another can be approximated by the Landau-Zener curve hopping probability.[28]

$$P_{LZ} = \exp\left(-\frac{4\pi V_{12}^2}{h\nu\left|s_1 - s_2\right|}\right) \tag{1.28}$$

Where,V_{12}^2 is half of the energy difference between the two states V_1 and V_2 at the point of closest contact, see Figure 1.12 below. Additionally, s_1 and s_2 are the slopes of the two unperturbed states, and v is the velocity of the motion, dr/dt.

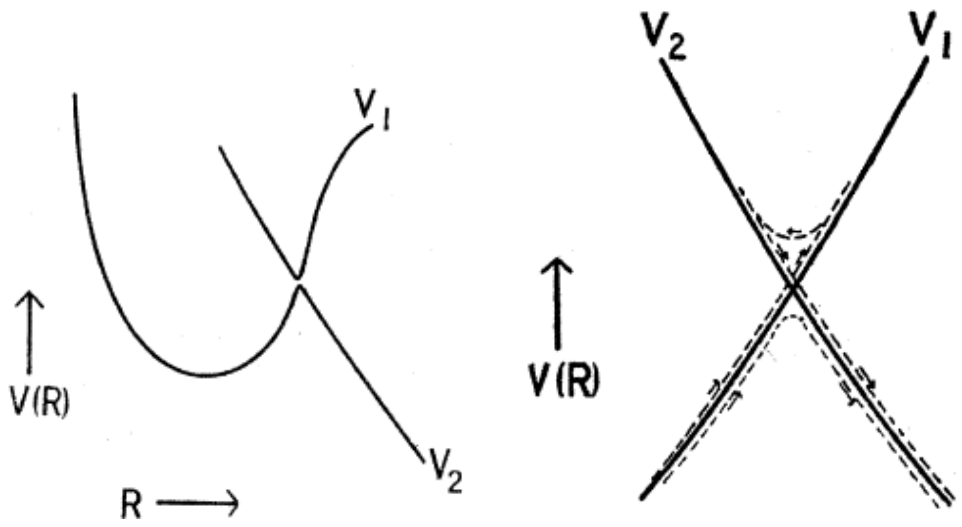

Figure 1.12: Left, a bound potential V_1 crossing a dissociative state V_2, notice that the curves are adiabatic and do not intersect. Right, the crossing region, the dashed lines indicate the two potential dissociation pathways. Images taken from Zener.[29]

1.3.4.2.2 Herzberg Case II: Vibrational Predissociation

In the second case, predissociation occurs via an overlap of the higher vibrational levels of an electronic state by a dissociation continuum joining onto a lower dissociation limit of the same electronic state. As mentioned above, this can only occur for molecules which contain 3 or more atoms. Since only the vibrational motion is changed, Case II can sometimes be distinguished from Cases I and III, as there should be no strong dependence on *J* or *N*.[26]

1.3.4.2.3 Herzberg Case III: Rotational Predissociation

Case III predissociation occurs when the high rotational levels of a given vibrational level approach the dissociation limit of the same electronic state. As the molecule adds energy to the electronic potential through centrifugal distortion, molecules with energies above the

dissociation potential will tunnel through the rotational barrier and dissociate on the same potential energy curve.

1.3.4.3 Direct Ionization and Dissociative Ionization

By exciting the molecule to a bound state within the ionization continuum (labelled (4) in Figure 1.11) molecular ions can be formed in a variety of rovibrational states. The ionization probability is governed by the same Franck-Condon factors as described in (1.24) above.

It is also possible to dissociate the molecule upon ionization, resulting in one ionized and one neutral fragment (see (6) in Figure 1.11).

1.3.4.4 Preionization (Auto-ionization)

A third form of ionization is possible in which the upper state is prepared in a so-called superexcited state. These are states of the neutral molecule that lie above the ionization threshold.[30] For example, Rydberg states that contain an excited ion core fall into this category. Superexcited states decay by a variety of processes including pre-ionization, i.e. by coupling of the neutral superexcited state to a state of the molecular ion. The same selection rules apply as in predissociation – keeping in mind that the outgoing electron has to be included in the state of the molecular ion. Preionization may therefore also be mediated by electronic, rotational or vibrational interactions. Lefebvre-Brion and Field [31, 32] also point out that it is possible for preionzation to be caused by spin-orbit interactions.

The role of preionization and dissociation of superexcited states of hydrogen halides have been studied by our group [6, 33, 34] and others [35, 36].

1.3.4.5 Radiative Transitions

Many excited electronic states remain stable for several nanoseconds or longer, if they are bound and not perturbed by nearby dissociative states. In this case, the lifetime of the excited molecule may be long enough for the molecules to release the excitation energy through the emission of radiation. If the transition is spin allowed then fluorescence takes place, typically from the lowest vibrational state of the excited state to the Franck-Condon allowed vibrational states of the electronic ground state. Phosphorescence, on the other hand describes the emission of light through a spin-forbidden process such as a triplet-singlet transition. The phosphorescence decay time can be longer than fluorescence decay by orders of magnitude. A more comprehensive discussion on fluorescence is found in Section 2.2.6.1.1 which discusses the fluorescence of organic dye molecules used to run common dye lasers.

1.4 Photodissociation Dynamics

The dynamics of photo-induced dissociation is governed by the excited state potential curve(s), which control to some extent the distribution of the excess energy into the electronic, vibrational and rotational states of the photofragments. This can be shown in a simple energy level diagram below.

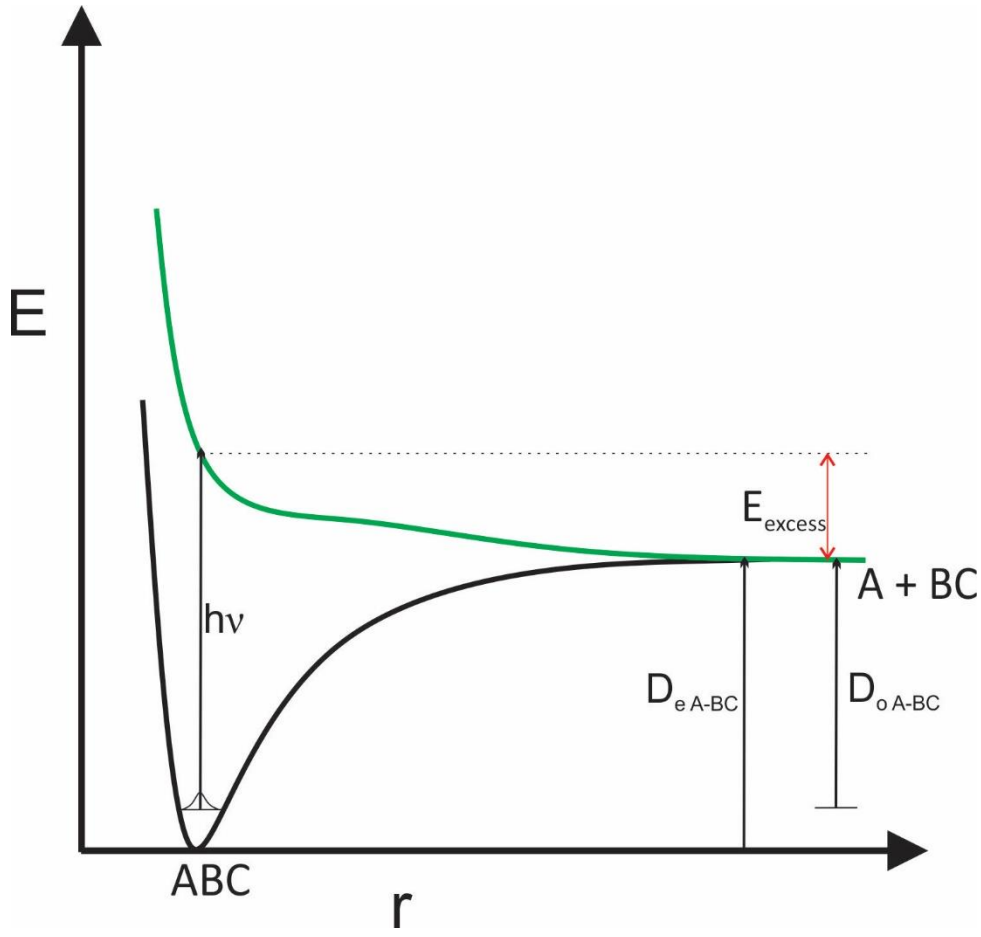

Figure 1.13:Kinetic energy release following dissociation of ABC.

The excess energy, E_{excess}, is the difference between the excitation energy, $h\nu$, and the dissociation energy, D_0. The excess energy is partitioned into the internal and the kinetic energies of the fragments. Energy conservation demands that the initial rovibronic energy of the parent molecule, $E_{int,ABC}$, is also included.

$$\begin{aligned} &a)\ \ h\nu + E_{\mathrm{int,ABC}} = D_{o,A-BC} + E_{excess} \\ &b)\ \ E_{excess} = E_{\mathrm{int},A} + E_{\mathrm{int},BC} + E_{k,A} + E_{k,\mathrm{BC}} \\ &c)\ \ KER = E_{k,A} + E_{k,\mathrm{BC}} \end{aligned} \tag{1.29}$$

As is apparent from these equations the total kinetic energy release, *KER*, i.e. the sum of the kinetic energy of both fragments, is equal to the energy difference between the sum of

the parent internal energy and excitation energy $h\nu$, and the sum of the dissociation energy and the internal energy (rovibronic energy) of the photofragments.

Equation (1.29)c expresses the kinetic energy of the fragments in the commonly used term Kinetic Energy Release (*KER*), i.e. the total excess kinetic energy following dissociation. In gas-phase (collision-free) experiments if one measures the velocity of only one of the fragments, it is possible to determine the internal energy of the co-fragment from conservation of linear momentum.

$$E_{k,\mathrm{A}} = \frac{m_{BC}}{m_A + m_{BC}} KER$$
$$E_{k,\mathrm{BC}} = \frac{m_A}{m_A + m_{BC}} KER \qquad (1.30)$$

Knowing the kinetic energy of one of the photofragments thereby permits calculating the kinetic energy of the other fragment and the KER. Energy conservation then dictates that the internal energy of the not-detected fragment, $E_{int,A}$, must be the difference between the excitation energy, $h\nu$, and the sum of KER, dissociation energy, D_0, and the internal energy of the detected fragment, $E_{int,BC}$.

1.4.1 Condensed Phase Considerations

All of the preceding information has been focused on gas phase reactions. For example Equations (1.29) and (1.30) assume that there is no energy exchange with the environment. When translating gas phase dynamics into condensed matter, it is useful to choose a matrix that interacts minimally with the electronic structure of the molecules. In this work, solid argon is used as the matrix. Argon does not react with NO, O and NO_2, and does not absorb

laser light at the relevant wavelengths. Thus the differences that are seen between this work and gas phase studies are largely due to the energy deposited into the matrix following dissociation, reducing the internal and kinetic energy of the fragmenting molecules.

1.4.2 Angular Distribution in Photodissociation

The angular distribution of the fragments can yield information on the species symmetry if the light source used in the dissociation is plane polarized. If we consider a set of dissociating diatomic molecules AB, then the fragments of each dissociation event will fly with equal momentum in opposite directions. When a large number of photodissociation events leading to the same final quantum state are collected, this whole set will build up a spherical distribution of fragments. This sphere is known as a Newton sphere. Each fragment species A and B will have a separate Newton sphere. The size of the Newton sphere is given by the speed of each fragment (i.e. its kinetic energy), and its angular distribution is governed by the alignment of the transition dipole with the electric field vector of the linearly polarized light source.

For all molecules and all transitions the transition dipole moment $\vec{\mu}$, has to be aligned parallel to the polarization of the electric vector of the dissociating light $\vec{E}$, to initiate an electronic transition with a probability of $(\vec{\mu}\cdot\vec{E})^2$.[37] The transition dipole moment in turn is correlated to the recoil velocity vector $\vec{v}$, due to the symmetry properties of the molecular orbitals involved in the transition. For example, the transition dipole moment of a diatomic molecule is oriented along the internuclear axis when both electronic states involved have the same symmetry, $\Delta\Omega = 0$ this is then called a "parallel transition".

The transition dipole moment is perpendicular to the axis when the states are of different symmetry ie. $\Delta\Omega = \pm 1$. It is then possible to correlate the electric field vector of the dissociating light with the recoil vector.

Zare noted that the normalized angular distribution can be described by the equation [38]

$$I(\theta) = \frac{1}{4\pi}\left[1 + \beta P_2(\cos\theta)\right] \tag{1.31}$$

Where θ, is the angle between vectors $\vec{v}$ and $\vec{E}$, P_2 is the second Legendre polynomial $P_2(x) = \frac{1}{2}\left(3x^2 - 1\right)$ and β is the anisotropy parameter, which can take on values of $-1 \leq \beta \leq 2$.

An angular anisotropy parameter of -1 is indicative of a perpendicular transition, $\Delta\Omega = \pm 1$, and a value of 2 indicates a parallel transition $\Delta\Omega = 0$. As long as the molecule does not rotate during the dissociation process, β assumes its limiting values.

In the case of a triatomic molecule it is also possible to correlate the diatomic fragment angular momentum $\vec{J}$ with $\vec{E}$, $\vec{\mu}$, and $\vec{v}$. If the molecule is moving through a bending motion as it dissociates, a torque perpendicular to the dissociating bond is produced. The alignment of the angular momentum vector with the electric field component can be probed by measuring the rotational state intensities as a function of probe laser polarization.[37]

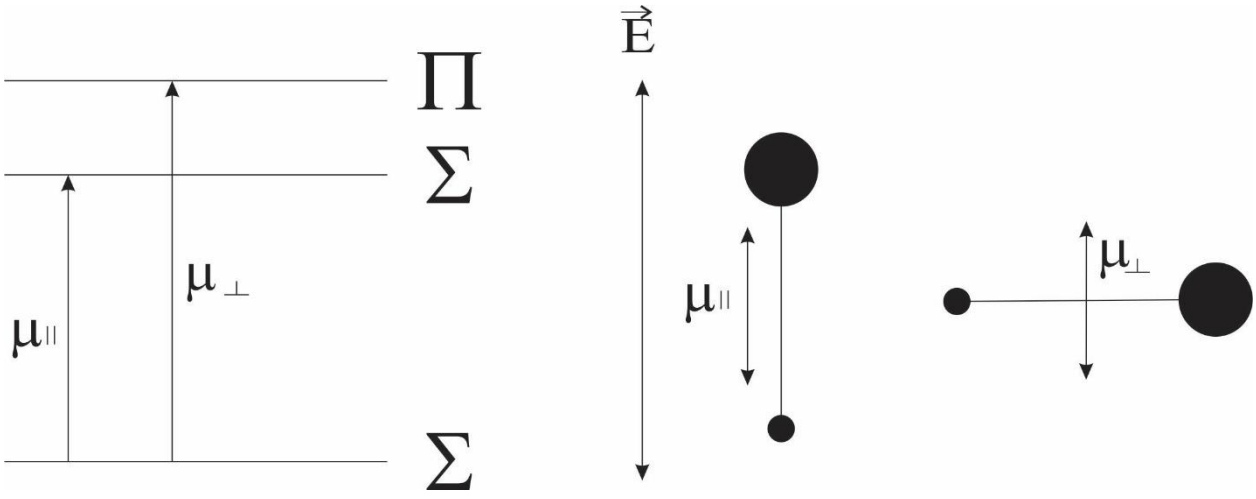

Figure 1.14:The ($\vec{\mu} - \vec{v}$) correlation for a diatomic molecule dissociation. $\mu_{\parallel}$ and $\mu_{\perp}$ indicate that the transition dipole moment is parallel or perpendicular to the electric field respectively. Adapted from Romanescu.[39]

1.5 Early Imaging Experiments

Once Zare's expression for the angular distribution was published, it became evident that by measuring the Newton sphere of the fragments one could gain information about the dissociation dynamics of the process. It took several years before Zare's equation was used experimentally. Solomon was the first to observe the distribution of the fragment recoil velocity.[40] The experiment involved using a small hemispheric dome whose inside surface was coated in tellurium. Within the dome, linearly polarized light was used to photolyse bromine, the etching rate of the film due to the fragments was observed to depend on the angle between the recoil velocity $\vec{v}$ and the electric field vector $\vec{E}$. The etching was found to peak perpendicular to $\vec{E}$, which indicates that the transition was a perpendicular transition.

While this method gave information on the anisotropy, no information about the magnitude of the individual recoil vectors could be resolved. However, only a few years later in 1969, separately Busch [41] and Diesen [42] published similar techniques to obtain both the direction and magnitude of $\vec{v}$. In these experiments a laser, linearly polarized, was used to dissociate halogen molecules, halogen-containing molecules, as well as NO_2, although the authors note that the results for NO_2 were incomplete. A quadrupole mass spectrometer was employed to detect the arrival time and angular distribution of the fragments.

1.5.1 Doppler Spectroscopy and Photofragment Time-Of-Flight Profiling

An interesting alternative approach to obtaining the angular anisotropy parameter based on the Doppler effect was proposed by Zare and Herschbach.[43] In Doppler spectroscopy the velocity of the fragments are determined through the shift in the absorption as the molecule travels towards the laser during the ionization process. If a fragment is moving at an angle θ_v with respect to the electric field of the dissociation laser, the velocity of the fragment along the direction of the light is $v\cos(\theta_v)$, and the absorption frequency is shifted from its rest absorption frequency, ν_0, to $\nu = \nu_o\,(1+(v/c)\cos(\theta_v))$. The angular distribution can be written as: [1, 37, 44]

$$P(\theta_v) = \frac{1+\beta P_2(\cos\theta)\dfrac{3((\nu-\nu_o)/\nu_o)^2(c/v)^2-1}{2}}{4\pi} \qquad (1.32)$$

where $P_2(x)$ is the second Legendre polynomial. The absorption frequency of the fragment is dependent on the internal state, and a Doppler profile can be determined for each internal state of the fragment. In practice, it has become more common to use Laser Induced Fluorescence (LIF) and monitor the shift in the emission. Schmiedl was the first to confirm

the effect in experiments that monitored the Doppler profile of the H atom produced in the dissociation of HI using LIF [45]. Dixon [46] expanded on this work and gave general equations to determine several vector correlations using LIF-Doppler spectroscopy. [46] In the Doppler technique, the kinetic resolution of the fragments is limited by the spectral width of lasers, this yields a resolution on the order of about 1800 m/s when it was used commonly.[47-49] Mons and Dimicoli proposed an alternative technique in 1986, based on the temporal profile of the ion current of the fragment, after ionization using Resonance Enhanced Multiphoton Ionization (REMPI).[50] In this scheme as described in Chapter 2.3.2.1, two or more photons are used to ionize the molecule. The first (pump) pulse excites the molecule to a bound excited state, the second (probe) ionizes the molecule. By using a polarized source, analyzing the ion current as a function of arrival time of the ions can yield the angular distribution of the fragments. By altering the polarization of the probe laser pulse, one can identify the $\vec{v} - \vec{J}$ correlation through the differences in the time-of-flight (TOF) profile.[51] Using this technique the resolution of the kinetic energies of the fragments can be enhanced to 260 m/s as reported by Mons and Dimicoli.

1.5.2 Photoion imaging

Ion imaging introduced by Chandler and Houston [52] ionizes the entire Newton sphere of the fragments and then accelerates the photoions along a time of flight mass spectrometer, much in the same way as done in photofragment TOF profiling. The ions are then captured on a position sensitive detector. This technique had the advantage over Doppler profiling as it avoids the need for ultrahigh-resolution lasers.[53]

The ion imaging set up, is a combination of REMPI and a modified Wiley-McLaren time of flight spectrometer, see Figure 1.15.

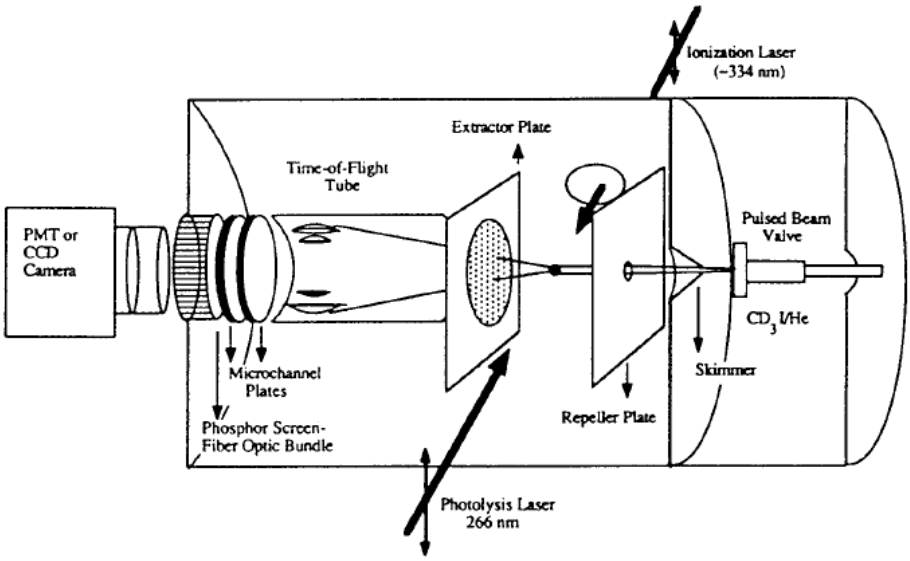

Figure 1.15: Ion imaging apparatus, reproduced from Sato[1].

A molecular beam of the sample and a carrier gas is introduced into the system through a pulsed valve. Counter propagating dissociation and ionization lasers enter the chamber perpendicular to the molecular beam. The REMPI technique allows for state-selective ionization of one of the fragments, which is then accelerated along the time-of-flight axis by the electric potential applied to the extractor and repeller plates. A grid in the extractor plate allows for the ions to pass through the extractor electrode while maintaining a near-homogenous electric field. The Newton sphere which is now ionized will maintain the angular distribution information. After it travels along the time of flight mass spectrometer it is projected onto the position-sensitive detector where the Newton sphere is detected as a disk with radius:

$$R = v_y \times TOF = \left(\frac{2E_k}{m/q} \right)^{1/2} \times TOF \tag{1.33}$$

Here, E_k is the kinetic energy of the fragment, and m/q is the mass to charge ratio of the fragment.[54] The position-sensitive detector is typically gated (turned on only when a photoion of a selected mass arrives) and is used to capture the two dimensional representation of the photofragment sphere. From this projection the angular distribution and anisotropy parameters can be found.

The major drawback to ion imaging is the lack of resolution of the ion cloud, since the electrostatic grid used to accelerate the ions introduces a blurring of the spatial distribution. To resolve this issue Eppink and Parker[5] introduced a new technique known as Velocity Map Imaging (VMI). They removed the grid and instead used an electrostatic lens, consisting essentially of the same electrode plates as in ion imaging although now with 20 mm clear holes and without grids. This introduces an inhomogeneity into the electric field which, when set correctly, causes the ion image to have a radius of:

$$R = N \times v_y \times TOF \tag{1.34}$$

where N is a magnification constant. Unfortunately this means that the direct relation between TOF and the radius is lost. This however, is accounted for as N is easily determinable for most apparatus. Removing the grids has the effect of eliminating the interaction volume blurring that was found in the ion-imaging apparatus and an increase in resolution of up to 20-fold can be achieved.[55, 56]

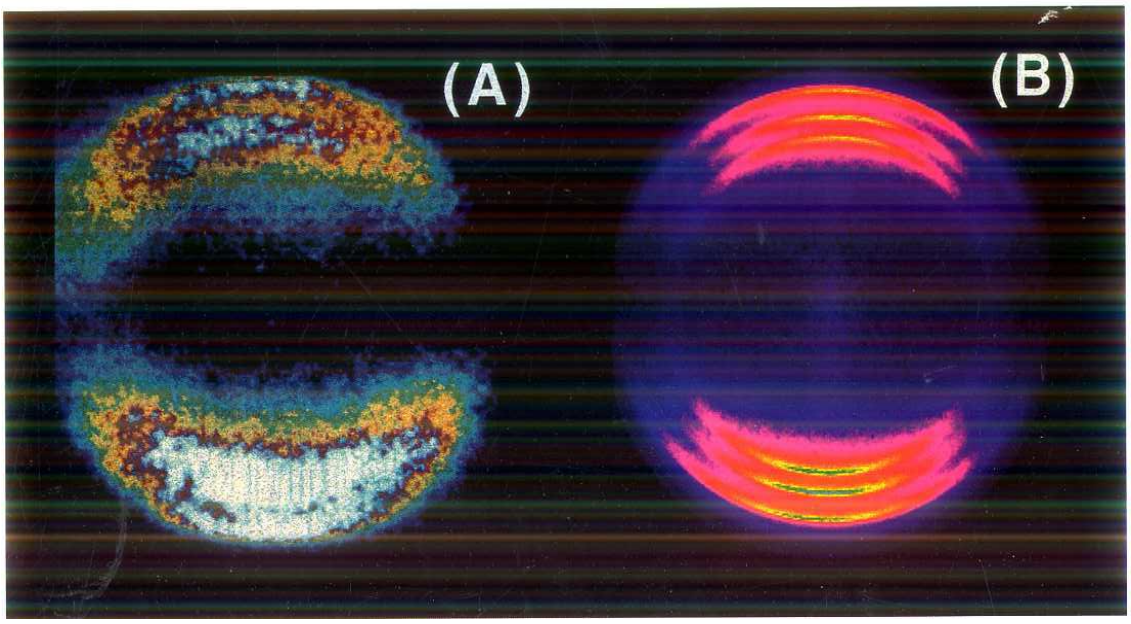

Figure 1.16: Images of the CH_3 fragment, following dissociation of CH_3I at 266 nm, using A ion-imaging and B, Velocity Map Imaging. Reproduced from Velocity Mapping of Multiphoton Excited Molecules, Advances in Photochemistry, Vol 25 Chandler and Parker.[56]

Several criteria must be satisfied such that the radial displacement from the centre of the image remains linear with the radial velocities of the fragments, known as VMI conditions.

1. The ions' radial displacement from the centre needs to scale linearly with the radial velocities and
2. The VM condition has to be fulfilled: ions having the same velocity but originating from different locations in the ionization volume are mapped to the same location at the detector plane.

Eppink and Parker in 1997 removed the distortions in the image caused by the grid electrodes used previously using plate electrodes that have a large hole within the extractor

and the ground plates.[5] A schematic is show below in Figure 1.17 (reproduced from Parker[5])

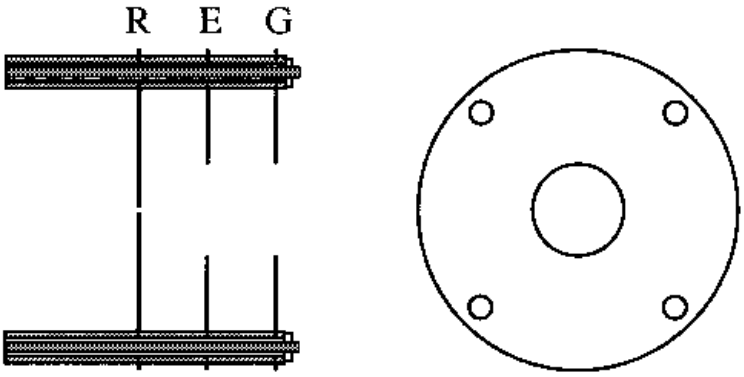

Figure 1.17:Eppink and Parker Velocity Map Imaging electrode design. Three steel plates are used as a repeller (R), extractor (E) and ground (G) electrodes. A small hole is used in the repeller to allow for sample introduction, and two larger holes in the extractor and ground plates, which induce an inhomogeneous electric field. Setting the plates to the appropriate charges will allow for the velocity mapping condition, where the inhomogeneity of the field causes the velocities of the ions to be mapped to specific locations at the detector.

This setup allows one to achieve the conditions outlined previously. 'Pancaking' of the ion cloud is achieved; as ions created further behind in the accelerating region reach a higher velocity component in the TOF direction, than those in front of it. This allows for the VMI condition along the time of flight axis. Equation 1.33 showed that the radius of the ring, *R,* is related to the cloud expansion speed v, linearly with the addition of a magnification factor. Finally, the Eppink-Parker setup induces a needed inhomogeneity in the electric field by the effect of the hole in the electrodes. Ions created closer to the edges of the hole experience a stronger field, and are accelerated more towards the center. If the potentials on the repeller and extractor electrodes are set correctly, this will allow for ions that were created in different positions along the x and y axis, to strike the detector at the same

location. Eppink and Parker demonstrated this effect computationally using the simulation program SIMION. Figure 1.18 has been reproduced from Parker.[5]

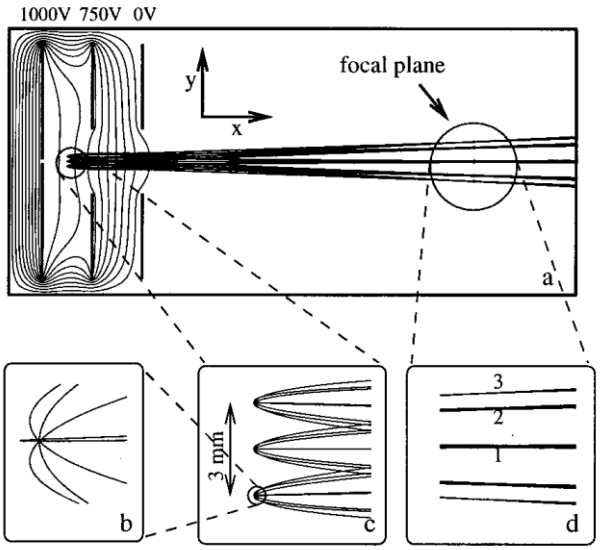

Figure 1.18:Ion trajectory simulation, of Eppink and Parker, with the repeller and extractor set to 1000 and 750V respectively. Velocity mapping is achieved at the focal plane, ions with the same velocity will map to the same location at the focal plane (d) regardless of where they were formed within the 3mm area (c).

Even when the voltages have been set up properly, there are still effects that reduce resolution. Detector resolution and space charge effects are two of the largest causes. Detector resolution is discussed later in Section 2.3.1.1. Space charge effects occur when the charges of the other ions affect the trajectory and position of one another. In a VMI setup this generally occurs at two possible locations. During the formation of ions in the ionization region, frequently a high density of ions is present which repel each other leading to image blurring. Another location for space charge effects is the region around the detector. When velocity mapping occurs, ions which have similar initial velocities will be focused to a small volume near the detector. These ions then repel one another and may activate multiple channels in the MCP.[54] In both cases space charge effects may be reduced by reducing the ionization rate, through lowering of the laser power of either pump

or probe laser. This of course has the obvious disadvantage that the experiment now takes longer.

While the Eppink-Parker design for VMI has been used successfully, there are other ion imaging techniques which seem to violate 'ion-pancaking' criteria. Specifically, slice imaging[57, 58] and 3D imaging[59] deliberately stretch the arrival time distribution of the ions. One can then obtain information on the third ion coordinate on the Newton sphere, i.e. the coordinate along the time-of flight axis.

With the application of femtosecond time-resolved techniques to molecular dynamics [60, 61] such as time-resolved photoelectron spectroscopy,[62] time-resolved photoelectron imaging (TRPEI) [63] and time-resolved ion imaging/VMI [64] along with time resolved coincidence experiments became possible.[65] These techniques have been applied to the study of NO_2 both with single colour [66] and two colour [67, 68] pump-probe experiments. Time-resolved studies utilize a different ionization technique than standard VMI due to the large linewidth inherent in their design. In a single colour pump-probe experiment, the fs-pulse is separated in time by an optical delay stage; it then intersects the molecular beam. The first pulse (pump) excites the ground state molecules to an excited state, shortly after the probe pulse ionizes it. Rather than stepping the laser from rotational line to rotational line as in a conventional VMI experiment, all of the populated rotational states in the excited molecule will be ionized. The dynamics of the species of interest are identified by varying the time delay between the pump and probe pulses.[63]

When designing the ion lens, the use of computational software is known to be a great resource. The program SIMION is used by many designers within the field.[5, 69, 70] Eppink and Parker showed in their paper that SIMION 6 was effective in simulating the

ion lens effectively. Currently the program is in its eighth edition, Version 8.1. In this work, SIMION 8.1 was used unless otherwise stated. An in-depth description of the velocity map imaging technique as well as the equipment needed for a successful experiment are described in Chapter 2.

CHAPTER 1 REFERENCES

[1] H. Sato, Photodissociation of Simple Molecules in the Gas Phase, Chem. Rev. 101 (2001) 2687-2725.

[2] F. Dominé, P.B. Shepson, Air-Snow Interactions and Atmospheric Chemistry, Science 297 (2002) 1506-1510.

[3] S. Li, J. Matthews, A. Sinha, Atmospheric Hydroxyl Radical Production from Electronically Excited NO_2 and H_2O, Science 319 (2008) 1657-1660.

[4] P.B. Ehrenfreund, A.; Gerakines, P.; Tielens, A.; van Dishoeck, Infrared Spectroscopy of interstellar apolar ice analogs, Astronomy and Astrophysics (1997) 649-669.

[5] A.T.J.B. Eppink, D.H. Parker, Velocity map imaging of ions and electrons using electrostatic lenses: Application in photoelectron and photofragment ion imaging of molecular oxygen, Review of Scientific Instruments 68 (1997) 3477-3484.

[6] C. Romanescu, H.-P. Loock, Proton formation in 2+1 resonance enhanced multiphoton excitation of HCl and HBr via (Ω=0) Rydberg and ion-pair states, The Journal of Chemical Physics 127 (2007) 124304.

[7] I. Wilkinson, B.J. Whitaker, Photodissociation of NO_2 in the $(2)^2B_2$ state: A slice imaging study and reinterpretation of previous results, The Journal of Chemical Physics 129 (2008) 154312.

[8] V. Blanchet, M.Z. Zgierski, T. Seideman, A. Stolow, Discerning vibronic molecular dynamics using time-resolved photoelectron spectroscopy, Nature 401 (1999) 52-54.

[9] O. Geßner, A.M.D. Lee, J.P. Shaffer, H. Reisler, S.V. Levchenko, A.I. Krylov, J.G. Underwood, H. Shi, A.L.L. East, D.M. Wardlaw, E.t.H. Chrysostom, C.C. Hayden, A.

Stolow, Femtosecond Multidimensional Imaging of a Molecular Dissociation, Science 311 (2006) 219-222.

[10] G. Marcotte, P. Marchand, S. Pronovost, P. Ayotte, C. Laffon, P. Parent, Surface-Enhanced Nitrate Photolysis on Ice, The Journal of Physical Chemistry A 119 (2015) 1996-2005.

[11] S.N. Wren, T.F. Kahan, K.B. Jumaa, D.J. Donaldson, Spectroscopic studies of the heterogeneous reaction between O_3(g) and halides at the surface of frozen salt solutions, Journal of Geophysical Research: Atmospheres 115 (2010).

[12] A. Yabushita, T. Hama, D. Iida, N. Kawanaka, M. Kawasaki, N. Watanabe, M.N.R. Ashfold, H.-P. Loock, Release of hydrogen molecules from the photodissociation of amorphous solid water and polycrystalline ice at 157 and 193nm, The Journal of Chemical Physics 129 (2008) 044501.

[13] A. Yabushita, Y. Inoue, T. Senga, M. Kawasaki, S. Sato, Photodissociation of Chlorine Molecules Adsorbed on Amorphous and Crystalline Water Ice Films, The Journal of Physical Chemistry B 106 (2002) 3151-3159.

[14] T.F. Kahan, D.J. Donaldson, Photolysis of Polycyclic Aromatic Hydrocarbons on Water and Ice Surfaces, The Journal of Physical Chemistry A 111 (2007) 1277-1285.

[15] M.P.A. Bernstein, L. J. Sandford, S. A., Complex Organics in Laboratory Simulations of Interstellar/Cometary Ices, Advances in Space Research 19 (1997) 991.

[16] P.B. Ehrenfreund, A.; Gerakines, P.; Tielens, A.; , Apolar ices, Faraday Discussions 109 (1998) 463-474.

[17] I. Wilkinson, B. J. Whitaker, Some remarks on the photodynamics of NO2, Annual Reports Section "C" (Physical Chemistry) 106 (2010) 274.

[18] R.D. McPeters, Climatology of Nitric-oxide in the Upper-Stratosphere, Mesosphere, and Thermosphere -1979 Through 1986, Journal of Geophysical Research, 94 (1989).

[19] H. Sato, Photodissociation of Simple Molecules in the Gas Phase, Chemical Reviews 101 (2001) 2687-2726.

[20] M. Ndour, B. D'Anna, C. George, O. Ka, Y. Balkanski, J. Kleffmann, K. Stemmler, M. Ammann, Photoenhanced uptake of NO2 on mineral dust: Laboratory experiments and model simulations, Geophysical Research Letters 35 (2008).

[21] L. Shuping, J. Matthews, A. Sinha, Atmospheric Hydroxyl Radical Production from Electronically Excited NO_2 and H_2O, Science 319 (2008).

[22] D.A. McQuarrie, Quantum Chemistry, University Science Books, USA, 2008.

[23] G. Herzberg, I. Spectra of Diatomic Molecules, Second ed., D. Van Nostrand, Canada, 1939, 1950.

[24] P.F. Bernath, Spectra of Atoms and Molecules, Oxford University Press, Inc.,, New York, New York, USA, 1995.

[25] J. Tellinghuisen, The Franck-Condon Principle in Bound-Free Transitions, Advances in Chemical Physics 60 (1985).

[26] G. Herzberg, Molecular Spectra and Molecular Structure, III. Electronic Spectra and Electronic Structure of Polyatomic Molecules, D. Van Nostrand Company, Canada, 1966.

[27] G. Herzberg, Molecular Spectra and Molecular Structure, II Infrared and Raman Spectra, D. Van Nostrand Company, Inc, Canada, 1945.

[28] C. Zener, Non-adiabatic crossing of energy levels, Proc. Roy. Soc. London Ser. A (1932) 696.

[29] C. Zener, Dissociation of Excited Diatomic Molecules by External Perturbations, Proc. Roy. Soc. London Ser. A (1933) 660.

[30] S.T. Pratt, Excited-state molecular photoionization dynamics, Rep. Prog. Phys. 58 (1995).

[31] H. Lefebvre-Brion, R.W. Field, The Spectra and Dynamics of Diatomic Molecules, Elsevier Inc., Netherlands, 2004.

[32] H. Lefebvre-Brion, R.W. Field, Perturbations in the Spectra of Diatomic Molecules, Elsevier, Netherlands, 2012.

[33] C. Romanescu, S. Manzhos, D. Boldovsky, J. Clarke, H.-P. Loock, Superexcited state reconstruction of HCl using photoelectron and photoion imaging, J. Chem. Phys. 120 (2004) 767-777.

[34] C. Romanescu, H.-P. Loock, Photoelectron imaging following 2 + 1 multiphoton excitation of HBr, Physical Chemistry Chemical Physics 8 (2006) 2940-2949.

[35] H. Lefebvre-Brion, F. Keller, Competition between autoionization and predissociation in the HCl and DCl molecules, J. Chem. Phys. 90 (1989) 7176.

[36] A.I. Chichinin, P.S. Shternin, N. Gödecke, S. Kauczok, C. Maul, O.S. Vasyutinskii, K.-H. Gericke, Intermediate state polarization in multiphoton ionization of HCl, J. Chem. Phys. 125 (2006) 034310.

[37] P.L. Houston, Vector Correlations In Photodissociation Dynamics, J. Chem. Phys 91 (1987) 5388-5397.

[38] R.N. Zare, Calculation of Intensity Distribution in the Vibrational Structure of Electronic Transitions: The B $^3\Pi_{0+u}$—X $^1\Sigma_{0+g}$ Resonance Series of Molecular Iodine, J. Chem. Phys. 40 (1964) 1934.

[39] C. Romanescu, PhD. Thesis, Queen's University (2007).

[40] J. Solomon, Photodissociation as Studied by Photolysis Mapping, J. Chem. Phys. 47 (1967) 889.

[41] G.E. Busch, Translational Spectroscopy: Cl2 Photodissociation, J. Chem. Phys. 51 (1969) 449.

[42] R.W. Diesen, Photochemical Recoil Spectroscopy, J. Chem. Phys. 50 (1969) 3635.

[43] R.N. Zare, D.R. Herschbach, Doppler Line Shape of Atomic Fluorescence Excited by Molecular Photodissociation, Proceedings of the IEEE (1963) 173-183.

[44] R.D. Levine, Molecular Reaction Dynamics, Cambridge University Press, UK, 2005.

[45] R. Schmiedl, H. Dugan, W. Meier, K.H. Welge, Laser Doppler spectroscopy of atomic hydrogen in the photodissociation of HI, Zeitschrift für Physik A Atoms and Nuclei 304 (1982) 137-142.

[46] R.N. Dixon, The determination of the vector correlation between photofragment rotational and translational motions from the analysis of Doppler-broadened spectral line profiles, J. Chem. Phys. 85 (1986) 1866.

[47] W.G. Wilson, K.S. Viswanathan, E. Sekreta, J.P. Reilly, Rotationally resolved laser photoelectron spectrum of gas-phase No, The Journal of Physical Chemistry 88 (1984) 672-673.

[48] W.C. Wiley, I.H. McLaren, Time-of-Flight Mass Spectrometer with Improved Resolution, Review of Scientific Instruments 26 (1955) 1150-1157.

[49] S.c. Yang, R. Bersohn, Theory of the angular distribution of molecular photofragments, J. Chem. Phys. 61 (1974) 4400-4407.

[50] M. Mons, I. Dimicoli, State Selective Kinetic Distribution of Photofragments, Chemical Physics Letters 131 (1986).

[51] J. Cao, H.P. Loock, C.X.W. Qian, The nonadiabatic photodissociation of BrNO at 355 nm, J. Chem. Phys. 101 (1994) 3395-3398.

[52] D.W. Chandler, P.L. Houston, Two-dimensional imaging of state-selected photodissociation products detected by multiphoton ionization, J. Chem. Phys. 87 (1987) 1445.

[53] P.L. Houston, J Phys Chem 100 (1996) 12757-12770.

[54] H. D., Parker, A. T. J. B. Eppink, Velocity map imaging: applications in molecular dynamics and experimental aspects, in: B.J. Whitaker (Ed.), Imaging in Molecular Dynamics Technology and Applications, Cambridge University Press, Cambridge, 2003, pp. 20-64.

[55] A.T.J.B. Eppink, D.H. Parker, Energy partitioning following photodissociation of methyl iodide in the A band: A velocity mapping study, The Journal of Chemical Physics 110 (1999) 832.

[56] D.W.a.P. Chandler, David H., Velocity Mapping of Multiphoton Excited Molecules, in Advances in Photochemistry, Volume 25 (eds D. C. Neckers, D. H. Volman and G. Von Bünau), John Wiley & Sons, Inc., Hoboken, NJ, USA. 1999.

[57] A.G. Suits, Continetti, R. E, Imaging in Chemical Dynamics, ACS Symposium series, Washington, 2001.

[58] D. Townsend, M.P. Minitti, A.G. Suits, Direct current slice imaging, Review of Scientific Instruments 74 (2003) 2530.

[59] A.I. Chichinin, Einfeld, T. S., Gericke, K.H., Maul, Christof, 3-D Imaging technique - observation of the three-dimensional product momentum distribution, in: B.J. Whitaker (Ed.), Imaging in Molecular Dynamics, Technology and Applications, Cabridge University Press, New york, USA, 2003.

[60] A.H. Zewail, Femtochemistry: Recent Progress in Studies of Dynamics and Control of Reactions and Their Transition States, The Journal of Physical Chemistry 100 (1996) 12701-12724.

[61] A.H. Zewail, Femtochemistry: Atomic-Scale Dynamics of the Chemical Bond†, The Journal of Physical Chemistry A 104 (2000) 5660-5694.

[62] A. Stolow, A.E. Bragg, D.M. Neumark, Femtosecond Time-Resolved Photoelectron Spectroscopy, Chemical Reviews 104 (2004) 1719-1758.

[63] L. Wang, H. Kohguchi, T. Suzuki, Femtosecond time-resolved photoelectron imaging, Faraday Discussions 113 (1999) 37-46.

[64] T. Shibata, T. Suzuki, Photofragment ion imaging with femtosecond laser pulses, Chemical Physics Letters 262 (1996) 115-119.

[65] P. Hockett, E. Ripani, A. Rytwinski, A. Stolow, Probing ultrafast dynamics with time-resolved multi-dimensional coincidence imaging: butadiene, Journal of Modern Optics 60 (2013) 1409-1425.

[66] J.A. Davies, R.E. Continetti, D.W. Chandler, C.C. Hayden, Femtosecond Time-Resolved Photoelectron Angular Distributions Probed during Photodissociation of NO_2, Physical Review Letters 84 (2000) 5983-5986.

[67] A. Vredenborg, W.G. Roeterdink, M.H.M. Janssen, Femtosecond time-resolved photoelectron-photoion coincidence imaging of multiphoton multichannel photodynamics in NO2, J. Chem. Phys. 128 (2008) 204311.

[68] A.T.J.B. Eppink, B.J. Whitaker, E. Gloaguen, B. Soep, A.M. Coroiu, D.H. Parker, Dissociative multiphoton ionization of NO2 studied by time-resolved imaging, J. Chem. Phys. 121 (2004) 7776-7783.

[69] M.D. Kershis, D.P. Wilson, M.G. White, J.J. John, A. Nomerotski, M. Brouard, J.W. Lee, C. Vallance, R. Turchetta, Exploring surface photoreaction dynamics using pixel imaging mass spectrometry (PImMS), J Chem Phys 139 (2013) 084202.

[70] N.G. Kling, D. Paul, A. Gura, G. Laurent, S. De, H. Li, Z. Wang, B. Ahn, C.H. Kim, T.K. Kim, I.V. Litvinyuk, C.L. Cocke, I. Ben-Itzhak, D. Kim, M.F. Kling, Thick-lens velocity-map imaging spectrometer with high resolution for high-energy charged particles, Journal of Instrumentation 9 (2014) P05005-P05005.

Chapter 2

Designing a Time of Flight Mass Spectrometer for Velocity Map Imaging

2.1 Introduction

As mentioned in Chapter 1, during a velocity map imaging experiment the velocities of molecular or atomic fragments are measured following a reactive event. Using state-selective ionization, energy conservation and momentum conservation of the photofragment species, a VMI experiment can determine the complete quantum state distribution and angular distribution of all photofragments. Four main steps are needed for a successful velocity map imaging experiment. The first step is the creation of neutral fragments, which travel outward in many directions; this expanding sphere is known as a Newton sphere. In the second step the fragments are ionized quantum state-selectively. Third, the now ionic Newton spheres must be projected onto a 2D detector; and, finally, the 2D images must be analyzed or converted into a 3D ion distribution. In this chapter, we describe the equipment that is used to extract this information. This chapter is intended to give the reader an introduction to Velocity Map Imaging before describing the Condensed Phase Velocity Map Imaging apparatus in Chapter 3.

2.2 The Velocity Map Imaging Apparatus

A velocity map imaging system is a multicomponent apparatus in which samples are prepared; reactions are initiated, probed, and then detected. The following sections describe an overview of the components involved in these steps. The figure below describes our VMI setup.

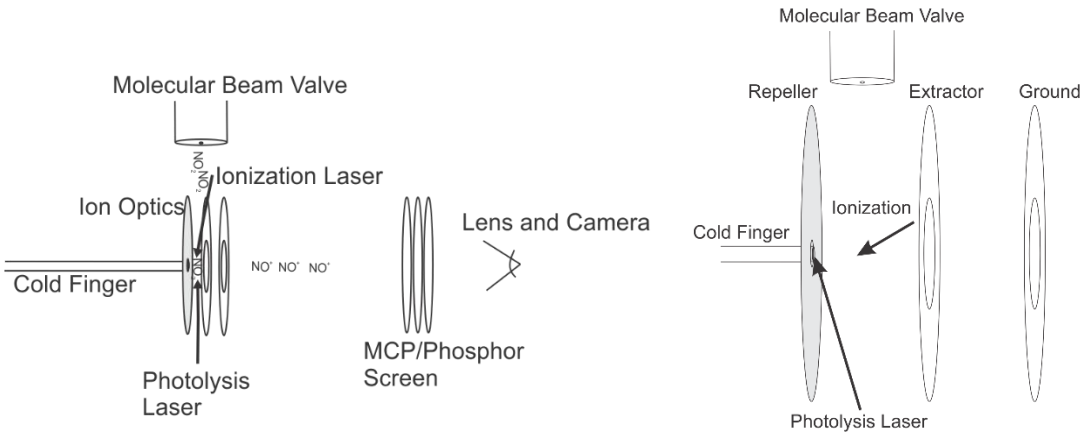

Figure 2.1:Left: Velocity map imaging setup; the sample is introduced through a molecular beam valve, photolysis and ionization occur between the charged repeller and extractor plates, which accelerate the ions along the flight tube. The ions are then detected at the position sensitive microchannel plate detector. The camera takes the resulting image of the phosphor screen. Right: Enlarged schematic of the ion optic section, with lasers aligned for a condensed phase experiment. In the gas phase set up, the photolysis laser is aligned between the repeller and extractor electrodes.

2.2.1 Materials and design

Our VMI machine is separated into two sections, a beam side and a time-of-flight side, via a gate valve (Edwards, GVC 060M). The beam side consists of a turbo molecular pump (Varian, TV 701) which is backed by a roughing pump (Edwards, E2M40) and the molecular beam valve (Parker) in which the sample enters. The cold finger attachment freezes the sample if desired. MgF_2 windows are placed on either side of the electrodes and allow for the laser beams to enter from either side of the chamber; finally, the electrodes form the VMI lens. The time of flight side of the machine contains a second turbo pump (Pfeiffer TMU-521) which is backed by a roughing pump (Edwards 12) as well as the TOF tube, which contains a μ-metal that is inserted into the outer stainless steel chamber. The μ-metal is a nickel-iron alloy (77 and 16% respectively) containing 5% copper and 2% chromium. The magnetic permeability of this alloy shields external magnetic fields which

otherwise may alter the trajectories of the ions. There are other alloys which have similar permeabilities however μ-metal is also quite ductile and can be made into sheets and tubes.[1] The TOF side of the system also contains the detector unit, comprised of two chevron stacked multichannel plates (Photonis), and a photosensitive phosphorus screen. The entire system is built of stainless steel with copper o-rings (Kurt J Leskar), to maintain high vacuum (10^{-6} - 10^{-7} Torr) between the separate connections.

2.2.2 Achieving High Vacuum

Vacuum is obtained through a two stage process involving two oil-sealed rotary vane pumps. These pumps are used to obtain pressures of a few millitorr, and contain a spring loaded vane system which is rotated via a rotor. The vanes within the chamber form two oiled sealed compartments, gas enters in one side and is forced out through a one way valve to an exhaust. This process depletes the oil within the pump slowly as some droplets are released through the exhaust and must be routinely refilled with oil over time.

The second stage of pumping uses turbomolecular pumps also known as turbo pumps. In our set up, these turbo pumps can reach pressures as low as 5×10^{-7} Torr. Similar to a jet turbine engine, a series of angled blades are turned on a common shaft at high speeds (upwards of 90000 rpm). The edges of the blades approach molecular speeds, and when a molecule strikes them they are accelerated towards the exhaust. A key aspect of turbomolecular pump design is the orientation of the blades with respect to the rotor which achieves a compression of molecules before they are sent on to the next set of blades and ultimately the exhaust. This detail means that the pumping efficiency is related to the molecular mass of the gas being pumped. The logarithm of the compression ratio is

proportional to the square of the molecular weight. As such heavy molecules, such as oil from the vane pump are strongly pumped away achieving an oil free vacuum system.[2]

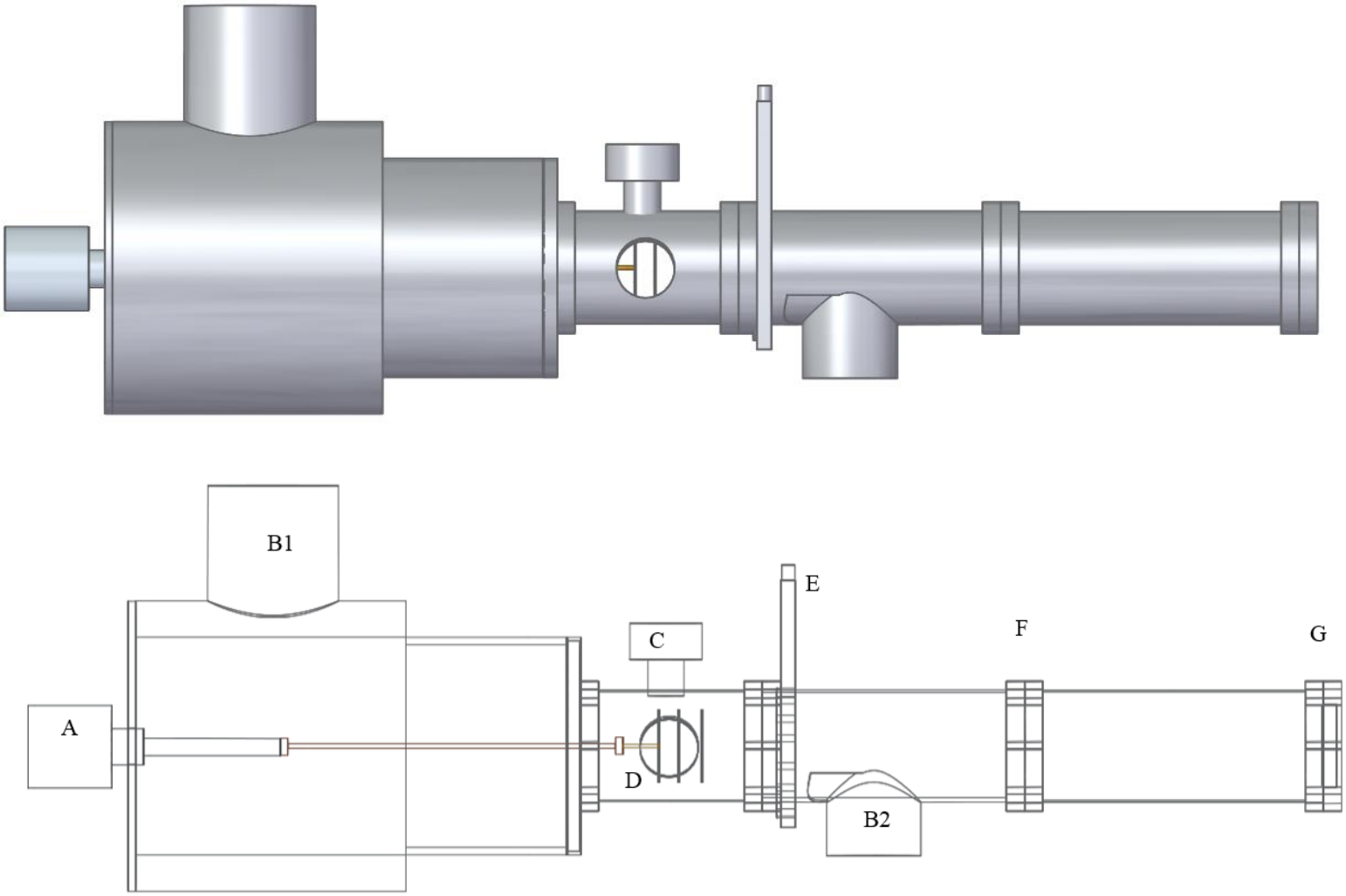

Figure 2.2:Top: CAD image of the VMI apparatus. Below: Wire diagram, A) Cold head and Expander, B1/B2) Turbomolecular Pumps C) Molecular Beam valve, D) Cold Finger and Ion optics, E) Gate Valve, F) Time of flight chamber, G) MCP and Phosphor screen. Gas preparation line and camera not shown.

2.2.3 Sample Preparation

Sample preparation is usually done within a stainless steel gas line known as a mixing chamber. Specifics of our sample preparation are described in chapter 3.2.1.

2.2.4 Molecular Beam Valve

Once the mixture is prepared, a valve connecting the mixing chamber to a molecular beam valve is opened. The molecular beam is directed perpendicular to the time-of-flight axis as shown in the Figure 2.2 The beam valve is driven by a pulse driver, (Parker, Iota One). When voltage is applied to the valve, the valve is opened typically for 200-230 μs, and is operated at 10 Hz. Timing of the valve is controlled through the delay generator (Stanford Research Systems DG 535). The specific details about the timing are discussed in Chapter 3.3.2. In a conventional VMI experiment the molecular beam then passes through a skimmer. This ensures that molecules which are not traveling parallel (or perpendicular, if the valve is mounted as such) to the time of flight axis are removed. The molecules then enter the ionization region through a hole in the repeller plate. (In our system however, the molecules are frozen onto the cold surface, as such no skimmer is needed.)

2.2.5 Ion Optics and Ionization

The molecular beam axis is perpendicular to both dissociation and ionization beams which are usually collinear and counter-propagating. The overlap of the photo-fragments and the ionization beam forms the ionization region. For fast-moving fragments, the delay between dissociation and ionization laser pulses may mean that the Newton spheres will have expanded to a larger diameter than the ionization region, this is known as “fly-out”.

However, as the dissociation beam is larger than the ionization region other fragments will have entered the ionization region, just as some have left, and overall a full Newton sphere will be probed [3] (See Figure 2.3).

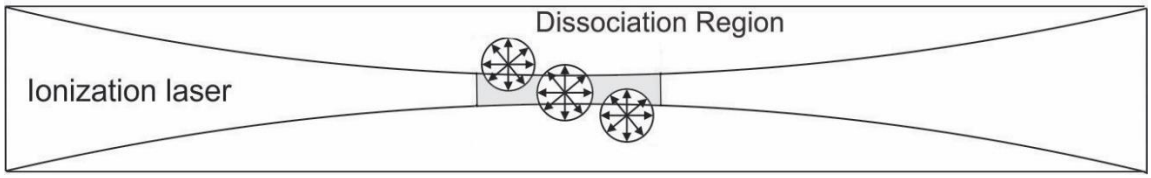

Figure 2.3: The dissociation region is defined as the entire encapsulated region, while the ionization region is defined by the grey area. Although the Newton sphere of a single event (separate spheres of arrows) may have grown larger than the ionization region if it was formed in the ionization region, components of others spheres formed just outside of the ionization region will enter the ionization region and lead to all components of the sphere being ionized and imaged.

There are two other ways of forming a Newton sphere, the first is to use the same beam for dissociation and ionization. This technique demands that the laser can dissociate the molecule into neutral fragments at a wavelength that can also be used for state-selective ionization. As it is a single pulse technique, dissociation and ionization occur on the timescale of the laser pulse. This means that light and fast neutral fragments formed at the edge of the ionization region traveling perpendicular to the laser beam may exit the region before being ionized and not be imaged. Bimolecular scattering can also be used; this technique involves two molecular beams intersecting one another, where collisions fragment the species of interest. They are then ionized and detected.[3] All of our experiments were conducted using laser dissociation followed by ionization from a second laser unless otherwise stated. A more detailed description of dissociation, ionization techniques, as well as the equipment needed is discussed in the Section 2.3.

2.2.5.1 Laser Systems

Two main steps of the VMI process require laser action, photodissociation and photoionization. For dissociation both the third harmonic of a neodymium yttrium aluminum garnet (Nd:YAG) laser at 355 nm as well as a frequency-doubled optical parametric oscillator (OPO) system are used. State selective ionization of the molecules is done with a second laser system – an excimer pumped dye laser system which is frequency doubled for a tunable output between 216 and 237.5 nm using Coumarin 450 as the dye. The following section describes the laser dissociation process, and gives an overview of optical parametric oscillation.

2.2.5.2 Dissociation Laser

Photodissociative experiments are initiated with a laser pulse. The type of laser employed can vary to suit the requirements of the reaction being explored. Time-resolved reactions utilize femtosecond pulses and require specialized laser systems such as Titanium-sapphire (Ti-Sapph) laser systems.[4] These systems have also been used to control the reaction dynamics using strong-field pulses.[5] In other studies dye lasers and Nd-YAG systems with pulse lengths of 5-15 ns are used.[6-8] In our experiments the third harmonic of the Nd:YAG laser is typically used for photolysis; alternatively, a Nd:YAG-pumped OPO laser was occasionally used for dissociation in experiments at other wavelengths. An OPO laser is tunable over a large range of frequencies and is ideal for survey studies since it does not require changing dyes and realignment as is common with dye lasers. In the past the key disadvantage of an OPO came from the loss of spectral resolution.[9] Until the early 2000's

[10-13] the best OPO lasers had a linewidth of ≈ 1-2 nm compared to 0.002 nm of a dye laser at comparable cost.[9] However, OPO lasers have improved and comparable, 0.03 nm linewidth, are now available at similar cost.[14] In any case this disadvantage is not as relevant for the purpose of this thesis since high spectral resolution is not required for the photodissociation process. The output beam of the OPO or Nd-YAG laser is focused using a lens with a 30 cm focal length into the chamber and the Ar-matrix is irradiated at roughly 35^{o} to the surface.

2.2.5.2.1 OPO Operational Principles

An Optical Parametric Oscillator (OPO) is, by a strict definition, not a laser. Rather than using stimulated emission, parametric oscillation is used to yield a coherent light source. Parametric oscillation, a nonlinear optical process, occurs during second harmonic generation. A beam of frequency ω passes through a nonlinear crystal such as β-barium borate, which then converts the beam into a frequency of 2ω. Additionally it is possible to achieve what is known as sum-difference frequency splitting whereby two new pulses may be formed from one pulse according to energy conservation

$$\omega_1 = \omega_2 + \omega_3 \tag{2.1}$$

Here ω_1 is the frequency of the pump beam, ω_3 is known as the signal frequency, and ω_2 the idler frequency. Like a laser, an OPO requires a threshold for the pump laser before appreciable output power is reached. However, it is important that the pump source is already fairly coherent. This necessitates the need for a laser source to be used as the driving source for the OPO itself.

A detailed description of nonlinear optics is outside the realm of this thesis, however; for further reading the reader is recommended to read Webb.[15]

2.2.5.2.2 Nd-YAG Pump

As mentioned above, a pump laser is needed for the operation of an OPO system. This is achieved by using a Nd-YAG laser (Spectra physics HD-INDI) 100 mJ cm^{-2} with a pulse width of 8 ns at 10 Hz repetition rate. Additionally, for many experiments the third harmonic of a different Nd-YAG (Continuum Powerlite Precision 8000, 150 mJ cm^{-2}) at 355 nm and with power lowered to 5 mJ/cm^2 is used directly for dissociation. The gain medium of the Nd-YAG laser is a solid crystalline rod made from an yttrium aluminum garnet crystal that is doped with Nd^{3+} ions. The material forms the gain element in a four level laser system. The ground state of the laser system is the $^4I_{9/2}$ state; from there the $^4F_{5/2}$ state is populated via excitation from a Xe flashlamp. After excitation to the $^4F_{5/2}$ state the Nd ions relax to the $^4F_{3/2}$ state which forms the upper state of the lasing transition. The fluorescence lifetime of the state $^4F_{3/2}$ to the $^4I_{11/2}$ state is on the order of 200 μs, emitting light at 1064 nm. The $^4I_{11/2}$ state then quickly relaxes to the ground vibrational state, thereby creating the required population inversion.

As flashlamp emission does not perfectly match the $^4F_{5/2} \leftarrow {}^4I_{9/2}$, transition, lamp-pumped Nd:YAG lasers are relatively inefficient, since only 0.1-1% electrical to light energy conversion is achieved. Pumping with GaAlAs diode lasers, however, allows for 15-20% "wall-plug efficiency".[16]

The infrared emission of an Nd-YAG can be easily converted by SHG into visible (532 nm) and by THG to the ultraviolet (355 nm) region of the spectrum. Here, the light formed at 355 nm is used to pump the OPO system mentioned above.

2.2.6 Ionization

In a successful VMI experiment, the ionization step is the next critical event that occurs following dissociation. As it occurs quickly following the dissociation step, any perturbation it has on the Newton sphere will drastically interfere with the results of the experiment. Ideally, any ionization scheme used for VMI will achieve two goals. Firstly, ionization should be done without changing the velocities of the fragments which obviously, is impossible to be realized perfectly (the recoil from the ejected electron may alter the photofragments' velocities).[17] Secondly, the ions should be formed state-selectively, if that level of resolution is desired. In order to satisfy these two requirements to the greatest degree, Resonance Enhanced Multiphoton Ionization (REMPI) has been used very frequently in VMI experiments.[3]

2.2.6.1 Dye laser

While OPOs are tunable over a wide wavelength range, their linewidth does not permit spectroscopy in many cases. For pulsed excitation processes in the visible and UV region of the spectrum, tunable dye lasers remain the most common light source.[18, 19] Alternatively, Ti:sapphire lasers have been used for time-resolved photoelectron and

photoion imaging.[20-22] They are primarily used when one is working in the ultrafast realm or in high-field studies as mentioned in Chapter 1.

In the Loock laboratory a frequency-doubled dye laser (Scanmate 2E) is used to generate the REMPI beam. For any laser dye, the tunable range is approximated by the fluorescence range of the given dye, i.e. usually 20-30 nm. If a different range is needed, one must change the dye being used. This tunability over 20 nm is sufficient to cover a rovibrational band system for most small molecules, with the exception of molecular hydrogen, H_2 and its isotopomers.

The Scanmate 2E laser has a narrow linewidth of 0.15 cm^{-1} at 450 nm, which corresponds to a line resolution of 3 pm. This line resolution increases further after going through the second harmonic generator. This gives a reasonable step size of 2 pm when scanning the laser over the band system. This resolution is well within the range needed for REMPI to be used as most bands are several pm in width.

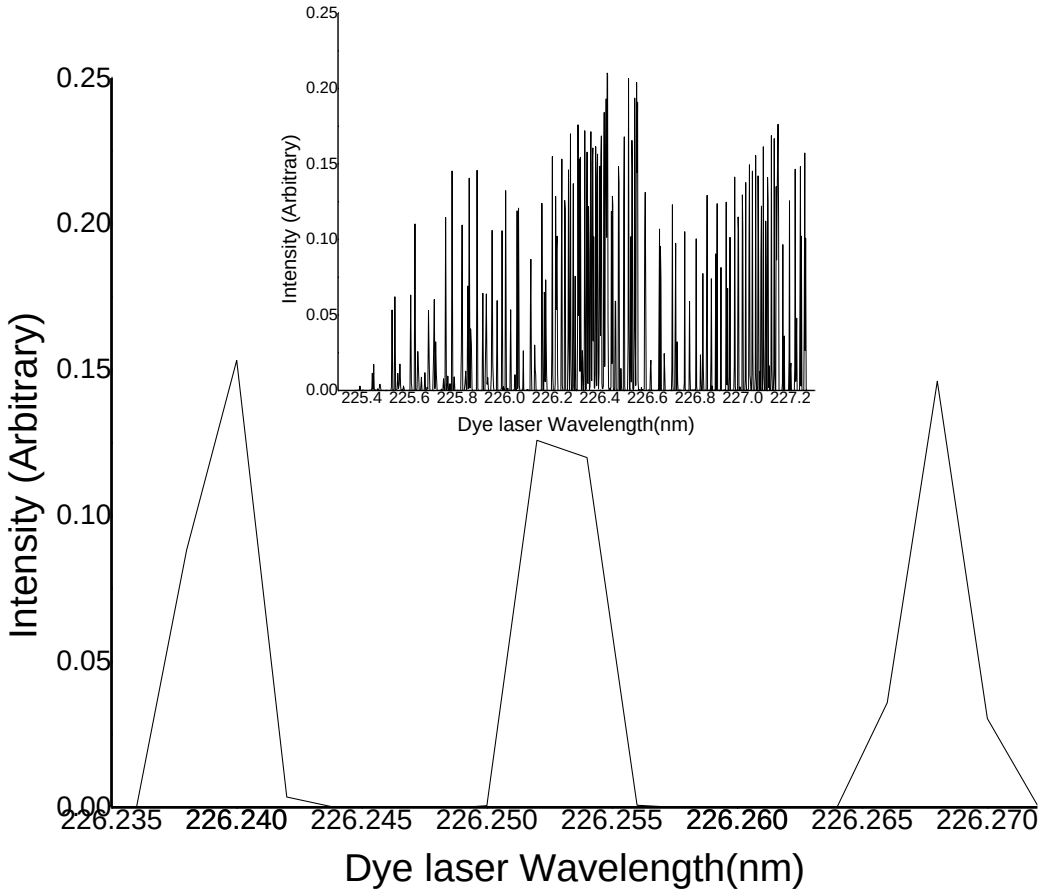

Figure 2.4:Enlarged region of the 1+1 REMPI spectrum NO $^2\Sigma_{1/2}(v'=0) \leftarrow {}^2\Pi_{3/2}(v''=0)$. It is clear that the lines of the rovibrational transitions have a width of close to 6 pm. The inset shows the full 1+1 REMPI spectrum $^2\Sigma_{1/2}(v'=0) \leftarrow {}^2\Pi_{3/2,1/2}(v''=0)$ of gas phase NO following dissociation with the same pulse.

2.2.6.1.1 Structure and Properties of Laser Dyes

As the gain medium for a dye laser, the selection of the dye is of obvious importance. The early development of dye lasers also corresponded with the discovery of many laser dyes. One of the most frequently used dyes, Rhodamine 6G, was discovered in the early days of dye laser development.[23] Laser dyes are usually characterized by their large visible and near ultraviolet absorption bands as well as their wide fluorescence emission. Dyes pose

an interesting problem as the light absorption is very difficult to derive based on their structure alone.[24] There are, however, several simple models that have been found to explain the experimental observations.

The high energy absorption of laser dyes from the ground, S_o, to the excited state, S_1, is attributed to the fact that this transition has a large transition strength leading to an oscillator strength in dye molecules close to one.[15, 24] Similarly, the fluorescence emission which corresponds to the stimulated emission of the laser, from S_1 to S_o, has a large spontaneous emission leading to a large gain in the laser. After the molecules in the ground state are excited to the upper, S_1 state they populate several of the vibronic states. Within picoseconds these relax to the lowest state in the S_1 manifold. For optimal lasing efficiency they would remain in this state until the stimulated emission event. There are of course different nonradiative transitions that occur and reduce the emission. Several of these pathways are due to the structure of the dye molecule as well as the interaction with the solvent. These pathways are usually attributed to two different types of processes, internal conversion, that is direct relaxation to the ground state S_o, or intersystem crossing into the triplet state, T_1. A schematic of these dye laser transitions is shown below.

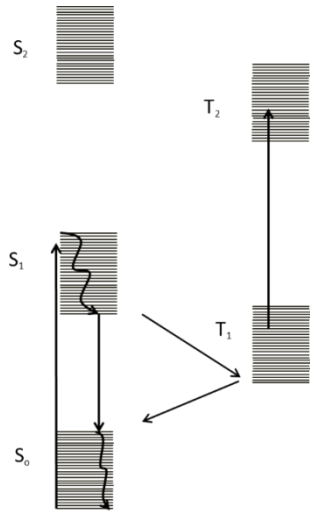

Figure 2.5:Energy level diagram from a typical dye laser. Straight arrows correspond to radiative transitions, curved arrows to non-radiative transition and diagonal arrows to the intersystem crossing. The radiative transitions from S_1 to S_0 are the transitions that result in the fluorescence of the molecule.

In the experiments that were performed in this thesis, coumarin dyes were used exclusively unless otherwise stated. As such, a description of some of the particular aspects of this class of dyes will be discussed.

Coumarin-based dyes, are ideally suited for the study of NO ionization as they emit in the blue green, a typical dye curve of 440 to 460 nm allows for easy doubling into the 220-230 nm range if the right derivative is used. Additionally, the absorption cross section at 308 nm is fairly high and thus can be pumped with a XeCl excimer laser. When coumarin 460 (dissolved in methanol, with a coumarin concentration 1.6 g/L) is excited with an XeCl excimer, a peak at 456 nm and a range of 440-484 nm with a 18% efficiency can be observed.[25]

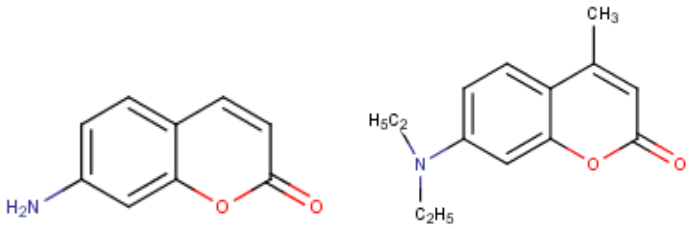

Figure 2.6: Coumarin (Left) and Coumarin 460 (Right), typical dye used for production of blue light in a dye laser, it is used frequently within this thesis.

2.2.6.1.2 Dye Laser Principles and Configuration

The Scanmate 2E has a transverse configuration; the pump light enters the cavity perpendicular to the output beam axis and passes through a cylindrical lens. The dye solution will attenuate the beam quickly and population inversion is achieved within a thin volume behind the cuvette wall. As the beam will be highly divergent in this set up, it is telescoped by lenses into a parallel beam, and expanded onto a Littrow grating. This setup is known as a Hansch-type arrangement. The Scanmate 2E laser uses this Hansch arrangement, with some extra specifications known as the LambdaPure® setup.[26]

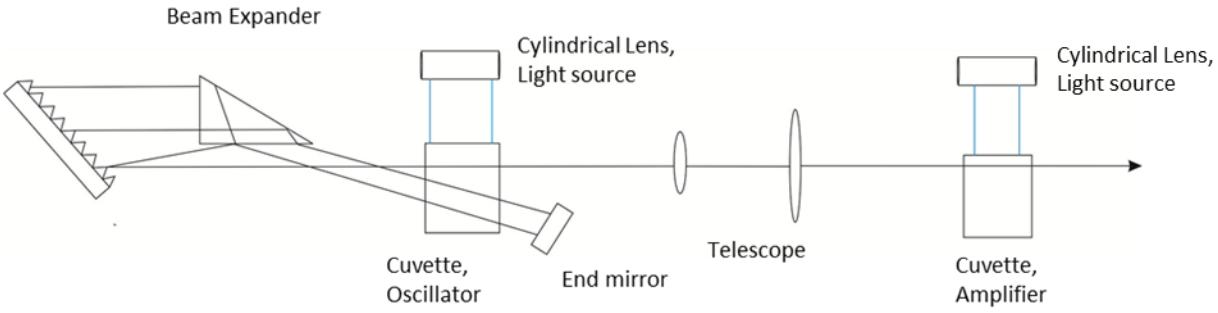

Figure 2.7: Lambda Physik "Super Pure" design. The addition of a main amplifier and the end mirror allows for reduction of amplified spontaneous emmision, while maintaining intensity. The increase in beam quality does, however, come at a cost of a more laborious alignment.

2.3 Data Collection

In velocity map imaging, the fragments' velocity is obtained by analyzing the image that the photoions form on the position sensitive detector. On the other hand, the arrival times of the ions at the detector also contain useful information about their mass and number. This signal is obtained by interrogating the restoring current on the multichannel plate. The amplitude of the restoring current is linearly proportional to the number of ions which reach the detector at that time. The restoring current is obtained with a Butterworth filter, which splits some of the restoring current from the power supplies and sends it to the oscilloscope. It was built by previous members of the Loock Lab, [27] and is connected to an oscilloscope which can be read by the PC. This allows us to obtain a REMPI spectrum when the dye laser is scanned through the rovibrational band. Additionally, one can measure the ion signal as a function of the time delay between the dissociation and ionization laser pulse. If the focus of the pump laser and of the probe laser are spatially displaced, the delay time contains information about the translational energy of the photofragments, as the photofragments would have to traverse this distance within the delay time of the laser pulses.

The data therefore have several "dimensions": VMI data yields information on photofragment velocities, the REMPI spectrum contains relative populations of the respective ro-vibrational states, the arrival time contain the masses of the photofragments, and the pump-probe delay time data contains additional information on the fragment kinetic energies and the energy partitioning into the matrix.

2.3.1 Velocity Map Image Creation

The velocity map image is created by capturing the display from the detector; the detector itself is a multicomponent device. This section describes the MCP (microchannel plate), phosphor screen, CMOS camera, and the program used to collect the images from the camera. Figure 2.8 shows a schematic of the detector setup.

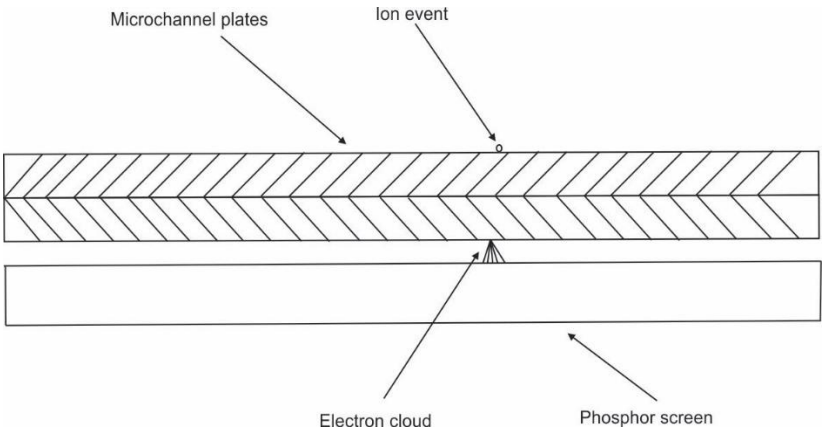

Figure 2.8: Detector assembly: Two coupled MCPs charged with a shared voltage of 2000 V; the ion hitting the MCP leads to an electron cascade which eventually leads to an electron cloud hitting the phosphor screen. This process emits photons at the same position as the ion that hit the MCP.

2.3.1.1 Microchannel Plates

The detector consists of two Microchannel plates, (Burle, now Photonis) which are used to detect and amplify single ions by turning them into easily detectable electrical and visual signals. The plates are 1 mm thick and 75 mm in diameter, consisting of an array of micron-sized diameter channels, the walls of which are at an angular bias to the front face of the detector. This ensures that the ions will hit the walls of the channels. High voltage is applied across these channels. When a particle hits the wall of the channel, multiple electrons are emitted. These secondary electrons then continue to travel down the channel, impinging upon the surface releasing more electrons. The potential bias means that the electrons are

accelerated towards the exit of the channel, at which point the amplification will have increased to 10^3 for a single MCP. In a chevron stack, as used in this work, amplification can reach up to 10^5-10^6. The electron cloud then hits the phosphor screen which causes localized light emission, which is captured from the camera.

Additionally, switching the voltage across the two MCPs allows for gating of the MCP detector. An oscilloscope is used to identify the timing gate needed to capture the ion's mass/charge (m/z) ratio. A delay timer (Stanford Research DG 535) is used to switch one of the MCPs from a low voltage state, which cannot induce an electron cascade, to a higher voltage state, which allows ion detection at the selected time. This eliminates most of the background signal and allows for selection of only the mass peak of interest.

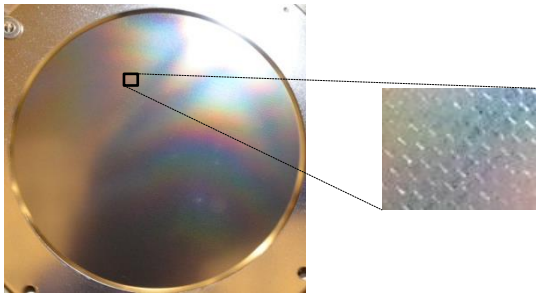

Figure 2.9:Image of a microchannel plate with digitally enlarged segment highlighting the hexagonal channel structure.

2.3.1.2 Phosphor Screen

The phosphor screen is used to convert the electrons ejected from the MCP into light such that they can be captured by the camera. The P45 phosphor screen employed in the experiments uses Y2O2S:Tb as the active material with emission centered at 545 nm. It

has a short persistence, less than 1.5 ms [28] which allows for observation of images on the times scales needed.

2.3.1.3 CMOS Camera

The phosphor screen is captured using a CMOS camera (Point Grey, Flea3) fitted with an adjustable camera lens. The phosphor screen and the camera are shielded from external light through a large thick cloth. The camera is triggered by the camera data collection software built using LabVIEW and the exposure length is controlled such that only one dissociation event is collected per frame. Data transfer is performed through a USB3 connection at 6 Gbits/second allowing for transfer of the image to the computer before a second image needs to be collected.

2.3.1.4 Camera Data Collection

The camera is controlled through a home-made LabVIEW program. An external trigger or the LabVIEW software can be used to start the camera. The program can be used to save individual images as well as average a preselected number of images. This is used to obtain high signal-to-noise from many dissociation events.

2.3.1.5 Image Reconstruction

The two-dimensional images the ions form on the detector are a projection of the three dimensional velocity distributions. With regard to this work, the raw images are used to identify the key reaction dynamics. While in molecular beam experiments, it is generally

possible to convert the 2D images to a 3D velocity distribution. Several techniques have been developed to recover this information.

Forward convolution methods are used when the probed velocity distributions are not cylindrically symmetric. This is commonly the case during bimolecular collision experiments, where the interaction time of the molecules is much longer than the ionization laser pulse.[29] In these methods the image is simulated based on an initial guess at the differential cross-section. The cross-section is then altered until a good agreement is found. Several groups have developed source code using these methods utilizing Monte Carlo techniques, one such code is "Imsim" by McBane.[30, 31] Recently, Dick has reported a method involving the determination of the velocity distribution through an iterative process, known as a maximum entropy reconstruction.[32]

When the original velocity distribution can be probed with cylindrical symmetry intact, inversion methods such as, inverse Abel[33] and Hankel[29, 34] transforms may be employed. By converting the image into polar coordinates it is possible to apply an inverse Abel transform and to obtain the 3D velocity distribution. The Hankel transform instead applies a Fourier transform to the image distribution, then converts to polar coordinates which yields a zero-order Hankel transform of the 3D image. This can then be used to recover the 3D velocity distribution from the 2D image.[34]

Back-projection methods such as the onion peeling technique [35-37] use an alternative approach, relying on the fragments projection onto the detector plane. The initial velocity components of the fragments can be expressed in the form of the image angular distribution and ρ. Here, ρ is the ratio of the kinetic energy of the fragment due to the acceleration by the electric field and the initial fragment kinetic energy. Unfortunately, as there are in

general several values for ρ in a single image, one must address the impact of each value of ρ on the image separately. The most energetic fragment is treated first, then its impact on the image is removed, and iteratively this is done for all layers of the image. This then yields the original three dimensional velocity distribution.

Finally, a technique known as BASEX[38] and its variant pBASEX[39] have become common over recent years. This method represents the image as an expansion in a basis set of the overall image. By choosing a suitable basis set, the expansion coefficients used in the procedure can then yield the 3-D velocity distribution. The pBASEX algorithm has adapted this to the polar symmetry of the photoionization process. Poisson has developed a LabVIEW-integrated program free of charge.[40] Recent years have also seen the development of hybrid techniques combining basis set representation and onion peeling techniques.[41]

2.4 Measuring the ion signal

To measure the ion signal, along with the signal from two photodiodes which measure the power of the dye laser and the Nd-YAG/OPO lasers, a multifunctional LabVIEW program built by myself and Mr. Jeff Crouse is used. Additionally, the same code is used to control the dye laser, and controls the motion the grating and the crystal. This makes it possible to scan the laser and record the REMPI signal while accounting for laser power fluctuations using a single program. A different LabVIEW code is used to record and change the time delay between the two lasers and is discussed in Section 2.6.

2.5 Resonance Enhanced Multiphoton Ionization (REMPI)

This section follows the description of REMPI given by Telle.[16] The ionization process in REMPI is a multiphoton (as low as 2-photon) technique, whereby the first photon(s) resonantly excites the molecule to an excited state, and the absorption of a second set of photons leads to ionization of the molecule. The ability to state-selectively access the excited state is what leads to the advantage of REMPI over single-photon ionization. As the resonant absorption of the first photon(s) forming the bound excited state is governed by spectroscopic selection rules and ground state population, a distinct spectrum with identifiable vibrational and rotational levels will be observed when monitoring either the electron current or ion current. When describing a given REMPI process, it is common to use the notation of (m+n) for single colour REMPI processes and (m+n') for two-colour processes. Here, m is the number of photons at the laser energy used to pump the fragment to the bound state, and n is the number of photons used to ionize the resonant state. Figure 2.10 describes the different REMPI processes.

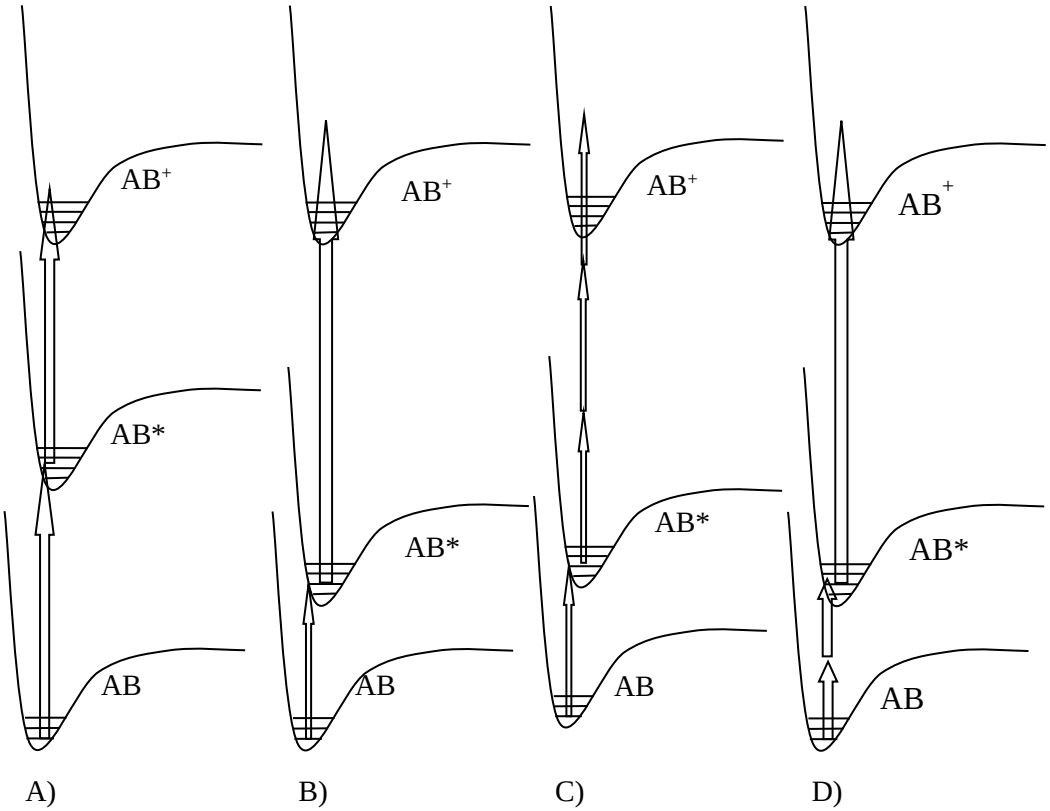

Figure 2.10: Description of four different REMPI process for a hypothetical diatomic molecule AB; A) (1+1), B) (1+1'), C) (1+3), and D) (2+1') REMPI

By scanning the frequency of the laser used for excitation to the intermediate state over the rotational transitions and measuring the restoring current, the relative populations of the rotational states of the fragments can be obtained. The spectral resolution of the REMPI spectrum is governed only by the excitation to the bound, intermediate state, and high-resolution lasers are preferred. The ionization step is non-resonant and may be conducted using a laser with a broader spectral linewidth.

It is not entirely obvious whether the ionization process itself can affect the measurement of the velocities of the photofragments. In fact, several considerations have to be made to obtain accurate VMI following a pump-probe experiment. The first is that as the fragment becomes ionized an electron must be removed. As the electron has mass, its recoil from

the photo-ion will cause a change in the velocity of this photo-ion. That being said, it is easy to see that in almost all cases momentum conservation ensures that the electron takes almost all excess kinetic energy and the ionized photofragment obtains very little additional kinetic energy. It is important to note that this may not always be true. If the photo-ion to electron mass ratio is not very large (as in the ionization of H-atoms for example) and/or the ionization threshold is exceeded by a large amount a measurable amount of kinetic energy is transferred to the photofragment products. The ionization recoil effect was first described by Loock et al. [17] in the photolysis of HI and subsequent ionization of the H-atoms at 277 nm.

Additionally, in the resonant excitation of fast-moving photofragments, a Doppler effect is observable. After photolysis some of the fragments recoil along the laser axis with a velocity that may amount to 5000 m/s.[3] Resonant spectroscopic transitions are then shifted according to the Doppler equation (see Equation 1.31). If the laser bandwidth is less than the Doppler shift, the laser wavelength has to be tuned over the entire width of the Doppler broadened line. In fact, Doppler broadening can be used as a diagnostic tool to estimate the fragment recoil velocities.[42]

Space charge effects may also impart excess energy during the ionization step. One can reduce the blurring effect of space charge by reducing the density of the generated photo-ions, for example by diluting the molecules in the molecular beam or by reducing the intensity of the ionization beam. In condensed phase experiments space charge effects are less likely to occur as the concentration of the photogenerated fragments is quite low.

Coupling REMPI with velocity map imaging allows us to measure the relative state

populations of each fragment in addition to its velocity distribution. In our study (1+1) REMPI will be used for NO detection.

2.6 Time Delay Experiments

Time delay experiments are highly suitable for condensed phase reactions. In the gas phase the time delay between the two laser pulses must be very short. The necessary equipment, ultrafast lasers and special timing equipment, becomes prohibitively expensive for our setup. In the condensed phase however, the limiting factor is the distance between the dissociation region and ionization region. As long as one can determine those parameters, the time delay can be converted to translational energy of the fragment. A customized LabVIEW program is used to collect the translational energy distribution of the NO photofragments. This is done by controlling the time delay between dissociation and ionization. As the displacement between the two laser beams is held constant at a few millimeters, by altering the time delay, one can probe the ions that leave the ice with a large amount of kinetic energy and those that are slower. This is shown schematically in Figure 2.11. With a short time delay, only those ions that have a large enough velocity to reach the ionization region in time can be ionized. Additionally, as the molecules are selectively ionized, the translational energy distributions between different rotational states of the ions are apparent.

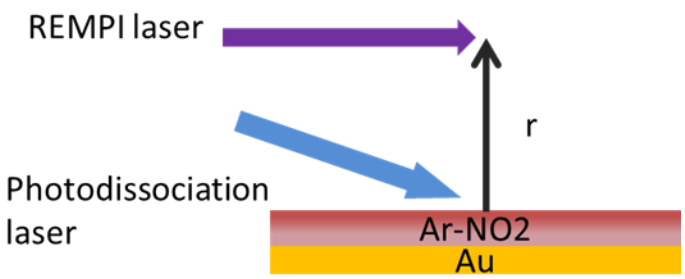

Figure 2.11: Arrival Time Setup: By varying the time delay between the photodissociation laser and the REMPI laser we are able to probe molecules with different velocities.

2.7 Summary

With the velocity map imaging apparatus described in this thesis we are able to conduct condensed phase VMI, REMPI, and time-delay experiments together. With these three experiments combined, the information needed to get a complete description of the molecular dynamics governing these condensed phase reactions can be obtained:

1) Fragment rotational state populations, through analysis of the REMPI spectrum.
2) Translational energy distribution along with difference between rovibrational bands, from the time delay experiments.
3) Fragment velocity and angular distributions, from the velocity map images.

This apparatus could, in the future, open the door for more complex reactions. These could involve reactions with the matrix and the guest species, such as photochemical reactions of nitrates within and on water ice. It may also be possible to study the fragmentation properties of active matrices themselves such as MALDI matrices.

CHAPTER 2 REFERENCES

[1] D.C. Jiles, Introduction to Magnetism and Magnetic Materials, Second Edition, CRC Press, USA, 1998.

[2] J. Moore, C.C. Davies, M.A. Coplan, S.C. Greer, Building Scienfitic Apparatus, Fourth Edition, Cambridge University Press, (2009).

[3] D.H.Parker, A.T.J.B. Eppink, Velocity map imaging: applications in molecular dynamics and experimental aspects, in: B.J. Whitaker (Ed.), Imaging in Molecular Dynamics Technology and Applications, Cambridge University Press, Cambridge, 2003, pp. 20-64.

[4] B. Jochim, R. Averin, N. Gregerson, J. McKenna, S. De, D. Ray, M. Zohrabi, B. Bergues, K.D. Carnes, M.F. Kling, I. Ben-Itzhak, E. Wells, Velocity map imaging as a tool for gaining mechanistic insight from closed-loop control studies of molecular fragmentation, Physical Review A 83 (2011).

[5] M.E. Corrales, J. Gonzalez-Vazquez, G. Balerdi, I.R. Sola, R. de Nalda, L. Banares, Control of ultrafast molecular photodissociation by laser-field-induced potentials, Nature chemistry 6 (2014) 785-790.

[6] M. Ahmed, D.S. Peterka, A.S. Bracker, O.S. Vasyutinskii, A.G. Suits, Coherence in polyatomic photodissociation: Aligned O(^{3}P) from photodissociation of NO_2 at 212.8 nm, J. Chem. Phys. 110 (1999) 4115.

[7] S. Manzhos, C. Romanescu, H.P. Loock, J.G. Underwood, Two-photon state selection and angular momentum polarization probed by velocity map imaging: application to H

atom photofragment angular distributions from the photodissociation of two-photon state selected HCl and HBr, J Chem Phys 121 (2004) 11802-11809.

[8] I. Wilkinson, M.P. de Miranda, B.J. Whitaker, Photodissociation of NO_2 in the (2) $^2B_2$ state: the O($^1D_2$) dissociation channel, J Chem Phys 131 (2009) 054308.

[9] S. Das, Narrow linewidth pulsed optical parametric oscillator, Pramana, J. Phys 75 (2010) 827-835.

[10] P. Schlup, G.W. Baxter, I.T. McKinnie, Single-mode near- and mid-infrared periodically poled lithium niobate optical parametric oscillator, Optics Communications 176 (2000) 267-271.

[11] K.L. Vodopyanov, J.P. Maffetone, I. Zwieback, W. Ruderman, AgGaS2 optical parametric oscillator continuously tunable from 3.9 to 11.3 μm, Applied Physics Letters 75 (1999) 1204-1206.

[12] B. Scherrer, I. Ribet, A. Godard, E. Rosencher, M. Lefebvre, Dual-cavity doubly resonant optical parametric oscillators: demonstration of pulsed single-mode operation, J. Opt. Soc. Am. B 17 (2000) 1716-1729.

[13] C. Drag, A. Desormeaux, M. Lefebvre, E. Rosencher, Entangled-cavity optical parametric oscillator for mid-infrared pulsed single-longitudinal-mode operation, Opt. Lett. 27 (2002) 1238-1240.

[14] Continuum, Horizon OPO Datasheet, in: C. lasers (Ed.)CA, USA, 2014.

[15] Handbook Of Laser Technology and Applications Institute of Physics Publishing, Bristol and Philadelphia, 2004.

[16] A.G.U. Helmut, H. Telle, Rovert J. Donovan, Laser Chemistry Spectroscopy, Dynamics, and Applications, Wiley2007.

[17] D.H. Parker, R.F. Delmdahl, B. Bakker, H.P. Loock, Ion recoil following (2+1) REMPI of nascent atoms - The effect on nascent velocity distributions in velocity map imaging, J.Chin.Chem.Soc. 48 (2001) 327-332.

[18] R. M. Garnica, M.F. Appel, L. Eagan, J R. McKeachie, and T. Benter, A REMPI Method for the Ultrasensitive Detection of NO and NO_2 Using Atmospheric Pressure Laser Ionization Mass Spectrometry, Anal. Chem. 72 (2000).

[19] R.C.Sausa, R.L. Pastel, (2+2) Resonance-Enhanced Multiphotn Ionization (REMPI) and Photoacoustic (PA) Spectroscopic Detection of Nitric Oxide and Nitrogen Dioxide Near 454 nm, Army Research Laboratory ARL-TR-1418 (1997).

[20] T. Shibata, T. Suzuki, Photofragment ion imaging with femtosecond laser pulses, Chemical Physics Letters 262 (1996) 115-119.

[21] J.K. Song, M. Tsubouchi, T. Suzuki, Femtosecond photoelectron imaging on pyrazine: Spectroscopy of 3s and 3p Rydberg states, J. Chem. Phys. 115 (2001) 8810-8818.

[22] T. Suzuki, L. Wang, H. Kohguchi, Femtosecond time-resolved photoelectron imaging on ultrafast electronic dephasing in an isolated molecule, J. Chem. Phys. 111 (1999) 4859-4861.

[23] J.R.L. P.P. Sorokin, E. C. Hammond, V. L. Moruzzi, Laser-pumped Stimulated Emission from Organic Dyes: Experimental Studies and Analytical Comparisons, IBM J. Res. Develop. 11 (1967) 130.

[24] B.B.S. F.P Schäfer, C.V. Shank, E.P. Ippen, K. H. Drexhage, T.W. Hänsch, Topics in Applied Physics: Dye Lasers Second Revised Edition, Springer-Verlag1977.

[25] U. Brackman, Lambdachrome Laser Dyes, Lamda Physik GmbH, Germany, 1997.

[26] L.P. GmbH, Dye Laser SCANmate Instruction Manual, Lambda Physik Inc., Goettingen, Germany, 1997.

[27] D. Boldovsky, PHOTODISSOCIATION DYNAMICS OF BROMINE CHLORIDE PROBED BY VELOCITY MAP IMAGING., Department Of Chemistry, Queen's University, Kingston, On, 2006.

[28] E. Inc., P-45 Datasheet, in: E. Inc. (Ed.)Virginia USA, 2015.

[29] A.T.J.B. Eppink, Wu, S.-M., Whitaker, B.J., Resonstruction Methods, in: B.J. Whitaker (Ed.), Imaging in Molecular Dynamics- Technology and Applications, Cambridge University Press, New York, USA, 2003.

[30] G.C. McBane, Simulation and Analysis of Image Data from Crossed Beam Experiments, McBane, G. C., Ohio.

[31] C.-H. Yang, Sarma, G., ter Meulen, J. J., Parker, D. H., McBane, G. C., Wiesenfeld, L., Faure, A., Scribano, Y., Feautrier, N. , Mapping Water Collisions for Interstellar Space Conditions, Journal of Chemical Physics 133 (2010) 131103.

[32] B. Dick, Inverting ion images without Abel inversion: maximum entropy reconstruction of velocity maps, Physical chemistry chemical physics : PCCP 16 (2014) 570-580.

[33] A.J. Heck, D.W. Chandler, Imaging techniques for the study of chemical reaction dynamics, Annu Rev Phys Chem 46 (1995) 335-372.

[34] L.M. Smith, Keefer, D.R., Sudharsanan, S. I, Abel Inversion using transform techniques, Journal of Quantitative Spectroscopy and Radiative Transfer 39 (1988).

[35] C. Bordas, F. Paulig, H. Helm, D.L. Huestis, Photoelectron imaging spectrometry: Principle and inversion method, Review of Scientific Instruments 67 (1996) 2257.

[36] J. Winterhalter, D. Maier, J. Honerkamp, V. Schyja, H. Helm, Imaging of charged atomic reaction products: Inversion by a two-dimensional regularization method, J. Chem. Phys. 110 (1999) 11187.

[37] S. Manzhos, H.-P. Loock, Photofragment image analysis using the Onion-Peeling Algorithm, Computer Physics Communications 154 (2003) 76-87.

[38] V. Dribinski, A. Ossadtchi, V.A. Mandelshtam, H. Reisler, Reconstruction of Abel-transformable images: The Gaussian basis-set expansion Abel transform method, Review of Scientific Instruments 73 (2002) 2634.

[39] G.A. Garcia, L. Nahon, I. Powis, Two-dimensional charged particle image inversion using a polar basis function expansion, Review of Scientific Instruments 75 (2004) 4989.

[40] L.C.-C. Poisson, LV_pBASEX, CEA-CNRS, Saclay, France, 2015.

[41] G.M. Roberts, J.L. Nixon, J. Lecointre, E. Wrede, J.R. Verlet, Toward real-time charged-particle image reconstruction using polar onion-peeling, The Review of scientific instruments 80 (2009) 053104.

[42] J.L. Kinsey, Fourier transform Doppler spectroscopy: A new means of obtaining velocity-angle distributions in scattering experiments, J. Chem. Phys. 66 (1977) 2560-2565.

Chapter 3

Condensed Phase VMI Apparatus

3.1Considerations for a Condensed Phase Experiment.

The key difference between a conventional VMI setup and the condensed-phase VMI (CP-VMI) described here is its ability to study photochemical reactions in the condensed phase with the same state-selective detection, angular resolution and kinetic energy resolution as is afforded by regular VMI. CP-VMI requires several alterations to the typical velocity map imaging apparatus. Naturally, the first alteration is the need for a surface on which the sample can be condensed. This surface must not interfere with the electric field within the region, or, at a minimum, the distortion caused by the electric field must be accounted for in some way. It must also be possible to cool the surface to a temperature at which the sample condenses on the surface - roughly 30 K for an argon matrix. The other difference between a typical VMI experiment and CP-VMI is the timing of the gas pulse. In a typical experiment the molecular beam valve is triggered such that the laser intersects the gas molecules. In the condensed phase setup this is to be avoided as only the species from the condensed material are to be probed.

3.1.1 Cryostat system

To cool the sample surface, a closed cycle helium cryostat (Sumitomo, DE204) is used. The cryostat cools a 7.6 cm long, 0.5 cm diameter sapphire “cold finger” to between 20 and 8K. The cold finger is placed into the acceleration region of the time-of-flight mass spectrometer. Sapphire was chosen as it is thermally conductive, but electronically

insulating and may thereby limit distortion of the electric field. The temperature of the finger is controlled using a controller (Cryo-Con 32), which can adjust the temperature of the substrate between 8 K and 300 K. This is done by monitoring the temperature using a silicon diode and then regulating the temperature with a small heater.

3.1.2 Timing control

The timing between the beam valve and the Nd:YAG laser, or OPO beam if being used, is done using a delay generator (DG535, Scientific Instruments). All of the pulses operate at a 10 Hz cycle. The flash lamp of the Nd:YAG fires first, then the Q-switch of the Nd:YAG laser is internally timed with the flash lamp and is triggered after 140 μs. A pulse synchronized with the Q-switch then triggers a DG535 delay generator. This pulse acts as "time zero" reference for all subsequent pulses. The delay generator sends out three pulses. The first, timed with the initial trigger, initiates a second DG535 delay generator. The second pulse is used when in imaging mode and is used to gate the microchannel plates. This pulse is timed such that the microchannel plate (MCP) is only on when the ions reach the detector. This is achieved by sending a pulse to a high voltage switch (*DEI* Scientific) which switches the back MCP from 0 to -500 V while the front MCP is held constant at +1400 V. The third pulse is sent to the camera controlling its shutter and exposure time. It is chosen to cover the arrival time of the ions. In wavelength scanning mode, also known as REMPI mode, the MCP is held "on" for the entirety of the experiment.

The second delay generator triggers both the excimer laser (Lambda Physics, 200), which pumps the dye laser used for REMPI, and the molecular beam valve, MBV (Parker). For condensed phase studies the MBV is opened 1 ms after the excimer laser fires. This limits

the amount of background NO_2 gas present during the experiment as almost an entire duty cycle (100ms) elapses before the condensed sample is dissociated again. In gas phase studies the MBV is timed such that the laser pulse from the dye laser overlaps the gas pulse. The molecular beam valve is open for 200 µs in both experimental modes. A timing diagram for the condensed phase experiment is shown in Figure 3.1 below.

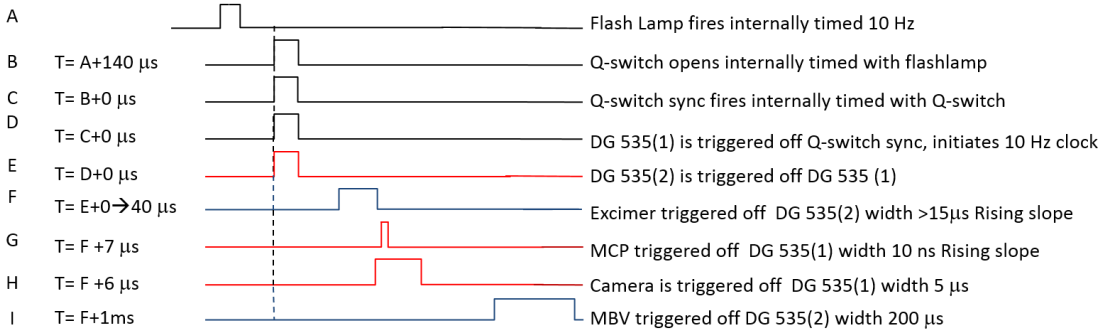

Figure 3.1: Trigger diagram from the different timing events during the experiment. The different colours indicate the source for the given pulse. Black signifies the sync output from the Q-switch of the Nd:YAG laser. The last of these three pulses starts the first delay generator labeled DG-535(1) in the figure and can be considered time zero of the experiment. The red lines signify pulses from the first delay generator and blue lines signify pulses starting from the second delay generator DG-535(2). All events are triggered on the rising edge.

3.1.3 Sample Preparation

The gas sample is made using an all stainless steel gas handling line. The line has several ports that can be made available to add bubblers, freeze-pump-thaw bulbs, or other contraptions that may be required for sample preparation.

In our experiments either NO (154 ppm in N_2) or NO_2 (Praxair, 99.5%) mixed with argon (Praxair, 5.0) was used without further purification. The sample concentrations are measured using a pressure gauge and used in relation with Raoult's law. Nitric oxide was mixed with argon through diffusion within the stainless steel containers up to a backing pressure between one and two bar, and left for two to twenty four hours to ensure proper mixing.

3.1.3.1 NO_2 mixing properties.

It should be noted that NO_2 mixing is not quite as simple as one would expect from Raoult's law. NO_2 differs from the ideal gas law quite strongly in moderate concentrations due to dimerization into N_2O_4. Care must be taken to ensure that concentrations of NO_2 are low enough that dimerization is negligible. Tevault and Andrew [1] have shown that when an NO_2 : Ar mixture is deposited at concentrations below 1:100 no dimerization occurred at 16 K. However, warming of the matrix above 40 K resulted in small amounts of dimerization. In order to avoid dimerization we kept the concentration at 1:150, as well as maintained a matrix temperature below 40 K. For many of our early studies, a round bottom flask connected to the gas handling line was used to inspect the gas. When dimerization occurs, the sample changes from a deep red-brown colour to a colourless, clear gas. Thus we were able to easily assess the extent of dimerization.

3.2 Apparatus design

The cold finger has first been installed perpendicular to the time of flight axis and later along the time of flight axis. Additionally, two different ion optic designs were developed in order to attempt to study the condensed phase photodynamics. The following section describes the different designs and the simulations of their ion trajectories.

3.2.1 Perpendicular Apparatus Setup

In the original ion optic design shown in Figure 3.2, the sapphire rod was placed perpendicular to the time-of-flight axis, between the repeller and extractor electrodes. The dissociation beam then struck the surface at an angle of 35^{o}. The resulting NO particles were ionized 2-5 mm above the surface. Using this design, REMPI experiments were conducted. Several images of the ions were collected, however, due to distortions of the electric field the velocity map images were highly distorted.

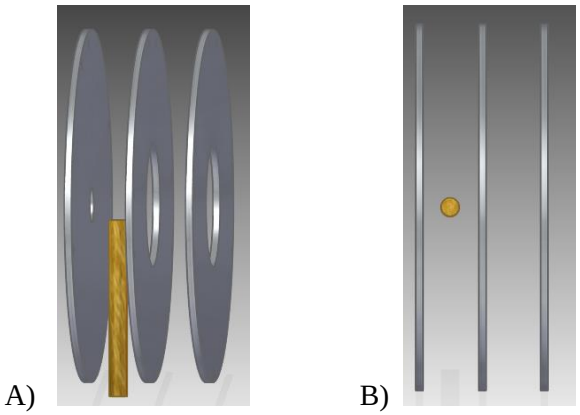

Figure 3.2:Perpendicular cold finger orientation: the cold finger was placed between the extractor and repeller electrodes with the surface 2 mm below the center of the plates. A) Side view. B) Top view from above the apparatus.

3.2.1.1 Image distortion

Nitric oxide at 150 ppm in nitrogen gas was used as a test molecule for testing the mapping capability of the system. In initial experiments, the cold finger was lowered completely out of the acceleration region. In these experiments the timing of the molecular beam valve (above the cold finger, but not shown in Fig 3.2) and the ionization beam are set such the molecular beam and the laser pulse intersect in the centre of the first time-of-flight acceleration region. The resulting ions were then accelerated using potentials set for VMI conditions.

The VMI condition was said to have been achieved when the image was a thin line only a few pixels across, shown in Figure 3.3A. The length of the image, *L* can be used to calculate the spread in velocities of the molecular beam valve.

$$\begin{aligned} &L = 110\,pixels / 1.375 = 80\,pixels \\ &t = 8.03\mu s \\ &1\ metre = 15400\,pixels \\ &L = 0.00519m \\ &v_{spread} = 0.00519m / 8.03x10^{-6} s = 650m / s \end{aligned} \tag{3.1}$$

Here, *L* is the length of the image, the factor 1/1.375 is the magnification factor discussed in section 3.2.3.2 and *t*, is the length of time between ionization and detection. This gives a spread in velocities of approximately 650 m/s for the molecular beam. These gas phase experiments proved that our design was capable of VMI of molecular beams.

The gas phase experiments were then repeated, this time with the cold finger in place. The resulting image is shown in Figure 3.3B. It is clear to see that a large distorting effect is caused by the cold finger.

It is then no surprise that condensed phase experiments conducted using NO_2 in argon also showed distortions. In Figure 3.2C the image shows large deviation from velocity mapping. The image appears to show that the particles have a negative (y) component. If this were true, however, the fragments would have travelled into the matrix and could not have been ionized.

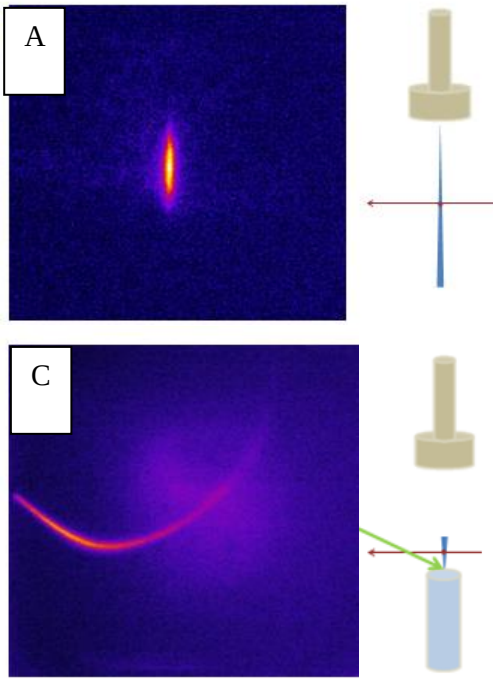

Figure 3.3:NO^+ ion images following 1+1 REMPI of NO at the bandhead of the Q transition at 226 nm. A) Gas phase NO 150 ppm in N_2, with the cold finger lowered completely out of the ionization region. The length of the intense part of the image can be used to determine the spread in the velocity of the molecules from the molecular beam. The thin line demonstrates velocity mapping for the molecular beam. B) Gas phase NO in N_2 with the cold finger at the location used during condensed phase studies. The resulting looped image (as opposed to the thin line in the top right image) illustrates the distortion caused by the cold finger. C) Resulting image of NO ions following dissociation of NO_2 from an NO_2:Ar 1:150 matrix at 10K. Distortion of the electric field due to the presence of the finger is evident from the curvature of the image.

3.2.2 Wing Electrode Design

In order to decrease the effect of the electric field distortion, a "wing electrode" design was built. Two additional electrodes were placed around the cold finger. They were controlled by a separate power supply and supplied with a voltage in an attempt to correct for the field distortion caused by the cold finger. While gas phase experiments with this design showed promise, no signal could be found when NO was ionized following photolysis of NO_2 in an argon-NO_2 matrix.

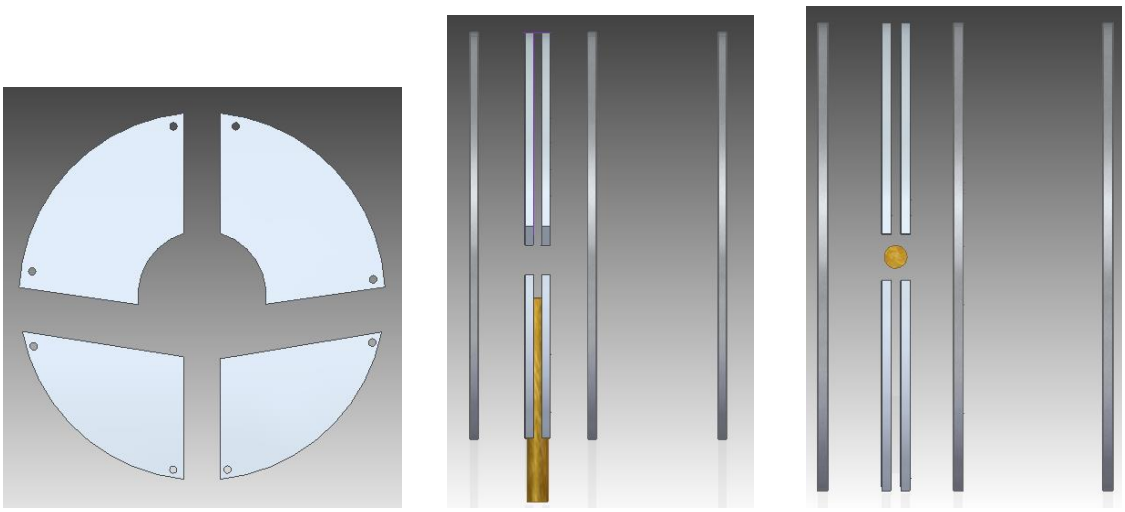

Figure 3.4: Wing electrode design. The three extractor, repeller, and ground electrodes remain the same as in the design above, however two additional electrodes were placed between the repeller and extractor electrodes. These additional electrodes surround the cold finger with potentials used to mimic the electric field that should be present without the cold finger in place. Unfortunatly, it proved too difficult to sucessfully dissociate and ionize the matrix material without tripping the electrodes.

3.2.3 On-Axis Apparatus Setup

In the current ion optic design, the cold finger is attached on axis with the time of flight spectrometer, with the surface of the cold finger at the center of the repeller plate. While the cold finger may still accumulate some electric charge, this would lead to a cylindrically symmetric distortion and then have a less pronounced effect on the velocity map imaging conditions.

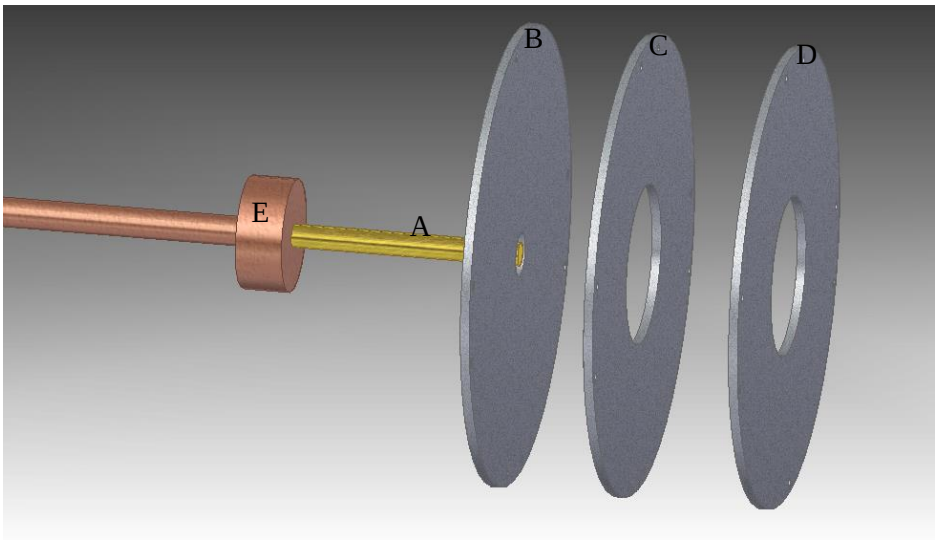

Figure 3.5: On-axis orientation of VMI ion optics. The cold finger, A, is mounted on a copper extending rod, E, and centered at the middle of the repeller electrode, B. The dissociation laser enters at a 35° angle between the repeller, B, and extractor, C, electrodes. Fragments are ionized between the repeller and extractor and are then accelerated down the length of the time-of-flight spectrometer through the ground plate, D.

3.2.3.1 Testing of On-Axis Design

The on-axis orientation of the cold finger results in an undistorted VMI image in the ionization of nitric oxide from a molecular beam (Figure 3.6). By comparing these images with Figure 3.2 (B), it can be seen that the “looping” effect has been eliminated and that a thin image has returned. The difference in intensity is due to the fact that in the current

orientation the appropriate position for dissociation of the molecular fragments from the ice surface is not directly in line with the molecular beam and the molecular flux and velocity of the NO molecules is reduced.

Figure 3.6: NO^+ ion images following (1)+1+1 REMPI at 226 nm with on-axis configuration. **Left**, gas phase NO in N_2 concentration 1:1000, beam valve open for 190 μs and the ionization region 4 mm away from the sapphire rod. The low intensity is due to the fact that the ionization region is now outside the main part of the molecular beam. **Right**, molecular beam open for 350 μs. The increased molecular flux widens the image due to ion-ion repulsion.

The images along with the SIMION calculations (Section 3.2.3.2) illustrate how that velocity map imaging in the presence of the sapphire rod is possible, if the correct potentials are applied to the ion optics.

3.2.3.2 Ion Trajectory Calculations

SIMION 8.1 (Scientific Instrument Services, Inc.) is a virtual ion optics bench, used to model experimental designs by modeling the flight of charged particles within the potential array created by the user. The user may design their ion optic bench by creating a *.GEM file which contains the electrode design. The electrode geometries and electrostatic potentials are stored in an array and are then refined by solving the Laplace equation by finite difference methods. The user defines starting parameters for charged particles, such

as mass, initial position, charge, and velocity. The software then calculates the trajectories of the particles and displays them in a process known as “flying”, or “fly’n”.

Ion trajectory calculations were performed using the geometry of our system utilizing the capability of SIMION 8.1 to simulate dielectric potentials. This is done by first creating one *.GEM file for the field inside the dielectic materials, which simulates the effect of the cold finger by assigning the volume occupied by the sapphire rod with a dielectric constant of ε=11.1, i.e. that of sapphire’s C axis, and by leaving the rest of the system at vacuum (ε= 1). The electrode geometry is held in a separate *.GEM file that consists of the three 11.4 cm diameter electrodes (repeller, extractor, and ground), the length of the VMI chamber 75 cm, and, in some simulations, the MCP detector. This electrode design is then refined with respect to each point in the dielectric field defined in the other *.GEM file. This greatly increases the amount of time for the refining process from a few seconds up to 20 minutes on a PC with 16G of available RAM.

The VMI simulation by Eppink and Parker [2] was used as a starting point as the geometries of our systems are very similar with the exception of the presence of our cold finger. In the simulation, 24 ion trajectories are modeled, originating at 3 different positions (0.5 mm apart) along the y axis, simulating a focal region of the ionization laser. At each of these three locations eight ions are placed with 1 eV kinetic energy and a mass of 15 amu. The mass was selected to be consistent with work by Eppink and Parker[3]. The velocities of the eight ions are given different directions along the x-y-plane in increments of 45 degrees in elevation. In Figure 3.7 the simulation seen in their publication is recreated, and we see that the ions with the same direction all map to the same location regardless of the initial position. When the effect of the cold finger is simulated by including the dielectric field in

the region of the cold finger we can see that the system no longer focuses the velocities (Figure 3.8 top). In order to regain the VMI "space focusing" effect we must alter the V_R/V_E ratio. In this case, the potential on the extractor was changed from V_E = 750 to 800V. In Figure 3.9, the voltages on the repeller are increased to V_R = 3000 V and 2330 V respectively, which achieves VMI conditions at the position of our MCP detector.

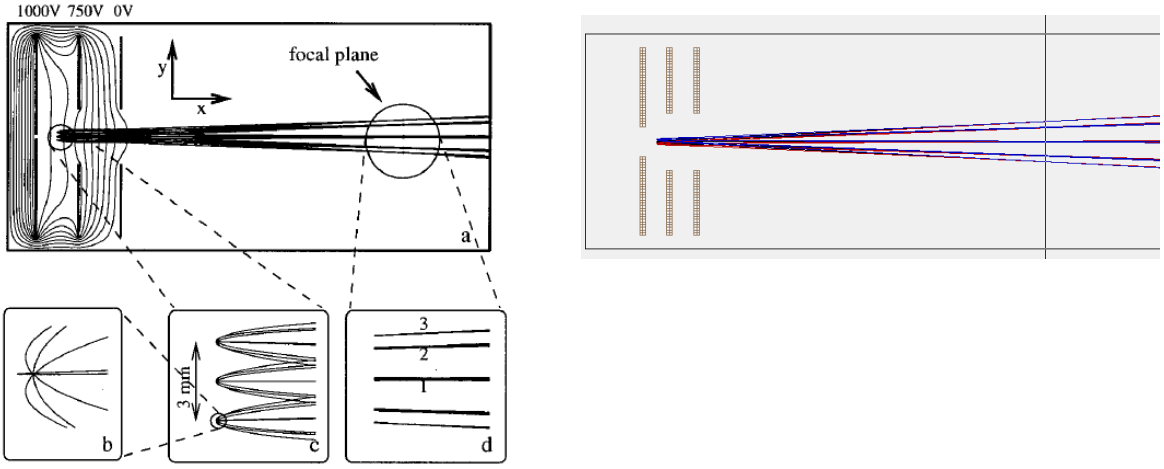

Figure 3.7: Left, SIMION results reported by Eppink and Parker 1997[2]. The ions are mapped to the position along the y-axis dependent on their velocities at the focal plane highlighted in the circular region (d) illustrating the VMI effect. In the right Figure, the results are reproduced using the electrode design used in the Loock group. The ions are all given the same starting positions in space relative to the electrodes and the ion velocities are all the same as in the work of Eppink and Parker. The vertical line in the image shows the focal plane, where all ions with the same velocities map to the same point.

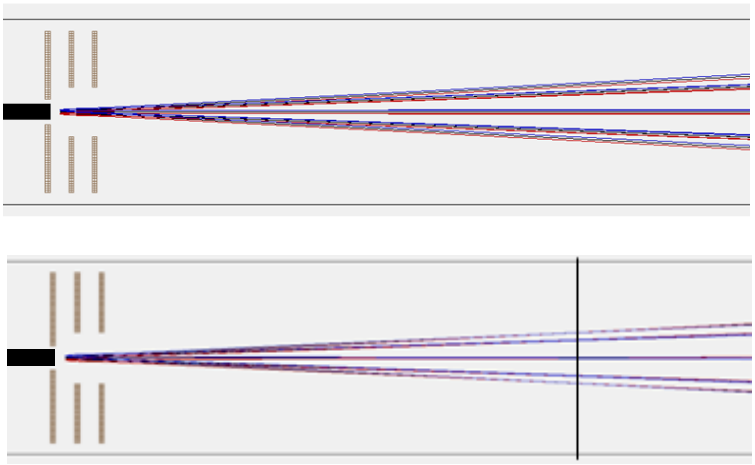

Figure 3.8: *Top*: Using the same electrode design and potentials as seen in Figure 3.5, with the dielectric effect of the sapphire rod included. It is evident that the ions do not exhibit the same velocity focusing as experienced without the electric field. *Bottom*: The focusing effect can be recovered by altering the potential of the extractor plate to 800 V.

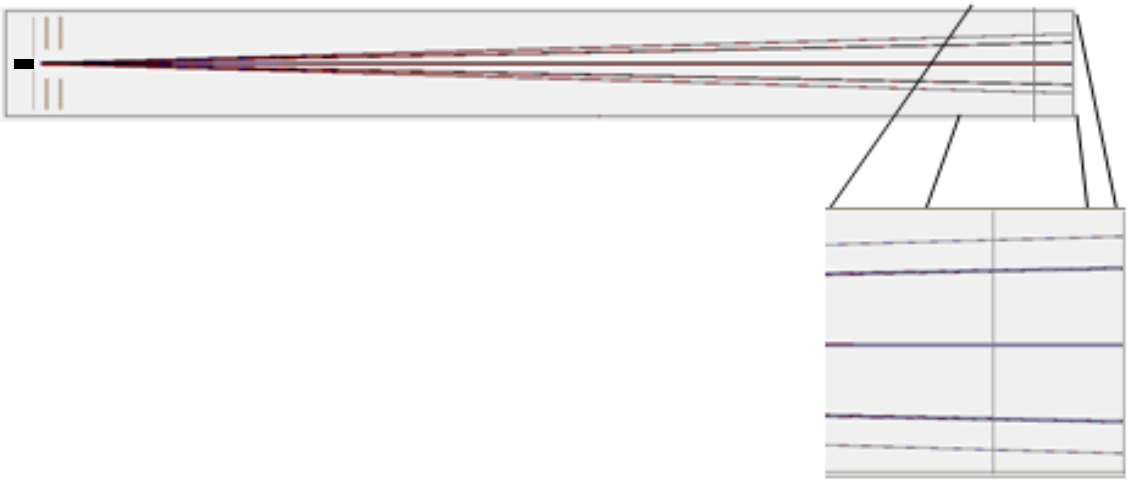

Figure 3.9: Results from ion trajectory calculation. Ions are velocity-focused at the position of our detector (75 cm away from ground electrode). Voltages used in the simulation were 3000 and 2330 V for the repeller and extractor plates, respectively. Experimental values vary from these settings, as the position of the cold finger with respect to the VMI optics change slightly. In the bottom Figure we see that velocity mapping is achieved due to the low spread in width of the ion bunches >0.5mm

The effect of the cold finger on the magnification factor, *N*, (see Chapter 1) can be seen from comparison with that calculated from Piyumie Wickramasinghe's M.Sc. thesis in our group [4]. She calculated the magnification factor for our electrodes in the absence of the cold finger for several V_R/V_E ratios. The magnification factor is the ratio of the radius

image seen (or calculated in simulation), *R*, to that expected from a uniform acceleration field, *R'*.

$$R' = vt \tag{3.2}$$

Here, *v* is the expansion velocity of the fragment, and *t* is the ion time of flight. By simulating two ions starting at the ionization region, both with the same translation kinetic energy and mass (1 eV and 15 amu, to be consistent with previous studies), but one traveling along the time of flight axis (0^o elevation) and one perpendicular (90^o elevation), it is possible to find the value of *R*. The ion time of flight is also reported from the ion trajectory simulation and, since the initial kinetic energy and mass are known, it is simple to calculate *R'*. The table below reports the values for the magnification factor with the dielectric field for several different values of extractor and repeller voltages.

Figure 3.10: Trajectories for two ions of mass 15 AMU and 1 eV of kinetic energy, one directly along the TOF axis, the other 90^o from it. The difference between the two positions where the ions strike the MCP give the value of R for the given potentials applied to the electrodes.

Table 3.1: Ion trajectory simulations of radius of the image and magnification factor based on different voltages applied to the electrodes, using ions with 15 amu mass and 1 eV of kinetic energy

V_R	V_E	TOF	R'	R	N
3000	2330	7.62848	27.36	37.65	1.375
2500	1942	8.20544	29.43	40.40	1.372
2000	1553	8.94214	32.08	43.90	1.369
1500	1165	9.93227	35.63	49.03	1.376
1000	777	11.381	40.82	55.89	1.369

The magnification factor is considerably larger compared to that determined by Wickramasinghe [4], who found an average value of N=1.275 caused by the inclusion of the dielectric field. This magnification factor is used when converting the size of the images to the distances that the ions actually traveled and as such their velocities.

CHAPTER 3 REFERENCES

[1] D.E. Tevault, L. Andrews, Laser Raman Matrix-Isolation Studies of Nitrogen Dioxide Resonance Raman-Spectrum of NO_2 and Raman-Spectrum of N_2O_4, Spectrochimica Acta Part A-Molecular and Biomolecular Spectroscopy A 30 (1974) 969-975.

[2] A.T.J.B. Eppink, D.H. Parker, Velocity map imaging of ions and electrons using electrostatic lenses: Application in photoelectron and photofragment ion imaging of molecular oxygen, Review of Scientific Instruments 68 (1997) 3477.

[3] A.T.J.B. Eppink, D.H. Parker, Velocity map imaging of ions and electrons using electrostatic lenses: Application in photoelectron and photofragment ion imaging of molecular oxygen, Review of Scientific Instruments 68 (1997) 3477-3484.

[4] P. Wickramasinghe, Veloctiy Map Imaging Apparatus for Studies on the Photochemistry of Water Ice, Department of Chemistry, Queen's University, Kingston, On, 2011.

Chapter 4

Literature Review: NO_2 Photodynamics in the First Absorption Band in the Gas and Condensed Phase

4.1 Photolysis Experiments of NO_2

Many photodissociation experiments have been conducted on gas-phase or molecular-beam-cooled NO_2 throughout the past 40 years. In these experiments researchers investigated the photoproduct identities, absorption cross sections, relative or absolute photoproduct yields, and branching ratios between electronic, vibrational and rotational quantum states. As a consequence much is known about the spectroscopy, reaction dynamics, and, therefore, about the excited state potential surfaces. The following section is a short review of this area.

Of course, NO_2 is an open-shell molecule and so has complicated and intriguing spectroscopic characteristics. There are several low-lying electronic states which are strongly coupled and researchers have identified several avoided crossings.[1] Wilkinson and Whitaker have calculated potential energy surfaces. Their adiabatic [1] (Figure 4.3) and diabatic [2] PES (Figure 4.4) were based on calculations by Schinke.[3, 4]

Table 4.1 shows the electronic configurations of the ground state and several excited states. The $(1)^2B_1$ and $(1)^2B_2$ states govern the photochemistry of NO_2 at excitation wavelengths longer than about 200 nm.

Table 4.1: Electronic configuration for the ground state and several of the excited states that are relevant to our study. Reproduced from Whitaker.[1] Excitation energies from 398 nm to about 250 nm lead to population of the first excited $(1)^2B_2$ state, and excitation from 248-198 nm leads to excitation into the $(2)^2B_2$ state. Note that these are labeled using electronic symmetry labels and the (1) $^2A_1$ state is the ground state.

State/C_{2v}	Coefficient	$3a_1$	$2b_2$	$4a_1$	$5a_1$	$3b_2$	$1b_1$	$4b_2$	$1a_2$	$6a_1$	$2b_1$	$7a_1$	$5b_2$	$(1)^2A_1 \rightarrow$ n
$(1)^2A_1$	0.9210112	↑↓	↑↓	↑↓	↑↓	↑↓	↑↓	↑↓	↑↓	↑				
$(1)^2B_1$	0.9144082	↑↓	↑↓	↑↓	↑↓	↑↓	↑↓	↑↓	↑↓		↑			$2b_1(\uparrow) \leftarrow 6a_1(\uparrow)$
$(1)^2B_2$	0.8836805	↑↓	↑↓	↑↓	↑↓	↑↓	↑↓	↑	↑↓	↑↓				$6a_1(\downarrow) \leftarrow 4b_2(\downarrow)$
	−0.2316846	↑↓	↑↓	↑↓	↑↓	↑↓	↑↓	↑↓	↓	↑	↑			$2b_1(\uparrow) \leftarrow 1a_2(\uparrow)$
$(1)^2A_2$	0.9254254	↑↓	↑↓	↑↓	↑↓	↑↓	↑↓	↑↓	↑	↑↓				$6a_1(\downarrow) \leftarrow 1a_2(\downarrow)$
$(2)^2A_2$	0.7231020	↑↓	↑↓	↑↓	↑↓	↑↓	↑↓	↑	↑↓	↑	↓			$2b_1(\downarrow) \leftarrow 4b_2(\downarrow)$
	−0.5415803	↑↓	↑↓	↑↓	↑↓	↑↓	↑↓	↓	↑↓	↑	↑			$2b_1(\uparrow) \leftarrow 4b_2(\uparrow)$

At 355 nm excitation to the (1) $^2B_2$ state is predominantly excited as the (1) $^2A_2$ is dark and the transition to the (1) $^2B_1$ state is much weaker.[5] Figure 4.1 shows the NO_2 absorption cross from 200 to 800 nm. Figure 4.2a-c show the molecular orbitals for the ground state HOMO (singly occupied), as well as the relevant molecular orbitals involved in the transitions to the excited electronic states.

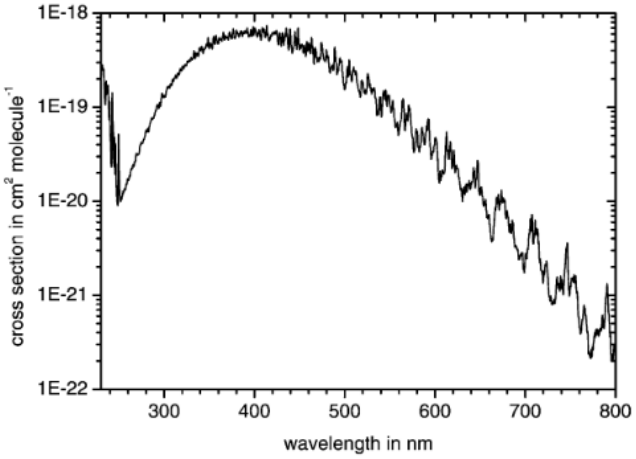

Figure 4.1: Absorption cross section of NO_2, it is easy to see that a dissociation wavelength of 355 nm is near the maximum of the absorption spectrum. Reproduced from Orphal.[6]

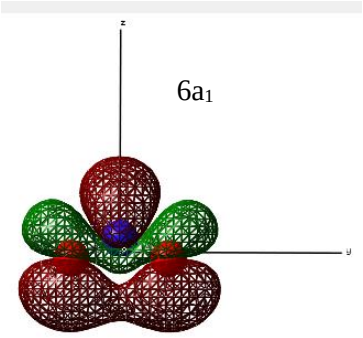

Figure 4.2a: The highest singly occupied molecular orbital (SOMO) in the ground state configuration, MO $6a_1$.

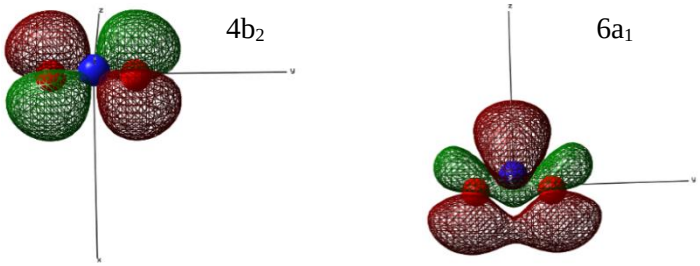

Figure 4.2b: Orbitals involved in the transition to the (1) $^2B_2$ state. Left; MO $4b_2(\downarrow)$ is the donating orbital. Right; MO $6a_1(\downarrow)$ is the accepting orbital.

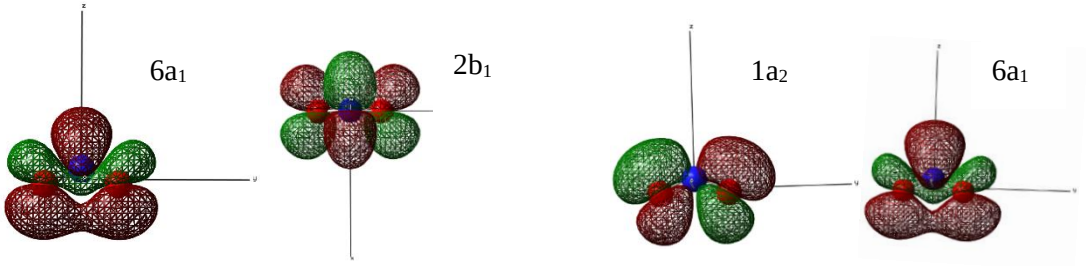

Figure 4.2c: The other two sets of orbitals involved in the other excitations, on the left are the MO's involved in the transition to the (1) $^2B_1$ state, involving MO's $6a_1 \uparrow$ (donating) and the $2b_1 \uparrow$ (accepting). On the right are the MO's involved in the transition to the (1) $^2A_2$ state, involving MO's $1a_2 \downarrow$ (donating) and the $6a_1 \downarrow$ (accepting).

The mutual alignment of the laser polarization, the transition dipole moment, μ, and the resulting fragment recoil vectors is an important aspect in molecular photodynamics. The alignment of the fragment recoil velocity vector with the transition dipole moment vector is characterized by the spatial anisotropy parameter β, as described in Section 1.4.2. The molecular orbital symmetries of the states involved are important in relation to the excitation of the molecule. NO_2 is a member of the C_2v point group in the Franck-Condon region, and the position of the transition dipole moment can be easily calculated using the respective direct product table. If the transition dipole moment is normal to the plane containing the NO_2 molecular frame, it is of B_1 symmetry. It is of B_2 symmetry when it lies in the plane of the molecule, i.e. along a line between the two oxygen atoms. The transition probability is given by,

$$\left|\left\langle MO_{final}\left|\vec{\mu}\right|MO_{initial}\right\rangle\right|^2 \tag{4.1}$$

and the symmetry of the transition is given by the direct product of the three symmetries through the use of a product table.

Table 4.2 C_{2v} Product Table

	A_1	**A_2**	**B_1**	**B_2**
A_1	A_1	A_2	B_1	B_2
A_2	A_2	A_1	B_2	B_1
B_1	B_1	B_2	A_1	A_2
B_2	B_2	B_1	A_2	A_1

By taking the direct product of the molecular orbital symmetries with the transition dipole moment we then obtained the symmetry of the transition.

$$MO_{final} \times \mu_{sym} \times MO_{initial} \tag{4.2}$$

Where all terms are the appropriate symmetry labels for each orbital and for the transition dipole moment. For an allowed transition, the direct product will yield a resultant symmetry of a_1. For the transitions listed above we have C_{2v} symmetries of $^2B_1$, $^2B_2$ and $^2A_2$ the symmetries for transitions perpendicular to the NO_2 molecule are then given by:

$$\begin{aligned} {}^2\mathrm{B}_1 &\rightarrow 2b_1 \times b_1 \times 6a_1 = a_1(allowed) \\ {}^2\mathrm{B}_2 &\rightarrow 6a_1 \times b_1 \times 4b_2 = a_2(not\ allowed) \\ {}^2\mathrm{A}_2 &\rightarrow 2b_1 \times b_1 \times 1a_2 = b_2(not\ allowed) \end{aligned} \tag{4.3}$$

And with the transition dipole moment in the plane of the molecule we have:

$$\begin{aligned} {}^2\mathrm{B}_1 &\rightarrow 2b_1 \times b_2 \times 6a_1 = a_2(not\ allowed) \\ {}^2\mathrm{B}_2 &\rightarrow 6a_1 \times b_2 \times 4b_2 = a_1(allowed) \\ {}^2\mathrm{A}_2 &\rightarrow 2b_1 \times b_2 \times 1a_2 = b_1(not\ allowed) \end{aligned} \tag{4.4}$$

The transition to the $^2B_2$ state is the most intense transition at 355 nm. The direct product suggests that the transition is allowed when the laser polarization is in the plane of the molecule. This gives a maximum β parameter of 2 for this transition, however, the transition dipole moment is not aligned with the dissociating N-O bond and, even if it was, the rotational [7] and vibrational[8] modification to the transition dipole moment can reduce the value of β considerably. Demyanenko[9] has shown that the NO_2 molecule bends to a smaller angle during dissociation which lowers the maximum β parameter to β

= 1.8, while Monti et al.[10] has shown that at certain rotational states this is lowered further down to 1.6.

In our dissociation experiments of NO_2 in the Ar-matrix the photolysis laser is horizontally polarized such that the molecules are preferentially dissociated along the time-of-flight axis. Many of molecules undergo several collisions with the matrix, which causes vector correlation information loss, but those molecules that are dissociated directly from the surface of the argon film may should retain this information.

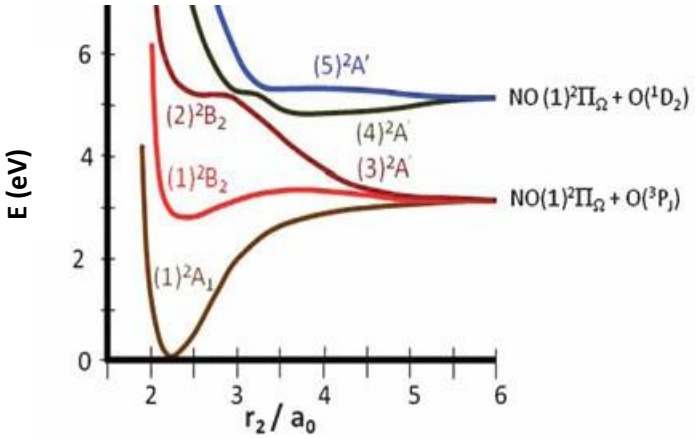

Figure 4.3: Potential energy curves for the first five adiabatic curves along the ON-O coordinate based on the work by Schinke[3].

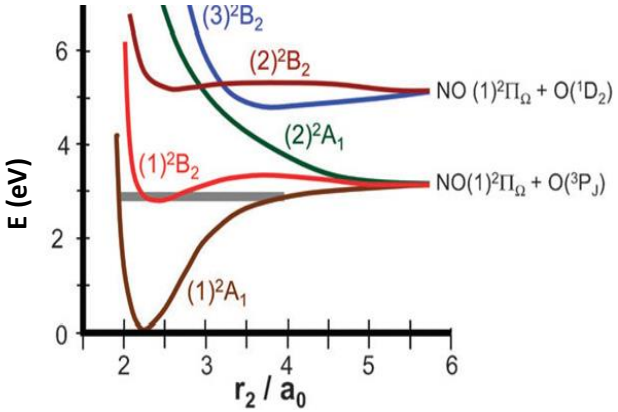

Figure 4.4: The diabatic potential energy curves for the NO_2 molecule corresponding to the adiabatic curves shown in Figure 4.3. Note that there is a change in symmetry labeling convention between some of the states in the two figures. The adiabatic curve (4) ^{2}A' corresponds to the diabatic $(2)^2A_1$ curve and $(5)^2$A' corresponds with $(3)^2B_2$.

NO_2 has a bent ground state configuration with a bond angle of 134°, caused by the interactions involving two of the higher energy molecular orbitals, $6a_1$ and $4b_2$.[11] At energies above 398 nm (3.115 eV) and below 248 nm, where only excitation to the (1) $^2B_2$ state is likely,[12, 13] NO ($^2\Pi_{1/2,3/2}$) and O (^3P_J) are observed as the only photoproducts. Miyawaki et al. studied the oxygen fragment spin-orbit state distribution following fragmentation at several wavelengths from 212 to 355 nm. They have shown a distribution of $^3P_2$:$^3P_1$:$^3P_0$ of (1:0.19:0.03) after dissociation at 355 nm. This is quite different from the statistical, infinite-temperature, limit of (5:3:1).[14] Hsieh et al. have confirmed this finding using a "core-sampling" technique where they found a distribution of 1:0.21:0.05 for the populations of ($^3P_2$: $^3P_1$: $^3P_0$).[15] Both of these findings are in good agreement with that of Mons and Dimocoli who studied the distribution at 360 nm.[16] At 248 nm the excitation to (2) $^2B_2$ state becomes possible. At the excitation threshold only NO and O(^3P) are observed once again. At 243 nm (5.102 eV) production of O ($^1D_2$) is also observed in addition to O(^3P_J).[17] While the (2) $^2B_2$ state correlates adiabatically to the lowest channel and would then form O(^3P_J) it diabatically correlates to the O(^1D) channel through an avoided crossing. Schinke proposed that coupling of this state with the (4) $^2A_2$ state occurs at the avoided crossing and allows for the production of O($^1D_2$).

Of these two pathways excitation to the (1) $^2B_2$ state is of the most important to this thesis as it is accessible at 355 nm and will be the focus of the review below.

4.1 The First Absorption Band at 398-249 nm.

Photodissociation via excitation of the (1) $^2B_2$ state, i.e. from 398 nm to 249 nm leads to dissociation into NO ($^2\Pi_\Omega$) and O (^3P_J) and has been studied by several researchers using a variety of techniques.[18, 19]

Jost and Nygard [20] were able to determine a precise measure of the energy required for dissociation in the first absorption band of NO_2. Using laser induced fluorescence the group found a dissociation energy of 25128.57 +/- 0.05 cm^{-1} or 397.953 nm +/-0.001 nm. Additionally, the authors pointed out that the excited state has a strong vibronic interaction with the ground state; however, they were not able to fully characterize it. At threshold only the lower spin orbit state of NO ($^2\Pi_{1/2}$) in conjunction with O ($^3P_2$) are formed. The appearance energies for NO ($^2\Pi_{3/2}$), O($^3P_1$, and $^3P_0$) are 119.82, 158.27, and 226.972 cm^{-1} higher in energy respectively.[21, 22]

4.1.1 Dissociation Rate and Anisotropy

Bezel and Wittig[17] have studied the rotational dependence of the NO_2 parent molecule on the unimolecular RRKM dissociation rate following photoexcitation and found that there was no change in the rate following addition of 100 cm^{-1} of rotational energy. This is somewhat surprising as the authors have shown that near-threshold introduction of higher excess energy results in an increase in dissociation rate in a stepwise manner with steps approximately 100 cm^{-1} wide.[5] The workers attributed the unusual dependence of the dissociation quantum yield to complex rovibrational dynamics in the excited (1) $^2B_2$ state. It has been shown that a conical intersection (CI) at low energy mixes this excited state

with the ground state at a bond angle of 108° and approximately 1.2 eV.[23] Population in the excited state is theorized to transfer to the ground in a stepwise manner.[24, 25]

Chapter 1.4.2 describes the anisotropy parameter, β, the vector correlations and the angular distribution of dissociating molecules. The β parameter for the dissociation of NO_2 has been studied extensively as it yields a great deal of information about the dissociation process. The anisotropy parameter gives information on the rate of dissociation. When fragmentation is slow, i.e. slower than the rotational period of the excited molecule the information about the initial molecular orientation is lost and β takes on a value of 0, this is known as the "axial recoil limit". In the opposite limit, that is where dissociation is infinitely fast, if the recoil direction is at an angle, χ, to the transition dipole moment, the anisotropy parameter assumes the value $\beta = 2P_2\left(\cos\left(\chi\right)\right)$. [7, 26] Monti et al.[10] have shown that this corresponds to a value of approximately 1.54; experimentally they found a maximum β = 1.6 +/-0.1 when detecting O $^3P_2$. This is also consistent with β = 1.4 observed at a dissociation energy of 355 nm in the study by Hradil et al.[27]

Matthews and Softley[28] studied the anisotropy parameter β of the O(^3P_J) photofragment as a function of available energy. They found remarkable fluctuations in the value of β with respect to excess energy near the dissociation threshold. It was observed that β ranged from 0 to 1.6 converging at 1.5 for all values of J at high excess energies. The anisotropy parameter was also found to fluctuate differently for each of the two values of J studied (J = 1.5, 2.5), see Figure 4.5. The fluctuation in the β parameter is indicative of the strong coupling of the ground state resonances with the transition state during fragmentation. The excited state reaches the CI within 10 fs[24] and couples with the ground state within 100

fs. This causes the dissociation rate of NO_2 to be highly dependent on excess energy, from 100 fs at high excess energy, to around 10 ps near threshold. At threshold, where the rate is limited by the time scale of vibrational energy redistribution, the rate can be described by statistical theories as shown by the groups of Reisler,[19, 29, 30] Wittig[5, 18], Mons[16] and recently by Dupré.[31] On the other hand, at larger excess energies the dissociation process is fast and non-statistical as shown by Matthews[28], Zacharias[32] and Mons[33]. The difference in rate is, of course, reflected in the lifetimes of the molecule prior to dissociation. A longer lifetime will allow the molecule to reorient itself before dissociation, which in turn affects the value of the anisotropy parameter, β. The large fluctuations of β can thus be attributed, at least in part, to difference in rate between the different states.

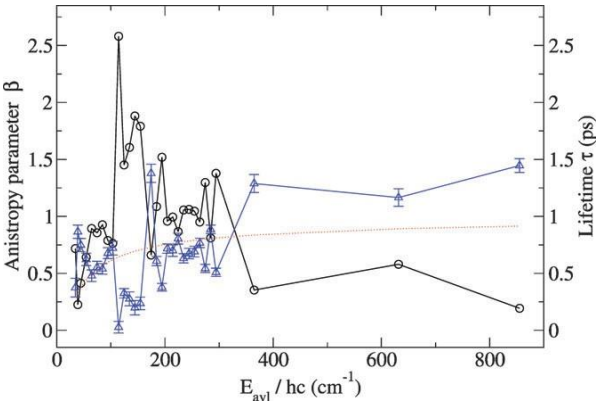

Figure 4.5: Anisotropy parameter β (triangles, blue line) with the corresponding lifetimes of each fragment (circles, black line). A clear inverse relationship is evident. Reproduced from Matthews.[28]

Reid and Reisler attributed the differences in the anisotropy parameter to overlapping resonances in the parent molecule that couple to the transition state which is similar in structure to the products.[19] Each fragment channel is correlated with a different superposition of the individual resonances and since the lifetimes differ, this leads to a different β parameter.[28]

Hradil and co-workers investigated the anisotropy parameter at 355 nm in a molecular beam of a NO_2-O_2 mixture in helium and found a β value of 1.2.[27, 34] The authors suggest that this yields a recoil angle of between 23° and 39°. The angular anisotropy parameter of NO_2 photolysis as a function of photolysis energy has also been studied at 371.7, 354.7, 338[9] and 308 nm.[17] The results show that β decreases with increasing NO fragment rotational energy but decreasing vibrational energy. Demyanenko et al.[9] show that over the range of 371.7-338 nm there is relatively little dependence on the excitation wavelength and that the largest determining factor of β is the rotational energy. This was found by comparing the translational energy of the fragments and the anisotropy parameter for each excitation wavelength (Figure 4.6).

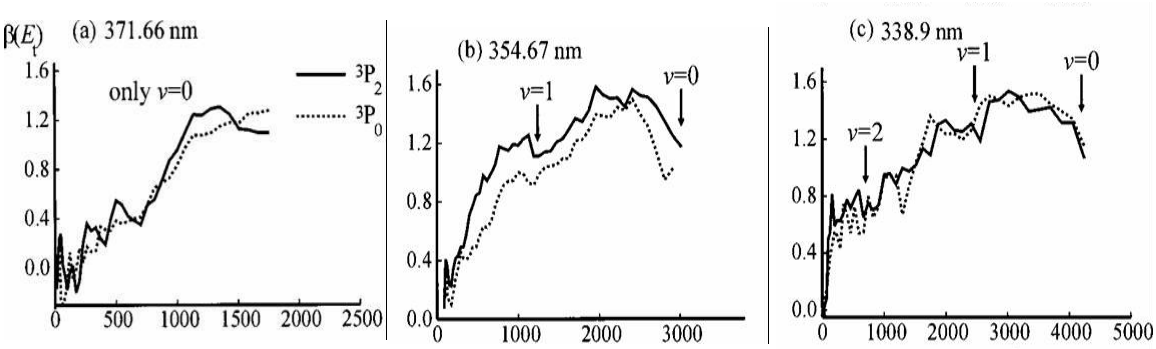

Figure 4.6: Dependence of β on translational energy in cm^{-1} (x-axis) for three different photolysis energies, for $^3P_2$ and $^3P_0$ oxygen following photolysis from NO_2. Reproduced from Demyanenko et al.[9]

Energy conservation demands that the translational energy of the NO fragment decreases as the rotational energy of the NO fragment increases for a given exciation energy and vibrational level (v=0). With decreasing translational energy it is also apparent that the anisotropy parameter decreases, and that β for O ($^3P_2$) and ($^3P_0$) is quite similar. Brouard et al.[17] in similar experiments at 308 nm, have found similar anisotropy parameter dependences. The correlation between β and the rotational distribution of the NO fragment

is indicative of a decrease in the ONO angle and subsequent asymmetric stretching during dissociation.[1]

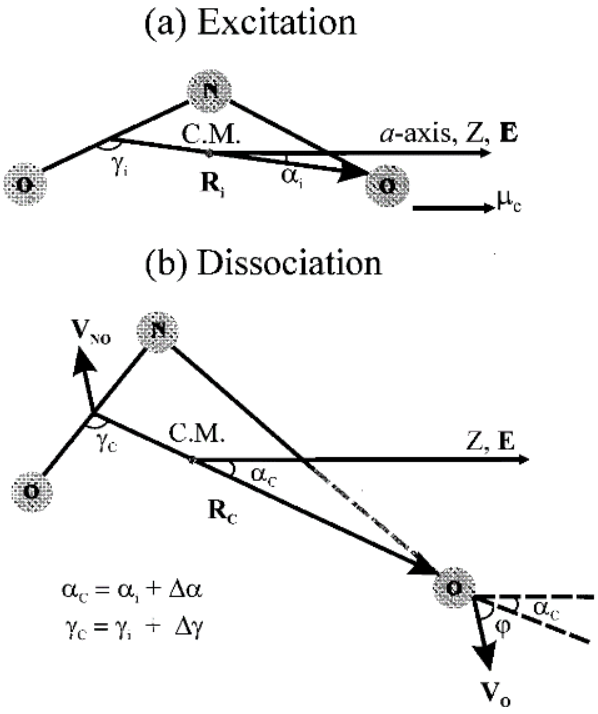

Figure 4.7: Geometry of NO_2 prior to excitation (a) and following excitation (b). E is the polarization vector of the laser, α_i is the initial angle between R_i and the laser polarization vector. R is the vector from the centre of mass of the NO and the departing oxygen atom. μ is the transition dipole moment and connects the two oxygen atoms. In the dissociation geometry we see that the ONO angle has decreased and the NO bond lengths have changed. Reproduced from Demyanenko.[8]

4.1.2 Translational, Rotational and Vibrational Distributions

The fragmentation rate affects the resulting energy distributions of the molecule. In the work of Brouard it was found that a population inversion of the vibrational states in the NO fragment for ν=0, 1 and 2 is present at dissociation energies of 308 nm. Robie et al.[35] at 369 nm and Zacharias[32] also show that the vibrational distribution is not well predicted by phase space theory, with a higher proportion found in the upper states than what would be expected. This is in contrast to work done by Harrison and co-workers who showed that the vibrational populations of $P_{(v=0)}$= 62% and $P_{(v=1)}$= 38% at 355 nm and 57% to 43% at 351 nm were consistent with a statistical model developed by Klippenstein and Radivoyeitch. Their statistical model combines variational RRKM theory with ab initio calculations.[36] The model predicts a vibrational distribution of $P_{(v=0)}$ = 60.7% and $P_{(v=1)}$ = 39.3%,[37] and includes constraints in the form of restrictions on couplings between the parent molecule's degrees of freedom. Hunter et al. has shown that this method can be used to predict the values found by Robie[38] and propose that these "dynamical constraints" are responsible for the success of the model.

The NO fragment rotational state distributions mirror the values for the anisotropy parameter. Experiments of NO_2 photodissociation at room temperature have shown that the NO fragment rotational distributions in both available vibrational states can be modeled with an RRKM type statistical simulation,[39] while at higher energy the rotational distribution is not statistical, i.e. it is not described by a Maxwell-Boltzmann distribution and a rotational temperature. Studies of jet-cooled NO_2 photodissociation have shown NO fragment rotational distributions that are not easily fit by statistical models even near threshold, although they have been fit to phase-space theory models.[35,40] More recently

Townsend et al. have used the direct current (DC) slice ion imaging method to show that the rotational distributions in both vibrational levels (ν=0 and 1) are bimodal. The authors also measured a unimodal distribution in translational energy for the ν=0 vibrational state and bimodal translational energy distribution for the ν=1 state with NO fragment energies peaking at 1000 and 2600 cm^{-1}.[41] Knepp et al. studied the photodissociation dynamics of gas-phase NO_2 at 309 nm.[42] At this wavelength there is enough energy to excite to the ν=3 NO vibrational state. The authors find that the NO vibrational state populations decrease monotonically from ν = 0-3, and that the rotational state distributions are highly dependent on the vibrational state with single maxima for ν=0 and 1, a flat distribution for ν=2 and oscillatory for ν=3. These results were in relatively good agreement with studies found at much higher energy from McFarlane et al.[43]

4.1.3 Summary of features of NO_2 photolysis from 400 nm-250 nm

Exposure of NO_2 to 400-250 nm light leads to excitation to the (1) $^2B_2$ state, corresponding to the $6a_1 \leftarrow 4b_2$ transition. This state is found to be strongly coupled to the ground state as they are connected through a conical intersection near the Franck-Condon region.[24] The partitioning of the NO fragment states, i.e. the vibrational and rotational distributions as well as the spatial anisotropy, are found to be statistical near the threshold to dissociation and non-statistical above it.[44] The fast dissociation is suggestive of a dissociation in the axial recoil limit whereby the molecule bends towards a smaller angle and an asymmetric stretch occurs during dissociation before redistribution of this energy is possible (see Figure 4.7 for a geometric sketch of the process given by Demyanenko).[9] The lifetimes

of the dissociating molecule were found to vary from hundreds of femtoseconds to tens of picoseconds, i.e. in the range of one rotational period. This difference in lifetimes drastically impacts the observed β parameter, as the axial recoil limit no longer holds when rotational motion is superimposed on the dissociation dynamics. It has also been shown that the anisotropy parameter β varies with small differences in the excess vibrational energy above threshold, again indicative of a complex dissociation process. Taken together these findings suggest that dissociation is dynamic with respect to the vibrational modes. These differences are attributed the picture of NO_2 photodissociation reported by Reid and Reisler, and may be attributed to overlapping resonances in the parent molecule. To study this further, the effect of rotational energy of the parent molecule on the rate of the decomposition has been studied; an addition of 100 cm^{-1} of additional rotational energy did not lead to an appreciable difference into the rate constant, signaling complex dynamics within the ro-vibrational states.

It is clear that the photolysis characteristics in the first absorption bands are quite complex and interesting.

4.2 Condensed-Phase Photodissociation of NO_2

Before discussing photochemical studies of NO_2 trapped in condensed phases such as rare gas matrices and water ice, it is important to briefly address the adsorption processes of NO_2 on, and into, these films.

4.2.1 NO_2 adsorption onto ice and icy dust grains.

The study of NO_2 deposition has been an interesting area of research as the adsorption characteristics i.e. adhesion rate, dimerization rate, etc. of NO_2 are quite varied depending on temperature, pressure and substrate. Saastad et al. and Bartels-Rausch have both found that there is little uptake of NO_2 onto pure ice surfaces at pressures and temperatures found in stratospheric conditions.[45, 46] However there has been evidence for NO_2 deposition onto these ice surfaces when dust particles are present as a substrate.[47, 48] Additionally, Bernstein has shown that in the ice grains found in comets and in the ISM there is evidence for NO_2.[49]

The majority of NO_2 condensed inside or on top of ice on Earth is found in polar snow packs. Here NO_2 is typically present in the form of its dimer, N_2O_4, however, there is evidence that it is also present as the monomer.[50-53] Sato et al. also showed that while deposition occurs as N_2O_4, further photochemistry produces NO_2.[52] An additional source for NO_2 molecules in the ice pack is the photodecomposition of nitrate, NO_3^-.[51] The study of NO_2 reactivity following adsorption has shown several interesting results including oxygen atom production,[53] and HONO production.[54] There is also evidence that vibrationally excited gaseous NO_2, upon reaction with H_2O, forms OH radicals.[55, 56] This production of OH is given as a possible mechanism for the apparent excess of OH radicals in the artic regions found by Domine et al.[57] While this thesis utilizes inert gas matrices, the apparatus can be used in the future to monitor the NO_2-ice deposition conditions to study all of the possible different types of NO_2:H_2O ice matrices.

4.2.2 NO_2/N_2O_4 photolysis in and on condensed matrices.

Due to the fact that NO_2 has a propensity for dimerizing into N_2O_4 when condensed, some of the literature of condensed N_2O_4 photolysis will also be discussed here. There is a relative lack of study of the photodissociation dynamics of NO_2 and N_2O_4 in and on ices when compared to the large number of studies concerned with gas phase NO_2. The studies that do exist show that the photochemistry is quite different compared to the gas phase - as might be expected due to the proximity of other molecules and cage effects.

Photodissociation studies of NO_2 on metal surfaces, have shown that spontaneous formation of N_2O_4 occurs upon deposition. Photodissociation of N_2O_4 at 3.5 to 6.4 eV produces NO fragments with exceedingly high rotational energy [58] and extensive metal-induced effects on translational and vibrational modes are observed. Dixon-Warren et al [59] studied the photodissociation NO_2 on a LiF surface cooled to 100 K at a dissociation wavelength of 248 nm. Through an infrared study prior to dissociation the authors showed that the NO_2 dimerized on the surface forming mostly N_2O_4. Vibrational levels of the NO photolysis product up to ν=7 were observed. Translational distributions for all vibrational levels were fit to a single Boltzmann distribution and were all very similar with the exception of ν=0 which showed the presence of much slower NO fragments. The vibrational level population was shown to be bimodal with one peak at ν=0 and a second at ν=3-4. Interestingly, the rotational population distribution could be fit to a single Boltzmann distribution. The lower vibrational states ν=0-1 had a rotational temperature of roughly 350-750 K, while higher vibrational states ν=6 and 7 had temperatures up to 1200 K.

Fournier et al.[60] condensed a mixture of NO_2 and argon in a 1:1000 molar ratio resulting in trapped NO_2 molecules. Photolysis was conducted at 147 nm using a xenon lamp and studied by thermoluminescence. The results were found to be quite different compared to that of the gas phase; the initial step dissociation is similar; however, due to the cage effect the O atom and the NO molecule are found to recombine, and this occurrence is found to increase after heating the matrix to 14K. Additionally; the authors found that some of the oxygen atoms are labile in the matrix and may combine with another oxygen atom, forming O_2, or with a second NO molecule, forming, again, NO_2. It has since been shown that transport of the oxygen atoms through the argon matrix is along defects.[61]

Cocke et al. [62] have studied photolysis of NO_2 in an argon matrix irradiating with 350 - 450 nm light. Additionally, the group used a much higher concentration of NO_2 using a 1:54 dilution. This higher concentration allowed for possible study of two NO_2 molecules being trapped in the same cage or nearby. Following photolysis the group found evidence for NO and O (^3P) formation which can move throughout the matrix albeit in a limited way. The group points out that diffusion through the matrix is likely due to matrix defects, however, they do suggest it is possible that this is from the argon lattice opening through collisions with the dissociated fragments. There was also evidence for a considerable amount of reaction between NO and O forming N_2O_3 and N_2O_5. A related exploration was possible due to the fact that there was a large amount of water impurity (desorption from the walls of the chamber) and the group was able to study water-NO_2 reactions. Following irradiation, the ratio of high to low surface area water ice increases; found by monitoring the libration mode. It is suggested that this is due to nanoparticulate ice formation. Due to

the large surface to volume ratio there is a large amount of dangling OH bonds which can cause further reaction with NO_2.

While these two studies have examined the possible photochemical reaction of photoproduct molecules that remain in the matrix, neither describe the photodynamics of the molecules that can leave the matrix into the gas phase. Additionally, while these studies give us an interesting look into the reactivity at high and low energies, to my knowledge there have been no studies on the photodynamics of monomeric NO_2 trapped in either a water or argon matrix.

NO_2 forms N_2O_4 when deposited on pure water ice films, which is one of the easiest ways of depositing NO_2, and it is not surprising that photolysis of N_2O_4 has been studied more extensively than monomeric NO_2. Susa and Koda[63] have studied the photolysis of N_2O_4 following irradiation at 193 nm using a ArF excimer laser and a TOF-MS detection scheme; Here N_2O_4 was deposited on, both, annealed and non-annealed water ice films. NO_2, NO and O are found as the only products from the ice surface. It is suggested that N_2O_4 dissociates into 2 NO_2 molecules - one of which is excited to a higher electronic state which dissociates into NO and oxygen. The group also shows that there is a large difference in the photochemistry of the two ice surfaces; it is found that in the non-annealed ice there is a lower yield of NO_2 relative to NO as compared to the annealed ice. This is proposed to be due to the fact that NO_2 can be reabsorbed into the ice when it collides with the surface, whereas the NO molecules do not stick when they collide with the ice surface. It is found that the NO molecules have a bimodal distribution in their speeds. The ratio of fast to slow NO is 1:0.81 for the non-annealed ice and 1:0.22 for annealed ice; this may be indicative

of the NO fragment distributing some of its kinetic energy into the ice matrix due to collisions inside the non-annealed ice matrix.

Yabushita et al.[58] have studied the photodynamics of N_2O_4 deposited on the surface of water ice following irradiation at 192, 248 and 351 nm. They were using a REMPI process coupled with photofragment time-of-flight spectroscopy along with infrared reflection absorption spectroscopy (IRAS) of the surface. The IRAS studies show that the surface is comprised solely of the usual D_{2h} N_2O_4. At all three wavelengths NO and NO_2 were formed. At 193 and 248 nm $O(^3P_j)$ was also found where the majority of the population was in the lowest level J = 2. The NO molecule was found to be highly rotationally excited in the v = 0 vibrational level; likely due to the same rapid decrease in bending angle as observed in the gas phase. The translational energy was found to be bimodal with a fast and slow component. The slow component dominated the population. It was found that the contribution of the slow component increases from 93% to 99% with decreasing energy from 193 to 351nm. Rieley et al. conducted photodissociation experiments of a physisorbed ordered monolayer N_2O_4 on 30 monolayer-thick water ice surfaces at 355 nm. Interestingly, in contrast to the work of Yabushita, the translational energy distribution was found to fit a single Boltzmann distribution (T_{trans} = 200K) very well, likely due to the use of single layer deposition.[64]

Given the vast research into gas phase photolysis of NO_2 it is surprising that there is a relatively small amount of similar work done on trapped monomeric NO_2. By taking advantage of our apparatus design we can get a full description of the photolysis of NO_2 while it is trapped in either an argon or water matrix. Additionally, as we are able to modify our ice sample through deposition rates, composition, and temperature, we will be able to

study all the different structures observed in the environment. Here we demonstrate the capabilities of the setup by characterizing the photodissociation dynamics of NO_2 in an argon matrix. The trapped NO_2 molecules experience relatively little interaction with the atoms of the argon matrix yielding a "simple" experiment, with which we can test the waters, so to speak, leaving room for more complicated H_2O ices to future studies.

CHAPTER 4 REFERENCES

[1] I. Wilkinson, B. J. Whitaker, Some remarks on the photodynamics of NO_2, Annual Reports Section "C" (Physical Chemistry) 106 (2010) 274-304.

[2] I. Wilkinson, B.J. Whitaker, Photodissociation of NO_2 in the $(2)^2B_2$ state: A slice imaging study and reinterpretation of previous results, The Journal of Chemical Physics 129 (2008) 154312.

[3] R. Schinke, Theoretical study of the $\tilde{D}\rightarrow\tilde{C}$ emission spectrum of NO_2, The Journal of Chemical Physics 129 (2008) 124303.

[4] R. Schinke, S.Y. Grebenshchikov, H. Zhu, The photodissociation of NO_2 in the second absorption band: Ab initio and quantum dynamics calculations, Chemical Physics 346 (2008) 99-114.

[5] S.I. Ionov, G.A. Brucker, C. Jaques, Y. Chen, C. Wittig, Probing the $NO_2\rightarrow NO+O$ transition state via time resolved unimolecular decomposition, The Journal of Chemical Physics 99 (1993) 3420-3435.

[6] J. Orphal, J. Photochem Photobio A: Chem, 157 (2003) 185-209.

[7] C. Jonah, Effect of Rotation and Thermal Velocity on the Anisotropy in Photodissociation Spectroscopy, The Journal of Chemical Physics 55 (1971) 1915-1922.

[8] H.-P. Loock, J. Cao, C.X.W. Qian, Vibrational modification of the spatial anisotropy parameter in photodissociation. A classical trajectory study, Chemical Physics Letters 206 (1993) 422-428.

[9] A.V. Demyanenko, V. Dribinski, H. Reisler, H. Meyer, C.X.W. Qian, Product quantum-state-dependent anisotropies in photoinitiated unimolecular decomposition, The Journal of Chemical Physics 111 (1999) 7383-7396.

[10] O.L.A. Monti, H. Dickinson, S.R. Mackenzie, T.P. Softley, Rapidly fluctuating anisotropy parameter in the near-threshold photodissociation of NO_2, The Journal of Chemical Physics 112 (2000) 3699-3709.

[11] G. Herzberg, Molecular Spectra and Molecular Structure: Volume III Electronic Spectra and Electronic Structure of Polyatomic Molecules, 1st ed., Van Nostrand Reinhold, New York, 1966.

[12] C.G. Stevens, R.N. Zare, Rotational analysis of the 5933 Å band of NO_2, Journal of Molecular Spectroscopy 56 (1975) 167-187.

[13] G.E. Busch, K. R.Wilson, J. Chem. Phys. 56 (1972).

[14] J. Miyawaki, T. Tsuchizawa, K. Yamanouchi, S. Tsuchiya, Spin-orbit state distribution of atomic oxygen (^3P_J) produced by photodissociation of nitrogen dioxide, Chemical Physics Letters 165 (1990) 168-170.

[15] C.-H. Hsieh, Y.-S. Lee, A. Fujii, S.-H. Lee, K. Liu, Photodissociation of NO_2 at 355 nm: pair correlation, Chemical Physics Letters 277 (1997) 33-38.

[16] M. Mons, I. Dimicoli, Photodissociation of NO_2. Internal energy distribution and anisotropies in the fragments, Chemical Physics 130 (1989) 307-324.

[17] M. Brouard, R. Cireasa, A.P. Clark, T.J. Preston, C. Vallance, The photodissociation dynamics of NO_2 at 308nm and of NO_2 and N_2O_4 at 226nm, The Journal of Chemical Physics 124 (2006) 064309.

[18] I. Bezel, P. Ionov, C. Wittig, Photoinitiated unimolecular decomposition of NO_2: Rotational dependence of the dissociation rate, The Journal of Chemical Physics 111 (1999) 9267-9279.

[19] S.A. Reid, H. Reisler, Unimolecular Reaction of NO_2: Overlapping Resonances, Fluctuations, and the Transition State, The Journal of Physical Chemistry 100 (1996) 474-487.

[20] R. Jost, J. Nygård, A. Pasinski, A. Delon, The photodissociation threshold of NO_2: Precise determination of its energy and density of states, The Journal of Chemical Physics 105 (1996) 1287-1290.

[21] A. Kramida, Ralchenko, Yu., Reader, J. and NIST ASD Team, NIST Atomic Spectra Database (version 5.3), National Institute of Standards and Technology, Gaithersburg, MD, 2015.

[22] K.P. Huber, G. Herzberg, Molecular Spectra and Molecular Structure: IV Constants of Diatomic Molecules, 1st ed., Van Nostrand Reinhold, New York, 1979.

[23] C.F. Jackels, E.R. Davidson, The two lowest energy $^2A'$ states of NO_2, The Journal of Chemical Physics 64 (1976) 2908-2917.

[24] M. Sanrey, M. Joyeux, Quantum mechanical and quasiclassical investigations of the time domain nonadiabatic dynamics of NO_2 close to the bottom of the X^2A_1-A^2B_2 conical intersection, The Journal of Chemical Physics 125 (2006) 014304.

[25] A. Delon, R. Jost, The NO_2 vibronic levels near the X^2A_1–A^2B_2 conical intersection: Jet cooled laser induced fluorescence between 11680 and 13900 cm−1, The Journal of Chemical Physics 110 (1999) 4300-4308.

[26] H. Kim, K.S. Dooley, S.W. North, G.E. Hall, P.L. Houston, Anisotropy of photofragment recoil as a function of dissociation lifetime, excitation frequency, rotational level, and rotational constant, The Journal of Chemical Physics 125 (2006) 133316.

[27] V.P. Hradil, T. Suzuki, S.A. Hewitt, P.L. Houston, B.J. Whitaker, An investigation of the 355 nm photodissociation of NO_2 by state-resolved photofragment imaging, The Journal of Chemical Physics 99 (1993) 4455-4463.

[28] S.J. Matthews, S. Willitsch, T.P. Softley, Fully state-selected VMI study of the near-threshold photodissociation of NO_2: variation of the angular anisotropy parameter, Physical Chemistry Chemical Physics 9 (2007) 5656-5663.

[29] S.A. Reid, D.C. Robie, H. Reisler, Fluctuations in the unimolecular decomposition of jet-cooled NO_2: Implications for overlapping resonances and the transition state, The Journal of Chemical Physics 100 (1994) 4256-4271.

[30] S.A. Reid, A. Sanov, H. Reisler, Resonances and fluctuations in the unimolecular reaction of NO_2, Faraday Discussions 102 (1995) 129-146.

[31] P. Dupré, Photodissociation resonances of jet-cooled NO_2 at the dissociation threshold by CW-CRDS, The Journal of Chemical Physics 142 (2015) 174305.

[32] H. Zacharias, M. Geilhaupt, K. Meier, K.H. Welge, Laser photofragment spectroscopy of the NO_2 dissociation at 337 nm. A nonstatistical decay process, The Journal of Chemical Physics 74 (1981) 218-225.

[33] M. Mons, I. Dimicoli, State selective kinetic distribution of photofragments, Chemical Physics Letters 131 (1986) 298-302.

[34] T. Suzuki, V.P. Hradil, S.A. Hewitt, P.L. Houston, B.J. Whitaker, Two-dimensional imaging of state-selected photofragments: the 355 nm photolysis of NO_2, Chemical Physics Letters 187 (1991) 257-262.

[35] D.C. Robie, M. Hunter, J.L. Bates, H. Reisler, Product state distributions in the photodissociation of expansion-cooled NO_2 near the NO($X\ ^2\Pi$) v=1 threshold, Chemical Physics Letters 193 (1992) 413-422.

[36] S.J. Klippenstein, T. Radivoyevitch, A theoretical study of the dissociation of NO_2, The Journal of Chemical Physics 99 (1993) 3644-3653.

[37] J.A. Harrison, X. Yang, M. Roesslein, P. Felder, J.R. Huber, Photodissociation of NO2 at 355 and 351 nm Investigated by Photofragment Translational Spectroscopy, The Journal of Physical Chemistry 98 (1994) 12260-12269.

[38] M. Hunter, S.A. Reid, D.C. Robie, H. Reisler, The monoenergetic unimolecular reaction of expansion-cooled NO_2: NO product state distributions at excess energies 0–3000 cm−1, The Journal of Chemical Physics 99 (1993) 1093-1108.

[39] P.A. Elofson, E. Ljungström, Stochastic simulation of $NO_2(X\ ^2A_1)\rightarrow O(^3P_j)$+NO($X\ ^2\Pi_\Omega$ photodissociation: rotational excitation of product NO, Chemical Physics 165 (1992) 323-337.

[40] N. Changlong, L. Hua, J. Pfab, Photodissociation of jet-cooled nitrogen dioxide at 355 nm: strong alignment and oscillations in the rotational state distributions of the nitric oxide (v=1) fragment, The Journal of Physical Chemistry 97 (1993) 7458-7464.

[41] D. Townsend, M.P. Minitti, A.G. Suits, Direct current slice imaging, Review of Scientific Instruments 74 (2003) 2530.

[42] P.T. Knepp, A.C. Terentis, S.H. Kable, Photodissociation dynamics of NO_2 at moderately high energy (λ=309.1 nm; Eavail=7222 cm−1), The Journal of Chemical Physics 103 (1995) 194-204.

[43] J. McFarlane, J.C. Polanyi, J.G. Shapter, Photodissociation dynamics of NO_2 at 248 nm, Journal of Photochemistry and Photobiology A: Chemistry 58 (1991) 139-172.

[44] H. Sato, Photodissociation of Simple Molecules in the Gas Phase, Chemical Reviews 101 (2001) 2687-2726.

[45] O.W. Saastad, T. Ellermann, C.J. Nielsen, On the adsorption of NO and NO_2 on cold H_2O/H_2SO_4 surfaces, Geophysical Research Letters 20 (1993) 1191-1193.

[46] T. Bartels-Rausch, M. Brigante, Y.F. Elshorbany, M. Ammann, B. D'Anna, C. George, K. Stemmler, M. Ndour, J. Kleffmann, Humic acid in ice: Photo-enhanced conversion of nitrogen dioxide into nitrous acid, Atmospheric Environment 44 (2010) 5443-5450.

[47] C.E. Kolb, R.A. Cox, J.P.D. Abbatt, M. Ammann, E.J. Davis, D.J. Donaldson, B.C. Garrett, C. George, P.T. Griffiths, D.R. Hanson, M. Kulmala, G. McFiggans, U. Pöschl, I. Riipinen, M.J. Rossi, Y. Rudich, P.E. Wagner, P.M. Winkler, D.R. Worsnop, C.D. O' Dowd, An overview of current issues in the uptake of atmospheric trace gases by aerosols and clouds, Atmos. Chem. Phys. 10 (2010) 10561-10605.

[48] M. Ndour, B. D'Anna, C. George, O. Ka, Y. Balkanski, J. Kleffmann, K. Stemmler, M. Ammann, Photoenhanced uptake of NO_2 on mineral dust: Laboratory experiments and model simulations, Geophysical Research Letters 35 (2008).

[49] M.P. Bernstein, Allamandola, L. J., Sandford, S. A., Complex Organics in Laboratory Simulations of Intersetllar/Cometary Ices, Life Sciences: Complex Organics in Space 19 (1997) 991-998.

[50] E. Ozensoy, C.H.F. Peden, J. Szanyi, Low Temperature H_2O and NO_2 Coadsorption on θ-Al_2O_3/NiAl(100) Ultrathin Films, The Journal of Physical Chemistry B 110 (2006) 8025-8034.

[51] A. Yabushita, N. Kawanaka, M. Kawasaki, P.D. Hamer, D.E. Shallcross, Release of Oxygen Atoms and Nitric Oxide Molecules from the Ultraviolet Photodissociation of Nitrate Adsorbed on Water Ice Films at 100 K, The Journal of Physical Chemistry A 111 (2007) 8629-8634.

[52] S. Sato, T. Senga, M. Kawasaki, Adsorption States and Photochemistry of NO_2 Adsorbed on Au(111), The Journal of Physical Chemistry B 103 (1999) 5063-5069.

[53] J. Wang, M.R. Voss, H. Busse, B.E. Koel, Chemisorbed Oxygen on Au(111) Produced by a Novel Route: Reaction in Condensed Films of NO_2 + H_2O, The Journal of Physical Chemistry B 102 (1998) 4693-4696.

[54] J. Wang, B.E. Koel, IRAS Studies of NO_2, N_2O_3, and N_2O_4 Adsorbed on Au(111) Surfaces and Reactions with Coadsorbed H2O, The Journal of Physical Chemistry A 102 (1998) 8573-8579.

[55] S. Li, J. Matthews, A. Sinha, Atmospheric Hydroxyl Radical Production from Electronically Excited NO_2 and H_2O, Science 319 (2008) 1657-1660.

[56] X. Li, F. Rohrer, A. Hofzumahaus, T. Brauers, R. Häseler, B. Bohn, S. Broch, H. Fuchs, S. Gomm, F. Holland, J. Jäger, J. Kaiser, F.N. Keutsch, I. Lohse, K. Lu, R. Tillmann, R. Wegener, G.M. Wolfe, T.F. Mentel, A. Kiendler-Scharr, A. Wahner, Missing Gas-Phase

Source of HONO Inferred from Zeppelin Measurements in the Troposphere, Science 344 (2014) 292-296.

[57] F. Dominé, P.B. Shepson, Air-Snow Interactions and Atmospheric Chemistry, Science 297 (2002) 1506-1510.

[58] A. Yabushita, Y. Inoue, T. Senga, M. Kawasaki, S. Sato, Photodissociation of N2O4 Adsorbed on Amorphous and Crystalline Water−Ice Films, The Journal of Physical Chemistry A 108 (2004) 438-446.

[59] St. J. Dixon-Warren, R. C. JAckson, J. C. Polanyi, H. Rieley, J. G. Shapter, H. Weiss, Photodissociation of NO_2 Adsorbed on LiF(001), The Journal of Physical Chemistry, 96 (1992) 10983-10994.

[60] J. Fournier, J. Deson, C. Vermeil, NO+O chemiluminescence in low temperature argon matrix, The Journal of Chemical Physics 67 (1977) 5688-5690.

[61] M.B. Ford, A.D. Foxworthy, G.J. Mains, L.M. Raff, Theoretical investigations of ozone vibrational relaxation and oxygen atom diffusion rates in Ar and xenon matrixes, The Journal of Physical Chemistry 97 (1993) 12134-12143.

[62] D.L. Cocke, J. A. G. Gomes, J. L. Gossage, K. Y. Li, C. J. Lin, S. Tandel, Water-related matrix isolation phenomena during NO_2 photolysis in argon matrix, Appl. Spectrosc. 58 (2004).

[63] A. Susa, S. Koda, Photochemistry of N_2O_4, J. Atmos. Chem. 45 (2003) 197.

[64] H. Rieley, D.J. Colby, D.P. McMurray, S.M. Reeman, Photodissociation Dynamics in Ordered Monolayers: Physisorbed N_2O_4, The Journal of Physical Chemistry B 101 (1997) 4982-4991.

Chapter 5

Resonance Enhanced Multiphoton Ionization Spectroscopy of Nitric Oxide Fragment and Fragment Time of Flight Profiles

5.1 Introduction

The apparatus described in Chapter 3 is capable of two non-imaging experimental techniques: REMPI spectroscopy, which monitors rovibronic state populations of the NO fragment following ionization, and fragment time-of-flight spectroscopy, which monitors the fragments' translational velocity of state-selected photoions. The fragment state distribution profiles of these two experiments yield information about the energy partitioning following dissociation.

5.1 REMPI Spectroscopy

The REMPI spectrum of the γ–band, i.e. the $^2\Pi_{1/2} \leftarrow {}^2\Sigma_{1/2}$ (0,0) and $^2\Pi_{3/2} \leftarrow {}^2\Sigma_{1/2}$ (0,0) transitions at 227-225.5 nm, were recorded. The delay between the photodissociation laser pulse (355 nm) and the REMPI laser pulse was set to either 9 μs, 18 μs, or 35 μs. The photodissociation laser was aimed at the NO_2 doped Ar-matrix on a cold finger at 20 K whereas the REMPI probe laser was focused to a spot about 3 mm above the matrix surface.

5.1.1 Laser Power Calibration and Background Subtraction

The relative amount of NO^+ formed is measured by recording the integrated peak intensity from an oscilloscope at a time interval corresponding to the arrival time for NO^+ using an

in-house built LabView program. The number of ions created is related to the photon flux of the ionization laser. The laser power is recorded using a photodiode and is used to calibrate the ion signal. Although the timing between ice dissociation and the molecular beam valve being opened was always set with the largest gap possible, some background NO_2 gas is always present. This background gas is also dissociated and ionized by the ionization beam. In order to measure the ion signal of NO coming from the ice after dissociation, the background signal must be subtracted from the overall recorded measurement. To obtain the NO^+ signal arising from the NO_2 background a REMPI spectrum was recorded with the dissociation laser blocked. This produces a REMPI spectrum that is attributed only to the background gas as the condensed phase sample remains trapped. As the signal of the background is also laser power dependent, the ionization laser power study was also conducted without the dissociation laser operating to calibrate this "blank" REMPI spectrum. The blank spectrum can then be used to subtract the background signal from REMPI spectrum recorded during the condensed phase experiment. The calibration steps are as follows:

1) The power dependence of the NO signal arising from background NO_2 gas was determined. Only the REMPI laser was used, i.e. photolysis of NO_2 was done at around 226 nm.
2) The REMPI spectrum of NO arising from photolysis of background NO_2 gas was obtained and the REMPI intensities were rescaled using the laser power dependence obtained in step one. The resulting spectrum is labelled as "REMPI blank".

3) The power dependence of the condensed phase photo-induced NO in Ar was determined under the normal experimental conditions. The signal now depends on both the photolysis and REMPI laser.
4) The REMPI spectrum of total NO was recorded, rescaled according to REMPI laser power. Using the data from step two, the background NO signal was then subtracted, yielding the ion signal for the NO fragment following dissociation from the NO_2:Ar sample.

5.1.2 Background NO_2 Laser Power Dependence

By holding the ionization laser's frequency constant at 226.26 nm (Q bandhead) and using three neutral density filters, the power dependence on the ion signal at the Q line bandhead can be recorded over the range that the laser power might fluctuate throughout the experiment. The same procedure was followed to find the power dependence of the Ar:NO_2 sample.

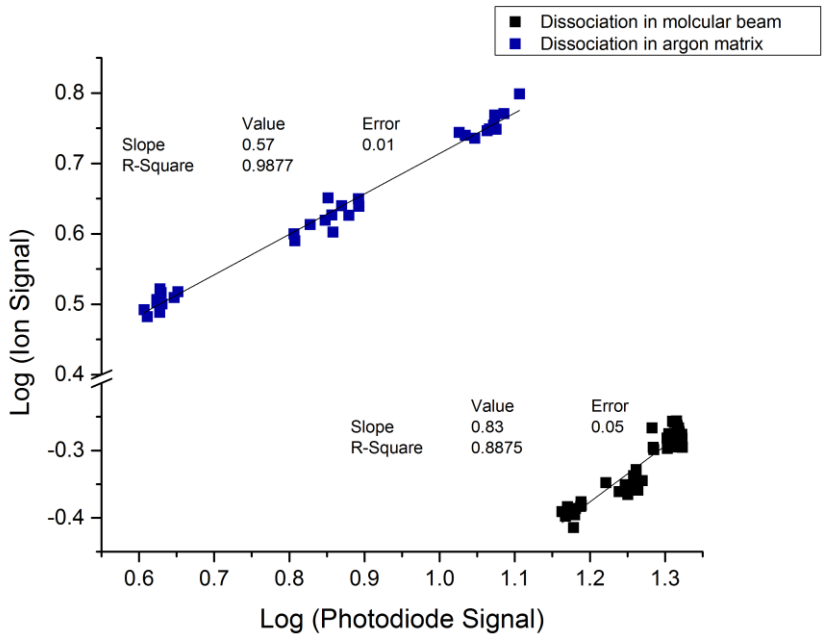

Figure 5.1: Integrated NO^+ ion signal as a function of laser intensity for background gas NO_2 (Black dots) and for NO formed by photodissociation of NO_2 from within the argon matrix (Blue dots). Dissociation of background NO_2 gas and subsequent ionization of the NO fragment involves three photons, the first dissociates the NO_2 molecule and the NO photofragment is then ionized in a two photon (1+1) REMPI process. When dissociation occurs in the matrix, only the two-photon ionization process is involved as the NO_2 is first fragmented by the Nd:YAG laser at 355 nm.

The difference in slope between the two fits illustrates the difference between the three photon process to probe NO from NO_2 photolysis and the two photon process that is required to detect NO that was produced by a different laser. The former process requires one photon to dissociate the NO_2 molecules and two photons for the 1+1 REMPI process to ionize the NO fragment. The latter process produces NO photofragments using a 355 nm laser aimed at the NO_2-doped Ar-matrix, and only the 1+1 REMPI process determines the power dependence. We expect these dependencies on laser intensity to be $S = I^3$ and $S = I^2$, respectively, but find much lower exponents of 0.83 and 0.57, respectively. This may point to the fact that the transitions are in the "saturation regime". It may also point to non-linear responses of either (or of both) the photodiode and the ion detector.

A REMPI spectrum of NO produced by photolysis of background NO_2 was taken. The resulting spectrum was then rescaled for laser intensity using the scaling exponent of 0.57 as obtained using the linear fit in Figure 5.1 and was used for background subtraction. The Ar:NO_2 spectrum is similarly rescaled using an exponent of 0.83, from which the calibrated background spectrum is then subtracted.

5.1.3 Resonance Enhanced Multiphoton Ionization Spectra

Rotational spectra were obtained by integrating the ion current to the power supply of the MCP through the Butterworth filter at each 0.002 nm increment of the dye laser. Spectra were obtained at three different delay intervals (9, 18 and 35 μs) between the dissociation and ionization laser. These three spectra are shown each three times and labelled respectively according to either their P, R or Q-branches, in order to show the individual transitions.

The line positions are given below for the different ΔJ branch transitions at each delay interval for clarity. The transitions are labeled using the convention given in PGOPHER[1], i.e. as $\Delta N \Delta J_{FF}$. Here, ΔN is denoted by a lowercase letter, ΔJ by an uppercase letter, which is followed by subscripts indicating the upper state F designation and the ground state F designation. If the transition is from a $F1$ to another $F1$ state or $F2$ to $F2$, then only one is shown. For instance, if the transition has $\Delta N=0$, $\Delta J=1$, and occurs from F1 of the ground state to F2 in the upper state, then the transition would be a qR21 transition.

5.1.3.1 P branch Transitions

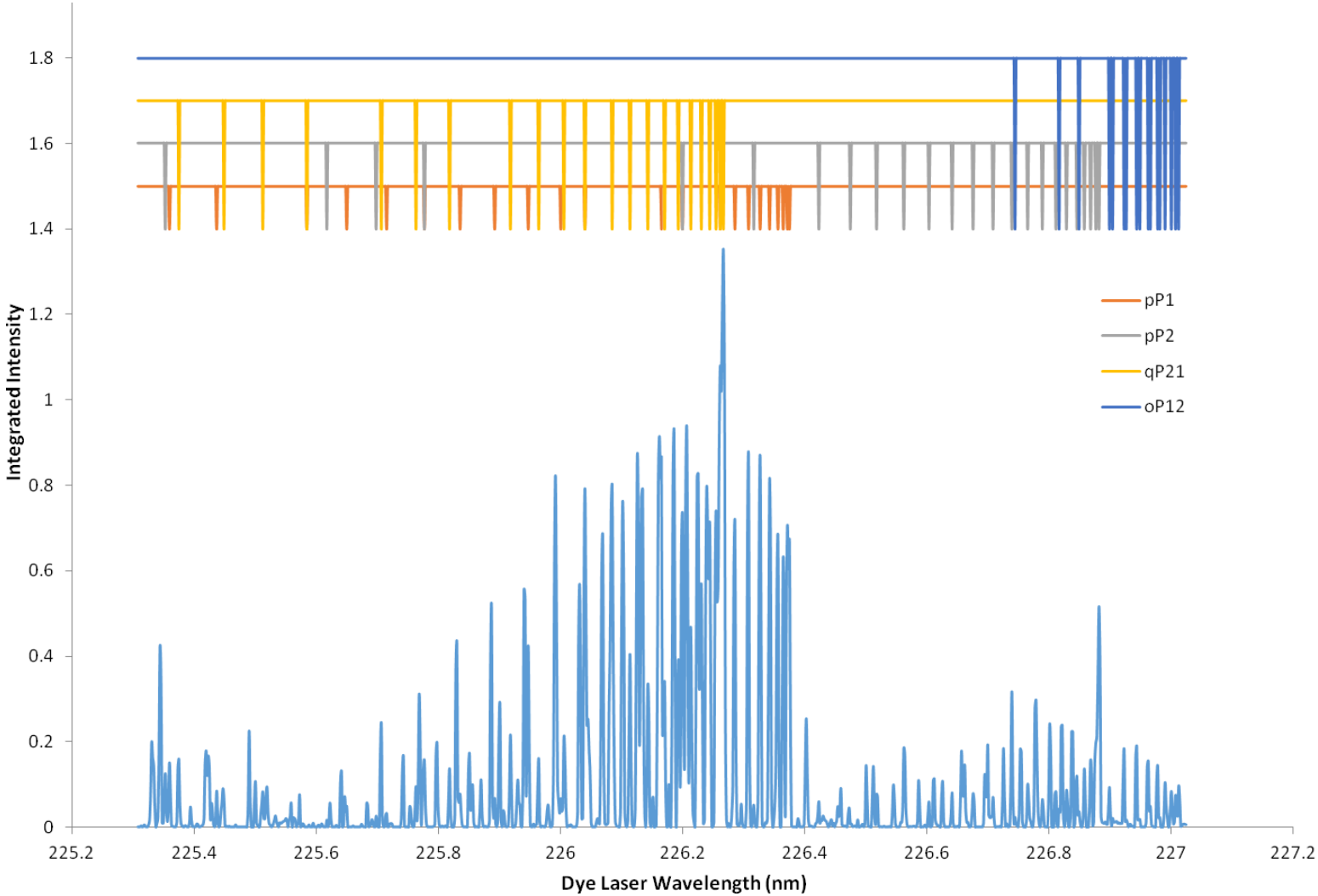

Figure 5.2: REMPI data of the NO fragment, 9 μs after dissociation. The vertical lines above the spectrum indicate the different P branch transitions.

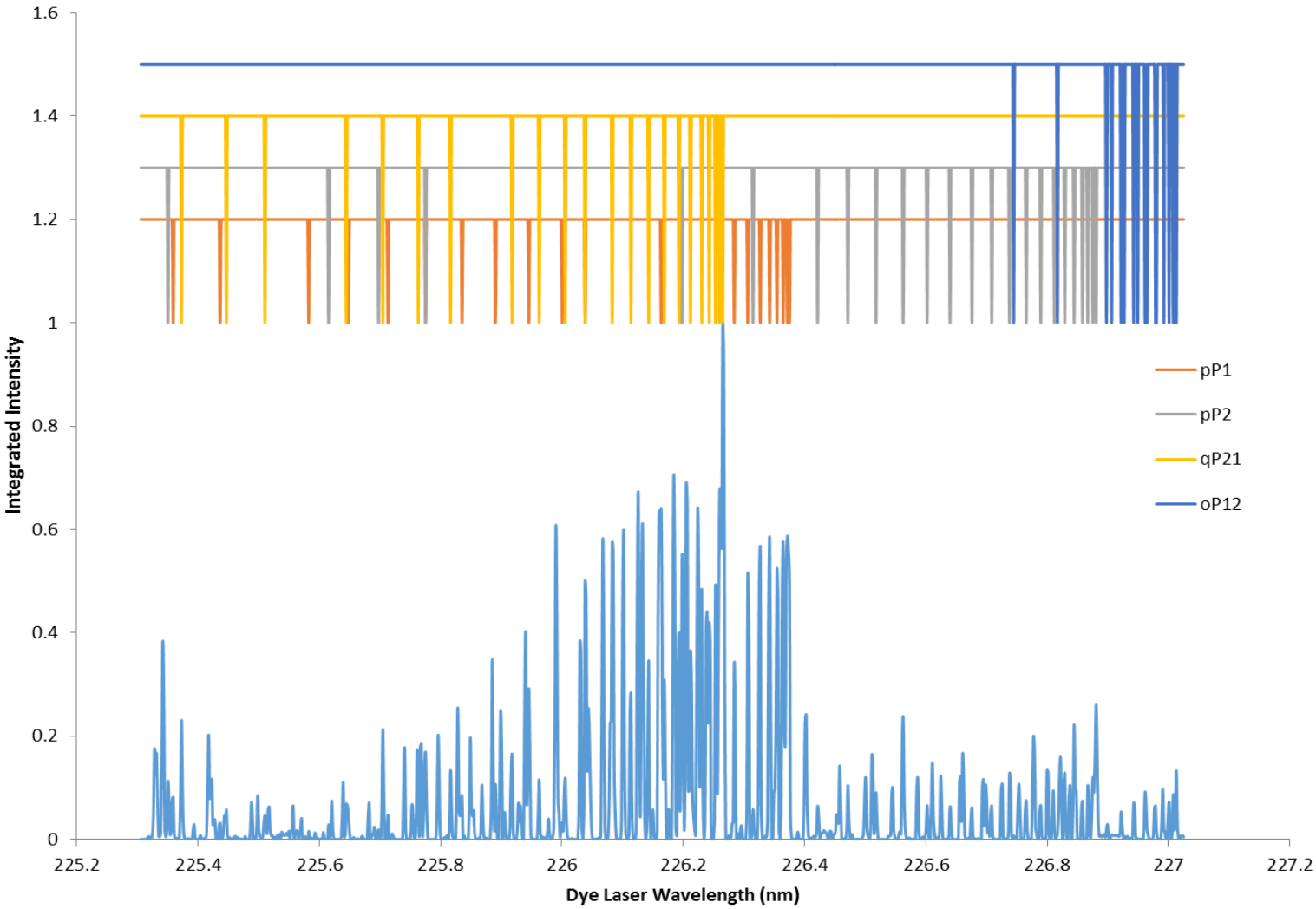

Figure 5.3: REMPI data of the NO fragment, 18 μs after dissociation. The vertical lines above the spectrum indicate the different P branch transitions.

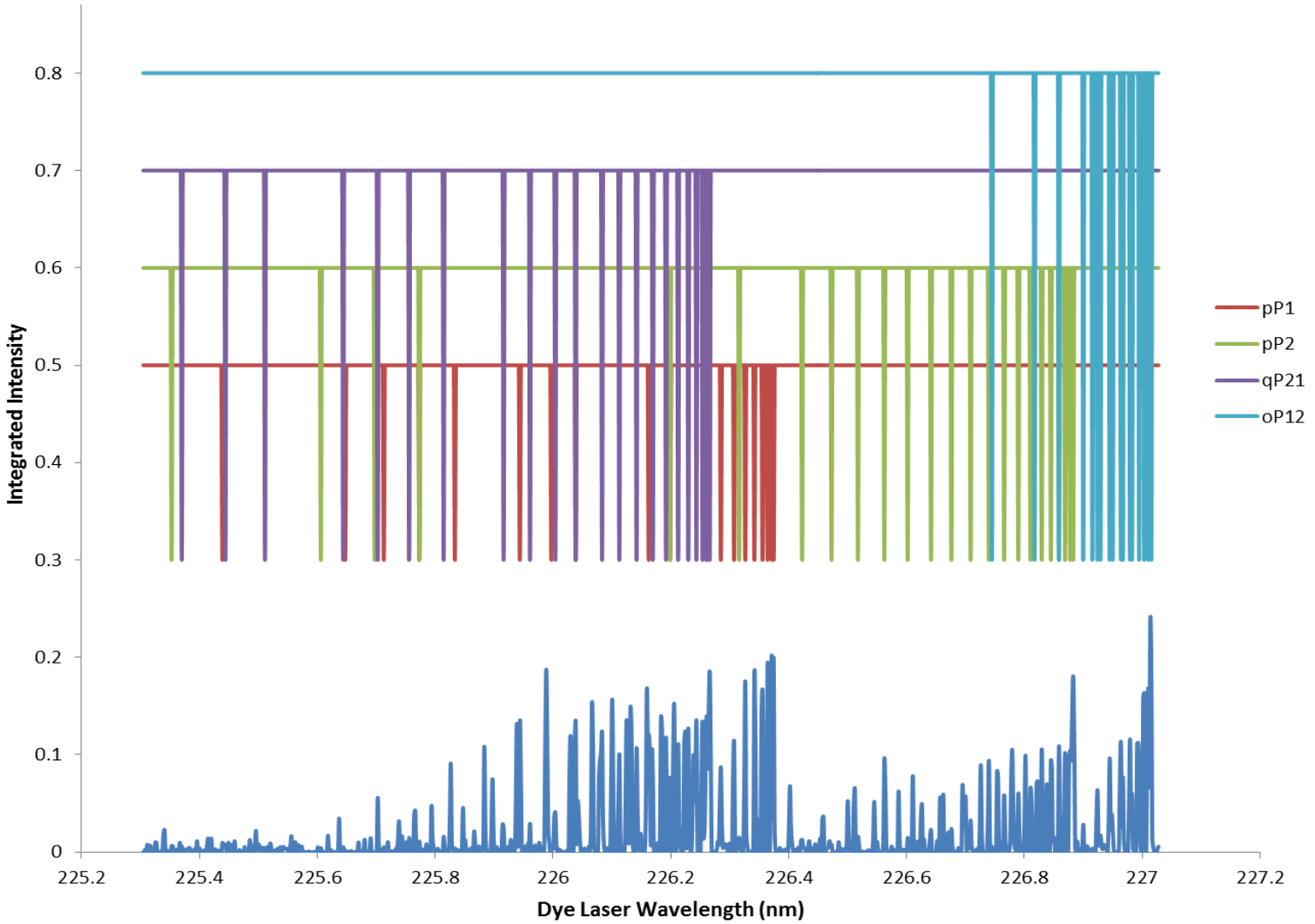

Figure 5.4: REMPI data of the NO fragment, 35 μs after dissociation. The vertical lines above the spectrum indicate the different P branch transitions.

5.1.3.2Q Branches

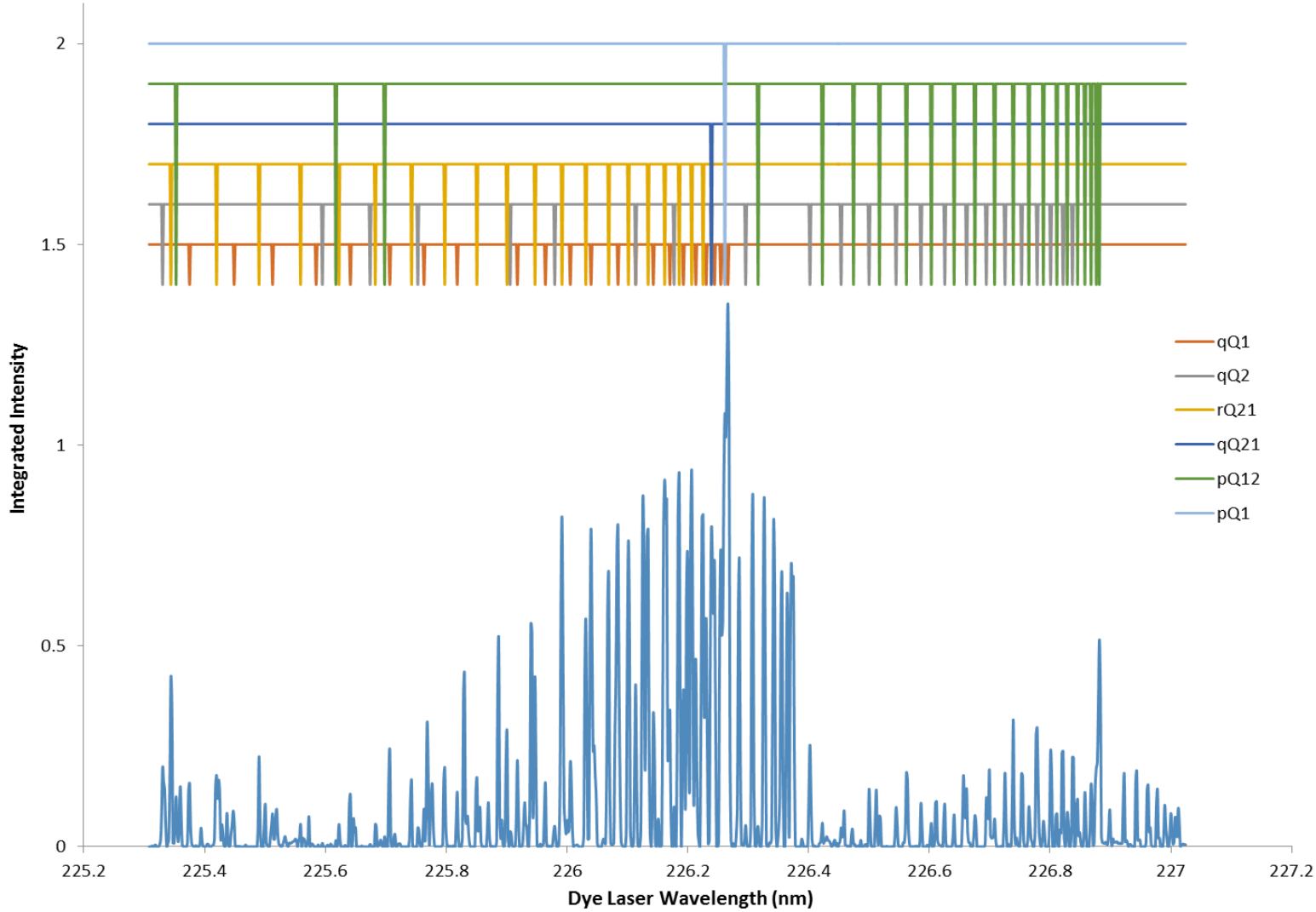

Figure 5.5: REMPI data of the NO fragment, 9 μs after dissociation. The vertical lines above the spectrum indicate the different Q branch transitions.

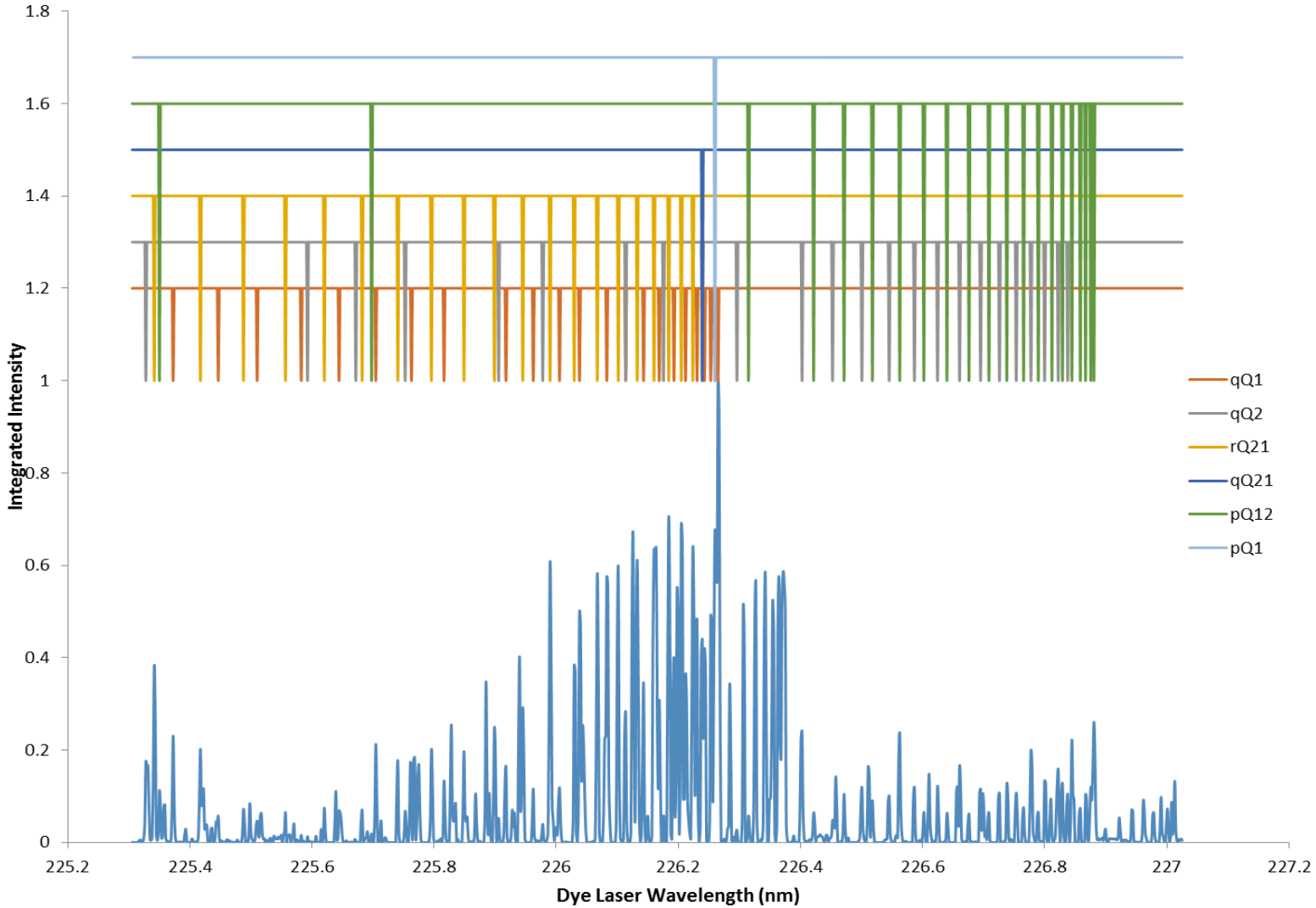

Figure 5.6: REMPI data of the NO fragment, 18 μs after dissociation. The vertical lines above the spectrum indicate the different Q branch transitions.

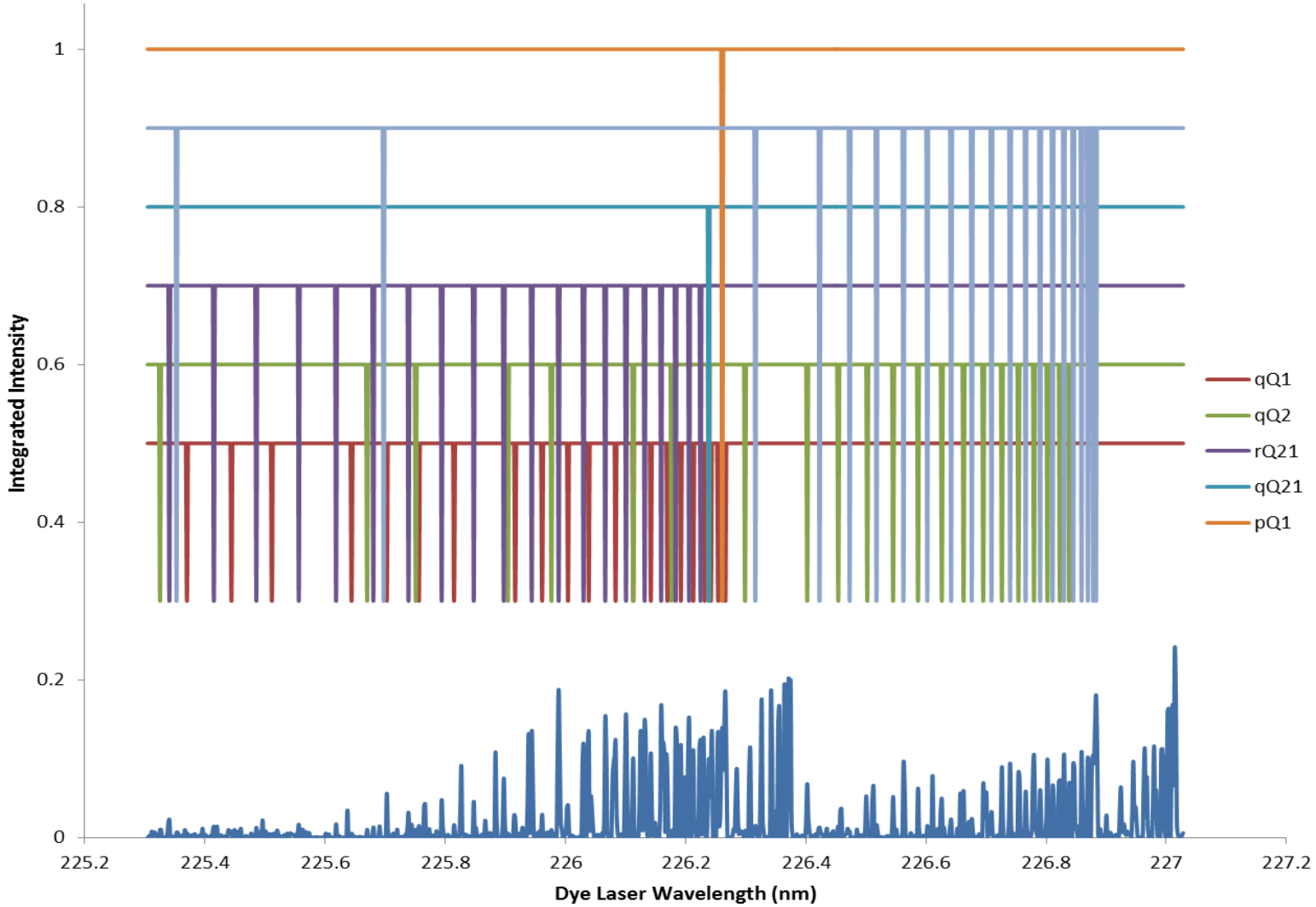

Figure 5.7: REMPI data of the NO fragment, 35 μs after dissociation. The vertical lines above the spectrum indicate the different Q branch transitions.

5.1.3.3 R Branches

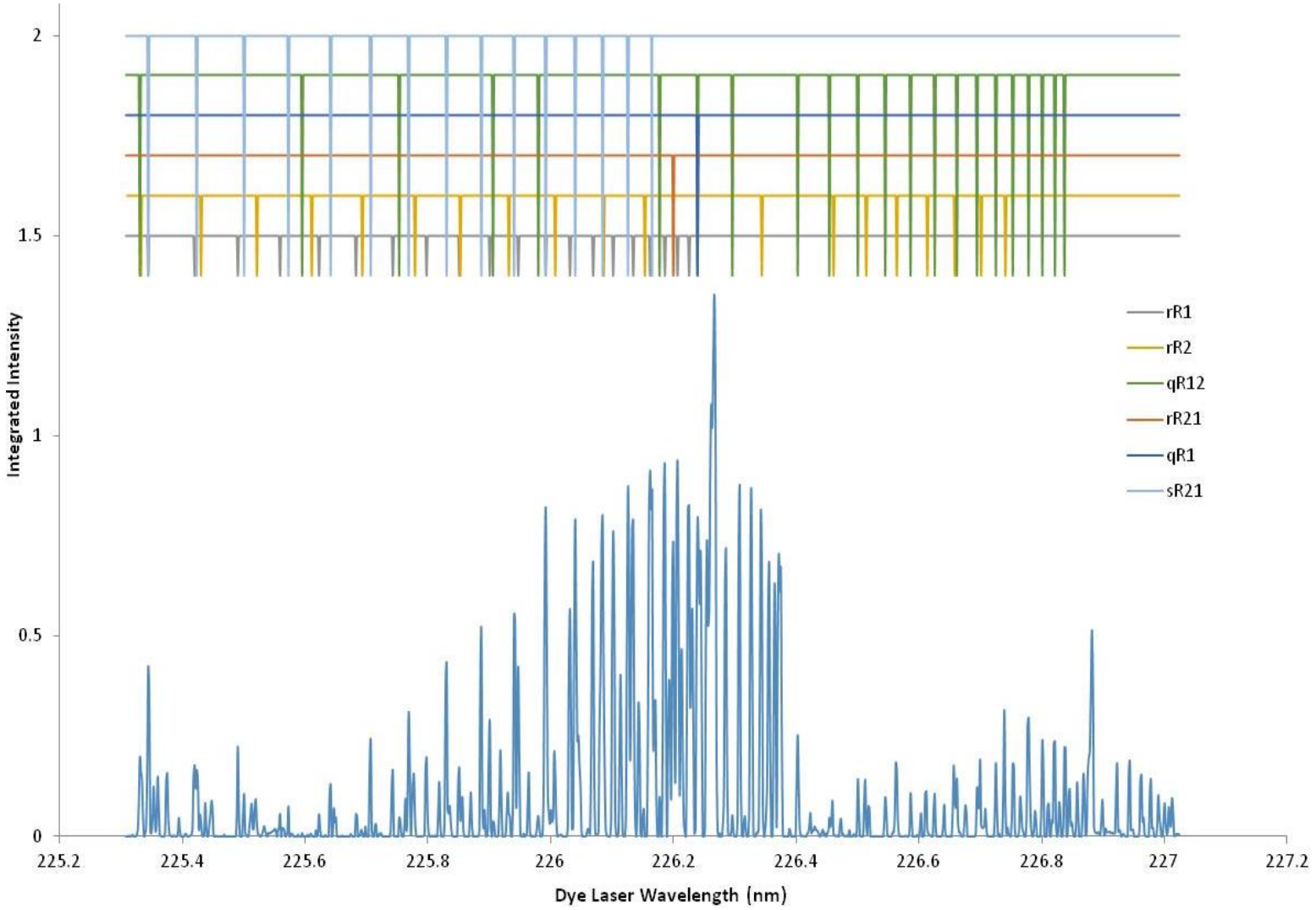

Figure 5.8: REMPI data of the NO fragment, 9 μs after dissociation. The vertical lines above the spectrum indicate the different R branch transitions.

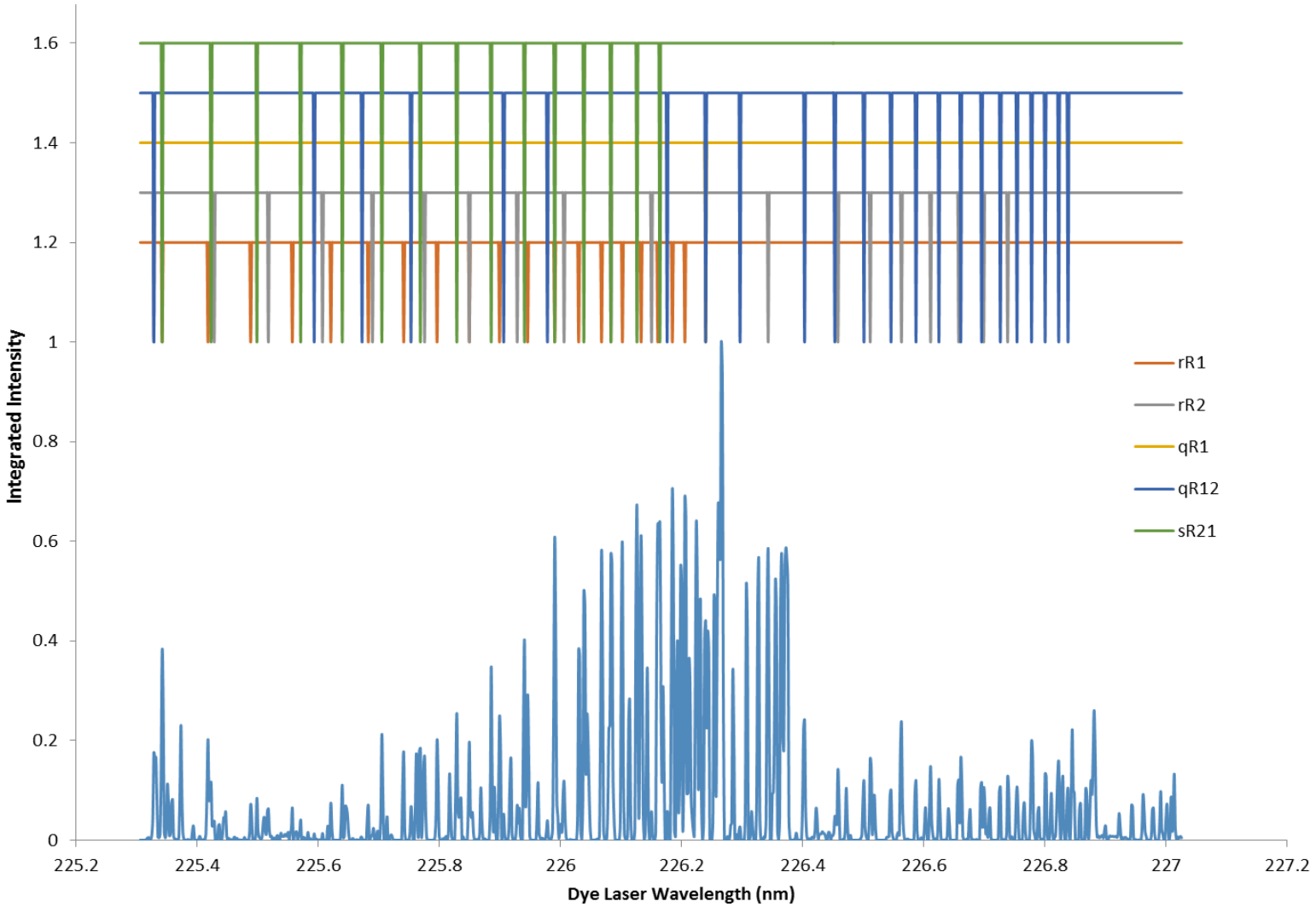

Figure 5.9: REMPI data of the NO fragment, 18 μs after dissociation. The vertical lines above the spectrum indicate the different R branch transitions.

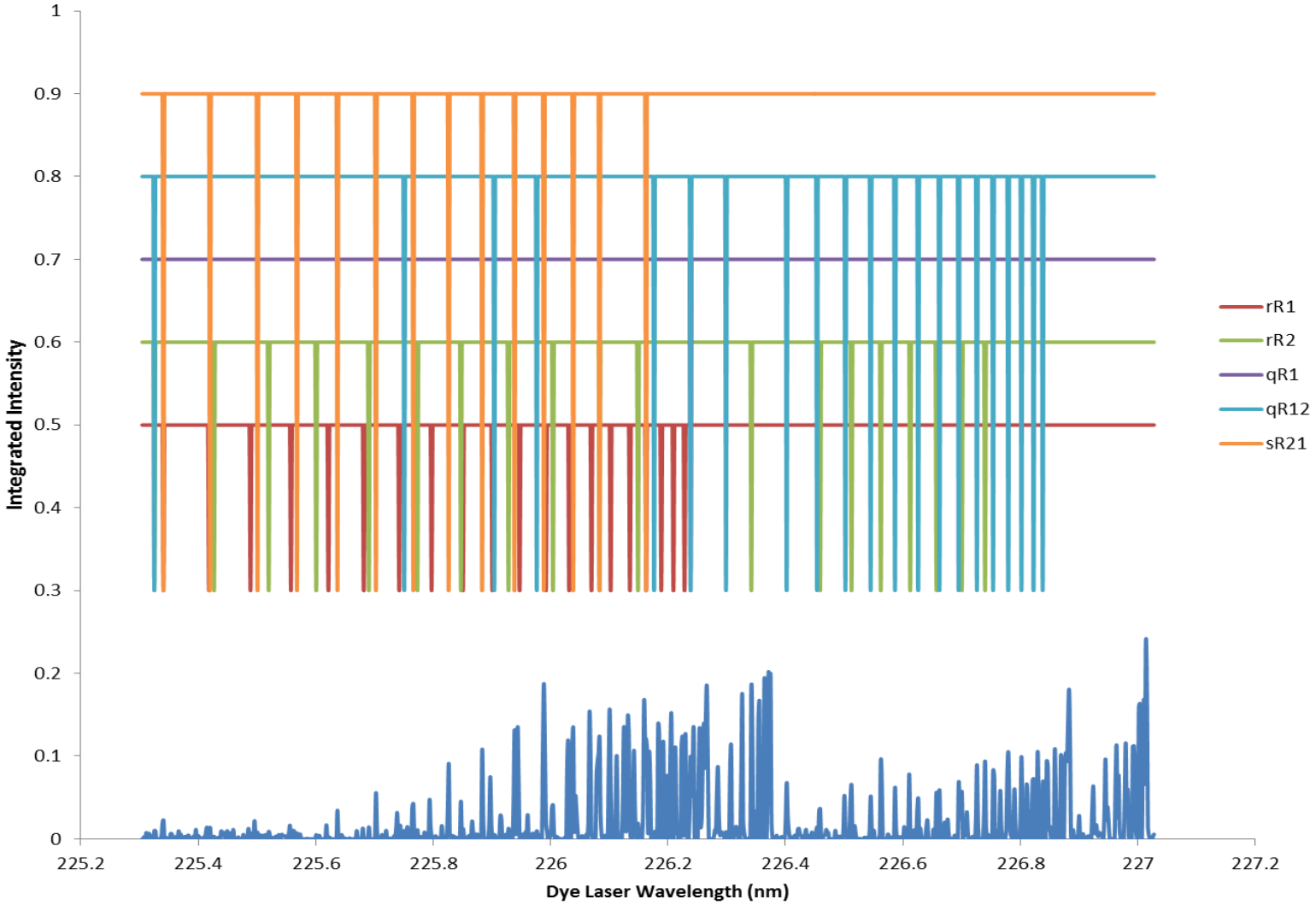

Figure 5.10: REMPI data of the NO fragment, 35 μs after dissociation. The vertical lines above the spectrum indicate the different R branch transitions.

It is easy to see that there are stark differences between the spectra at different time delays. This is best seen in the pP1 branch at 226.2 to 226.4 nm. At short 9 μs delay the peak intensity decreases with increasing wavelength, while the trend is reversed when the delay is 18 or 35 μs. A complication in interpreting these peaks is that the pP1 forms a bandhead and therefore reverses in this region. Many of the lines therefore correspond to transitions from two different rotational states in the same branch. For example, the peak at 226.285 nm is actually both J = 1.5 and J=16.5, and at 226.306 nm the J=2.5 and J=15.5 are both excited and so on. A similar trend occurs in the region above 227 nm, where we see the oP12 states. Again a complication occurs where several of the peaks are too close to be resolved with the dye laser. These peaks unfortunately must be removed when analyzing the rotational population of each J state due to the overlapped nature of the peaks; it is not possible to separate their components.

5.2 Maxwell-Boltzmann Distributions

The populations of the different rotational states of the two lowest energy spin-orbit states of the NO fragment have been calculated by dividing the integrated intensity by the respective Hönl-London factor, H_L - see Equation (5.1) and the rotational degeneracy. These factors are taken for each line in the REMPI spectrum as given by PGOPHER.[1] In a "Boltzmann plot" the logarithm of the population of each rotational state is given as a function of rotational energy. If the population is thermally distributed and governed by a single temperature, the logarithms of the populations fall on a straight line with a slope equal to $\frac{1}{k_B T}$, where k_B is the Boltzmann constant $1.38064852\times10^{-23}\ \frac{m^2 kg}{s^2 K}$ and T is

temperature in K. If multiple temperature distributions are present, the weighted rotational populations resemble a bi-exponential and can be approximated by the sum of two Boltzmann terms.

$$\frac{P}{H_L} = A\exp\left(\frac{E_{rot}}{k_B T_1}\right) + B\exp\left(\frac{E_{rot}}{k_B T_2}\right), \tag{5.1}$$

where P is the population of the state, and H_L is the Hönl-London factor for the given transition and adjusted for degeneracy of the rotational state. The pre-exponential factors A and B are the proportionality factors for each Boltzmann factor. A summary of the energy distributions is found in Table 5.1. Figure 5.11 shows the Boltzmann graphs for the transitions originating from the same spin-orbit state at the three different delay times.

Table 5.1: The rotational temperature profiles for the two components of the bi-exponential Equation (5.1) for the different ionization delays of each spin state. The upper and lower bounds represent the 99% confidence interval of the fit parameter which relates to the temperature. The relative fraction of the two components, high and low J is also listed.

Lower Spin State

Delay (μs)	First Component (K)	Lower Bound (K)	Upper Bound (K)	Second Component (K)	Lower Bound (K)	Upper Bound (K)	Relative Fractions A:B
9	190	140	250	-2030	170	-2540	93:7
18	150	120	200	1440	290	-460	89:11
35	150	90	1100	600	50	2030	99:1

Upper Spin State

Delay (μs)	First Component (K)	Lower Bound (K)	Upper Bound (K)	Second Component (K)	Lower Bound (K)	Upper Bound (K)	Relative Fractions A:B
9	77	62	110	730	320	-190.0	71:29
18	210	130	530	2200	220	-270.0	82:18
35	180	160	210	2700	41	-14	87:13

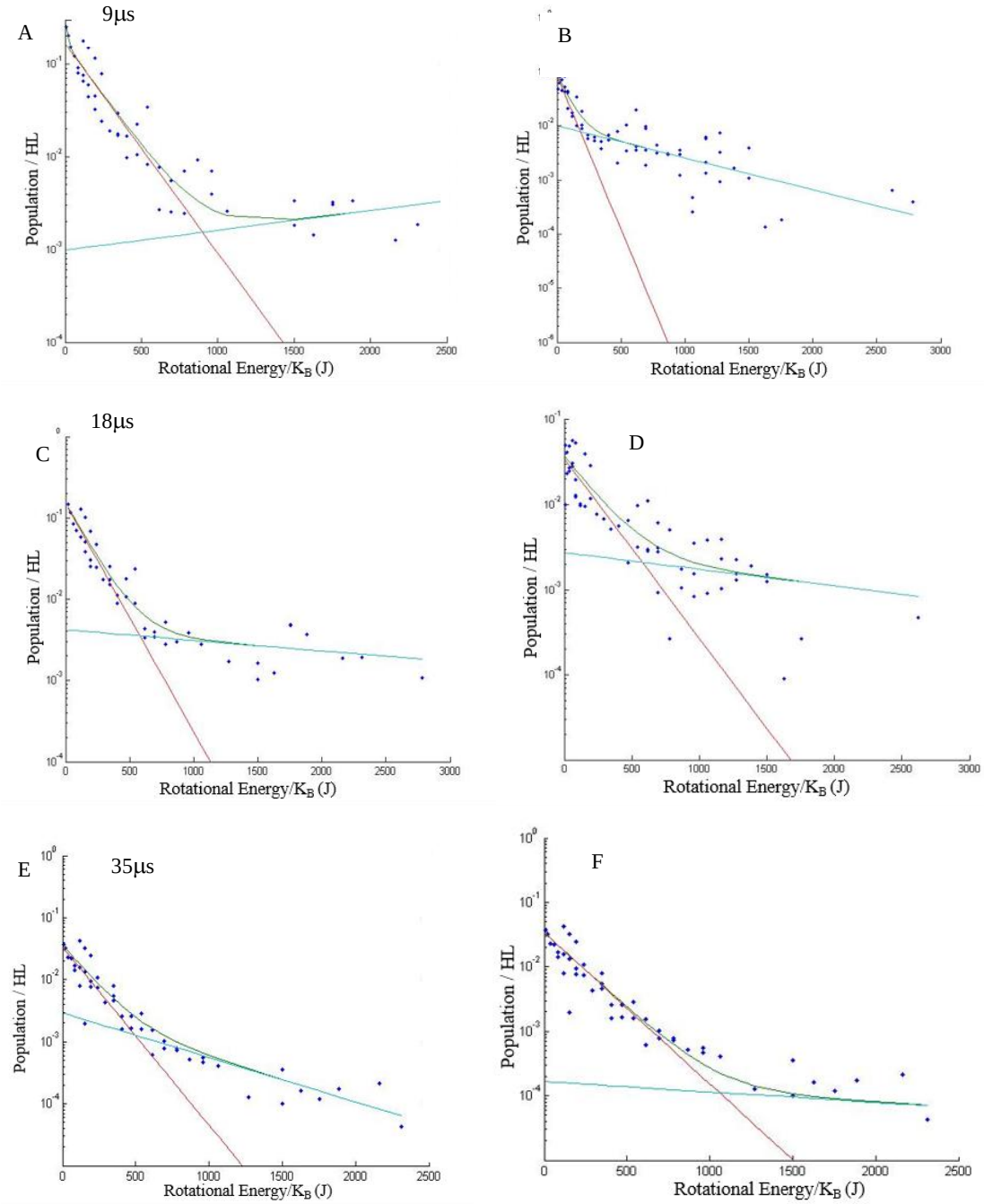

Figure 5.11: Boltzmann plots of the rotational state population as a function of rotational energy from the lower spin orbit state $^2\Pi_{1/2}$, (Left) and for the higher spin orbit state $^2\Pi_{3/2}$ for the three different delay times (Right). The green line is the best fit of the data (blue dots) to Equation (5.1). The red and teal lines are the two temperature components which form the bi-exponential. The temperature of the high temperature component decreases as the delay increases for the lower spin orbit state.

In all of the delay experiments and for both spin-states the data had to be fit to a bi-exponential function, where the "cold" component (i.e. low-*J*) is dominant. In the $^2\Pi_{1/2}$ state, at short delay times the "low-*J*" component is described by a temperature of around 190 K. The "high-*J*" component is quite interesting. At high rotational energy, it is non-thermal as evident by the "negative temperature". Even after restricting the fitting parameters to only give positive values the second component shows a non-thermally high temperature, while the first component shows little change. It is also clear that at longer delay times the temperature of both components decreases, although no experiments show complete thermalization to the matrix temperature of 20 K. While the upper spin state does exhibit biexponential behavior, it does not show the same trend as the lower state. The population generated after 9 μs delay shows a thermal distribution for both temperature components that is much cooler than either of the two longer delay times. In both spin states the "high-*J*" component appears to suffer from large non-thermal effects induced by the laser dissociation as evident by the negative temperatures and the very large gap between the upper and lower bounds. This effect is exacerbated by the low intensity of peaks at high rotational energy.

As expected the NO fragments contain more rotational energy when probed at short delay times, i.e. when they originate either from the surface (or near the surface) of the matrix. The NO fragments that arrive after 18 and 35 μs likely originate from deeper inside the matrix and have undergone many collisions with matrix Ar atoms to reduce their rotational temperature. We note that even at the longest delay times the distribution is far from thermal indicating that the Ar-matrix is not overly efficient in quenching rotational motion. In the $^2\Pi_{1/2}$ state at all delay times, the "low-*J*" component comprises 90 to 99% of the total

signal, while in the upper $^2\Pi_{3/2}$ state it forms roughly 70-90% of the signal. The two components indicate two separate processes occurring within the dissociation. It is likely that the "high-*J*" population is generated by photolysis of NO_2 at the surface of the argon; a limited number or collisions leads to a non-thermal distribution of energy. The "low-*J*" component is then from dissociation of NO_2 from within the matrix. Collisions with the matrix leads to thermalization of the rotational states of the NO fragment. At shorter time delay more of the signal is due to the "high-*J*" component, this suggests at short time delay more of the NO_2 molecules that dissociate near the surface are sampled than at longer delay – as might be expected.

The "high-*J*" component behavior compares well with previous gas phase studies in molecular beams at similar dissociation energies. Zacharias *et al.* found a temperature distribution for high *J* levels of >1000 K for dissociation at 351 nm and 337 nm, although their spectra were complicated by background NO.[2] When dissociating NO_2 in near threshold at from 393 to 347 nm Kawasaki *et al.* found the NO rotational distributions for high *J* levels to fit at 1300 K.[3] Interestingly, these studies also show a bimodal temperature distribution, with the "low-*J*" features having a distribution of close to 300 K. It is important to stress however, that in these studies the "high-*J*" component dominates the spectra, whereas in our work the opposite is true. Reisler and coworkers attempted to model the rotational distribution using a statistical model using Phase Space Theory (PST), while this method works well at low dissociation energy it did not reproduce the data well from dissociation at 355 nm.[4] Reid and Reisler proposed that the two distributions were caused by the overlapping ($X\ ^2A_1/A\ ^2B_2$) of states.[5] We note that there are substantial differences in the "low-*J*" distributions between the gas phase dissociation, and the

condensed phase work: in the present work the temperature of the low-J population corresponds to only about 100-200K and a very large fraction of NO photofragments (70-99%) are found in these low rotational states. In the gas phase a much smaller fraction is formed at low rotational temperature and this temperature is much higher – at least 300 K. This illustrates a different mechanism, i.e. a dissipation of rotational energy in the matrix prior to desorption, which is unique to condensed phase dissociation. The independent works by Zacharias,[2] Kawasaki,[3] and Reid[4] in the gas phase at 355 nm do not show inverted rotational state populations of the NO fragment which we observe after 9 ms delay in the "high-*J*" component as reported in Table 5.1 (-2030 K). All of the researchers do, however, find that the rotational energy distributions are non-thermal, with rotational temperatures ranging from 1000-1300 K, which corresponds well with our results of 1440 K at 18 ms and our inverted distribution at 9 ms. These findings support that at short time delay the NO fragment rotational energy distribution is similar to that seen in gas phase. At longer time delays the NO fragments do not exhibit similar rotational distributions as the rotational states populations are cooled to temperatures closer to 100-200 K. These colder fragments were not observed in the gas phase experiments, presumably because in gas phase experiments collisional cooling is negligible, while collisional quenching is a dominant process following NO_2 photodissociation inside an Ar-matrix.

5.2.1 Translational Energy Distribution

As dissociation and ionization occur at fixed locations during the course of an experiment, it is possible to monitor the translational energy distribution along the time of flight axis, if the distance between the two locations is known. Since REMP-ionization is state-selective, the translational energy distribution can be determined for each rotational state

by monitoring the ion intensity as a function of time delay between ionization and dissociation.

5.2.1.1 Determination of the Dissociation-Ionization Distance

The intensity of the REMPI signal obtained for a selected rotational state is obtained as a function of the time delay between the photolysis and REMPI laser pulses (see Section 2.4.2.2). The time delay data is fit to a flux-weighted Maxwell-Boltzmann distribution (Equation 5.2), the pre-exponential factor accounts for the fact that the fragments originate from a flat circular area much larger than the ionization region. This has been used for similar experiments in the past and is explained in more detail in references.[6, 7]

$$S_{MB}(t,r,T) = r^3 t^{-4} \exp\left[\frac{-mr^2}{2k_B T t^2}\right] \tag{5.2}$$

Equation (5.2) gives the flux weighted Maxwell Boltzmann distribution, where *r* is the distance between the dissociation and ionization and *t* is the time it takes for the fragments to travel between these two points. When multiple distributions are present, the total signal can be fit by a sum of two or more flux-weighted distributions, as seen in Equation (5.3).

$$S(a_i,r,t,T_i) = a_1 S_{MB}(t,r,T_1) + a_2 S_{MB}(t,r,T_2) + \ldots \tag{5.3}$$

It is clear that the distance between the dissociation and ionization plays an important role in determining the energy distribution. The dissociation site is at a fixed location (the end of the cold finger). However, the ionization region can be moved through the use of a prism mounted onto a two-point pivoting base, which is controlled by micrometer screws. It is not easy to measure the distance between the two points directly, since they are inside the

vacuum chamber. Therefore, the location of the ionization beam at a distance of about 3.8 meters outside the chamber is recorded for each arrival time experiment. The time of maximum intensity of each time-delay experiment is recorded and the beam is then translated. The new projection location is again recorded along with the time delay data. The distance between the two projection points, d*x*, is easily measured. As the distance between the prism and the ionization region, *D*, is known, the distance between the two ionization regions, *dr*, can be readily calculated. The difference in the time delay which corresponds to the maximum ion intensity, t_{max}, is dependent only on the distance *r*, when all other variables are held constant. Thus the difference in t_{max} between the two ionization locations can be used to calculate the distance between the dissociation laser and the ionization region. (Figure 5.12)

$$
\begin{aligned}
t_{1_{max}} / r_{1_{max}} &= t_{2_{max}} / r_{2_{max}} \\
r_{2_{max}} &= r_{1_{max}} + dr \\
t_{1_{max}} / r_{1_{max}} &= t_{2_{max}} / (r_1 + dr) \\
t_{1_{max}} / t_{2_{max}} &= r_1 / (r_1 + dr) \\
r_1 &= \frac{(t_{1_{max}} / t_{2_{max}})dr}{1-(t_{1_{max}} / t_{2_{max}})}
\end{aligned}
\tag{5.4}
$$

As t_{1max} (9.5 μs), t_{2max}(19.0 μs), *D* (3814 mm) and *x* (27 mm) are all known, solving for *dr* yields 3.4 mm. Solving for r_1 using the last line in Equation 5.4 the distance between the dissociation and ionization regions is 3.392 mm or 3.4 mm as well. For all experiments care was taken to ensure that the distance was held constant and known.

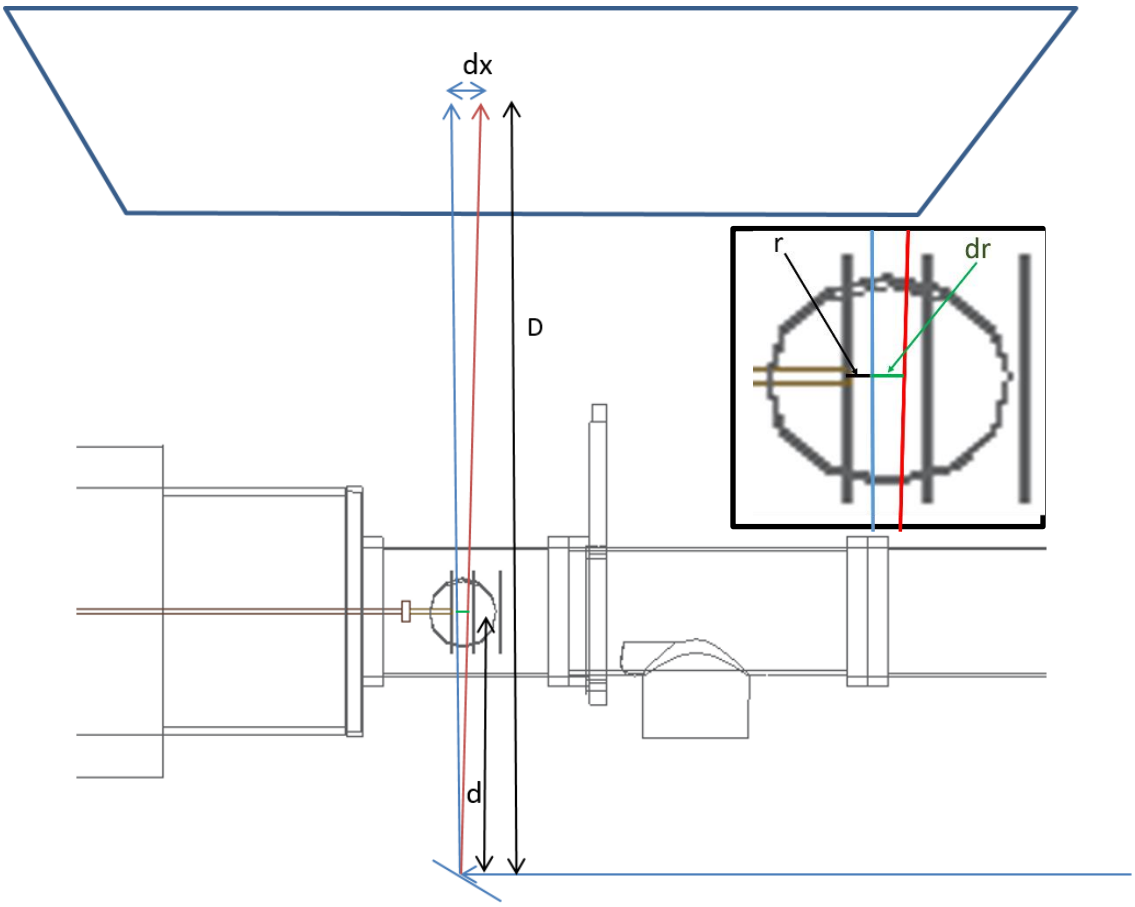

Figure 5.12: Diagram of the distances needed to calculate the distance between the dissociation region and the ionization region. The inset shows an enlarged region of the electrodes to indicate the distances between the two ionization regions in the separate experiments, *dr*, and the distance between dissociation and ionization, *r*. Using the calculation in Equation 5.4 we found that r = 3.3 mm and was held constant for all reported data.

5.2.1.2 Arrival time measurements

The transit times between the photolysis laser pulse in the matrix and REMPI laser pulse were measured for selected rotational states. These time delay plots for several of the pP1, rR1 and oP12 branches are shown in Figures 5.13 and 5.14, and are summarized in Table 5.2a-c. Figures 5.15 and 5.16 show the average translation temperature recorded for the different J values.

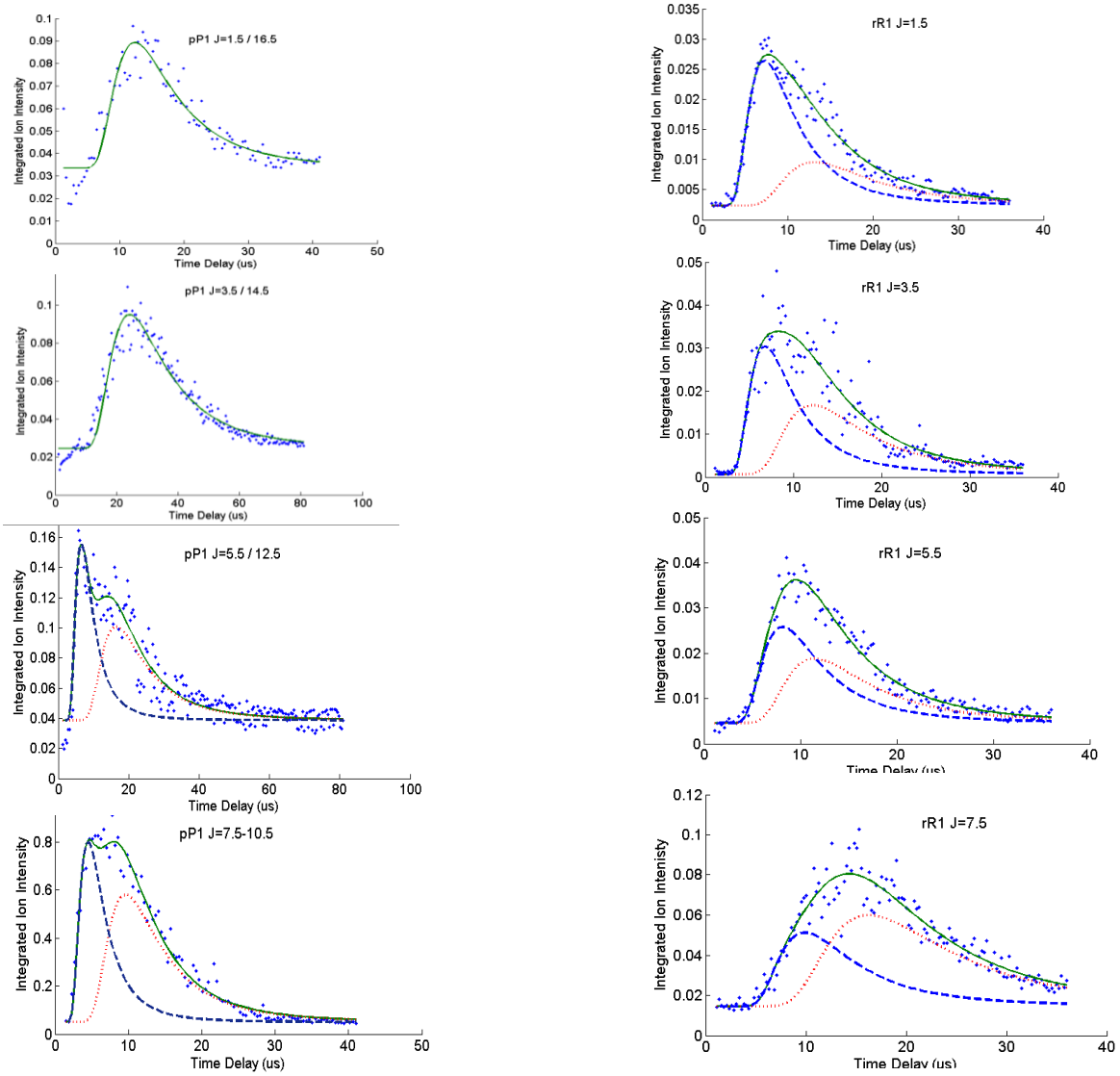

Figure 5.13: Time delay plots for several peaks of the pP1 branch and rR1 branch (blue dots) along with the fit to the Boltzmann expression of Equation (5.2) (green line). When two temperature profiles are needed to describe the overall trend the sum of the two Boltzmann profiles, Equation (5.3), is shown in green and the individual fits are shown in the blue and red hashed lines.

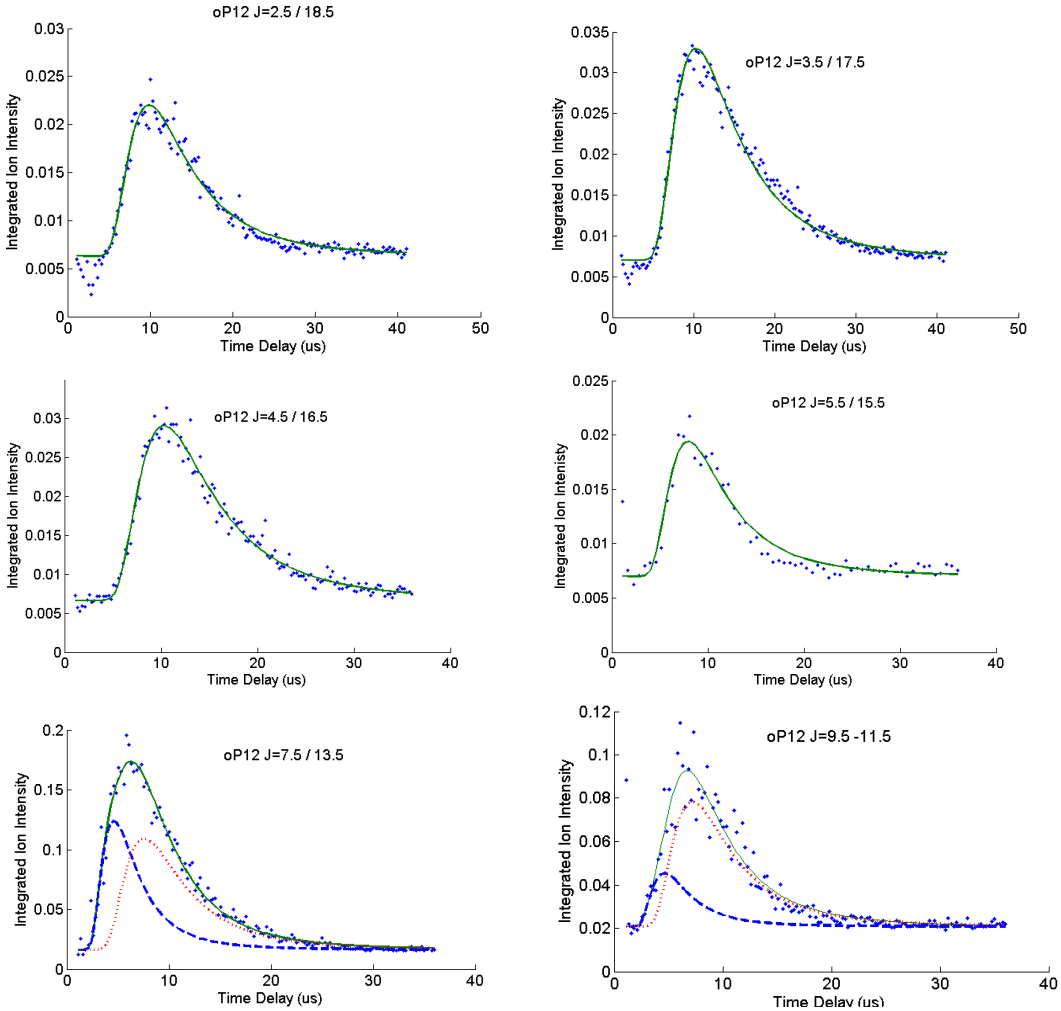

Figure 5.14: Time delay plots for the oP12 branch originating from the $^2\Pi_{3/2}$ state. This state exhibits similar behavior to the pP1 branch. For low rotational states only one temperature distribution is seen, while for high rotational states values a second temperature profile is observed.

Table 5.2: Average translational temperatures and standard deviation for different rotational states that form the pP1, rR1 and oP12 branches. Multiple J values indicate that the two peaks overlap in the REMPI spectrum. For peaks which have multiple temperature components both a low temperature and a high temperature component is shown.

J Value pP1 Branch	Average Translational Temperature (K)	J Value rR1 Branch	Average Translational Temperature	J Value oP12 Branch	Average translational Temperature (K)
1.5/16.5	27 (5)	1.5 (Low T Component)	54 (5.5)	2.5/18.5	57.9 (0.6)
2.5/15.5	59 (18)	1.5 (High T Component)	156.8 (7.9)	3.5/17.5	58.4 (7.5)
3.5/14.5	34 (12)	2.5 (Low T Component)	27.2 (6.8)	4.5/16.5	57.6 (6.7)
4.5/13.5 (Low T Component)	37 (13)	2.5 (High T Component)	91.7 (5.3)	5.5/15.5 (Low T Component)	55.3 (2.3)
4.5/13.5 (High T Component)	144 (32)	3.5 (Low T Component)	58.5 (3.6)	5.5/15.5 (High T Component)	231.7 (0)
5.5/12.5 (Low T Component)	18.1	3.5 (High T Component)	158.6 (17.8)	6.5/14.5 (Low T Component)	76.3 (25.3)
5.5/12.5 (High T Component)	96.3	4.5 (Low T Component)	43.6 (6.5)	6.5/14.5 (High T Component)	97.2 (23.3)
6.5/11.5 (Low T Component)	15.3	4.5 (High T Component)	133.2 (17.8)	7.5/13.5 (Low T Component)	66.1 (2.4)
6.5/11.5 (High T Component)	94.7	5.5 (Low T Component)	60.3 (1.9)	7.5/13.5 (High T Component))	214.9 (33.9)
7.5-10.5 (Low T Component)	20.1	5.5 (High T Component)	129.8 (7.3)	8.5/12.5 (Low T Component)	66.1 (2.5)
7.5-10.5 (High T Component)	89.1	6.5 (Low T Component)	59.3 (29.6)	8.5/12.5 (High T Component)	194.6 (24.2)
		6.5 (High T Component)	119.4 (17.7)	9.5-11.5 (High T Component)	73.8 (3.2)
		7.5 (Low T Component)	32.6 (1.9)	9.5-11.5 (High T Component)	208 (33.3)
		7.5 (High T Component)	83.1 (4)		
		8.5 (Low T Component)	25.2 (5)		
		8.5 (High T Component)	170.5 (32.5)		
		9.5 (Low T Component)	17.4 (12.4)		
		9.5 (High T Component)	207.2 (29.4)		
		10.5	110.3 (4.3)		

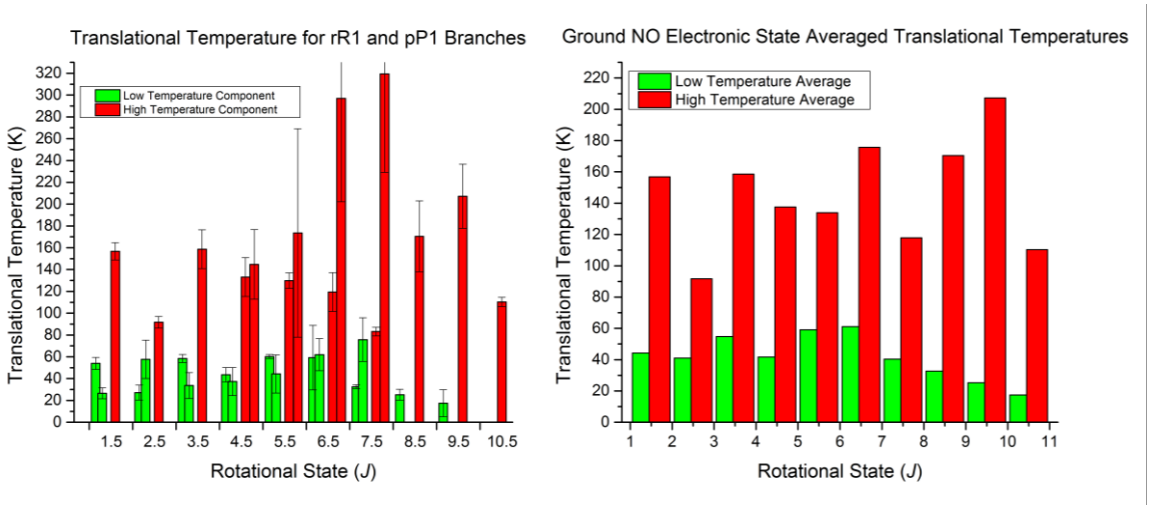

Figure 5.15: Left, Average translational temperature for the different rotational states which form the rR1 branch (left green and left red bars) and the pP1 branch (right green and right red bars). Both branches are dominated by two thermal distributions, one at low temperatures (green) which is slightly warmer than the bulk argon matrix and one at higher temperature (red). It is important to note that the pP1 branch rotational lines are overlaped with lines having higher rotational ground state. Error bars represent one standard deviation. Right, weighted averages of the two branches for each rotational state, both low and high temperature distributions are approximately constant at 30-50K and 100-180K respectively.

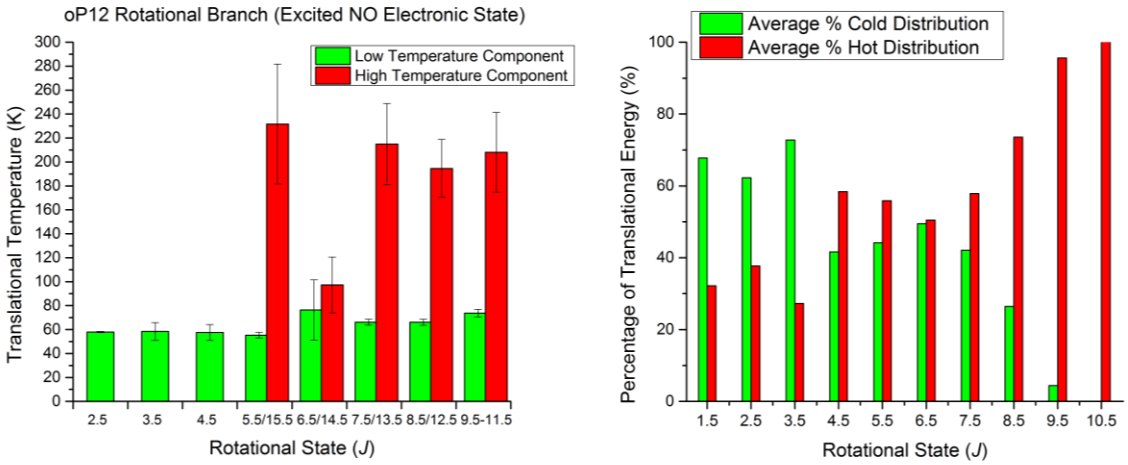

Figure 5.16: Left, average translational temperature for the different rotational states which form the oP12 branch. Similar to the other two systems, two temperature profiles are present at similar temperatures that of the lower NO spin state. Error bars represent one standard deviation of three trials. Right, average percentage of contribution of total signal of each temperature for J states for the rR1 and pP1 branches.

The translational temperature distributions (Fig 5.15 and 5.16) show several interesting features. From the time-delay plots for both the pP1 and rR1 branches (Figure 5.13a and Figure 5.14a) it is easy to see that the ion intensity profile is described by more than one translational temperature for several of the J values. In both the P and R branch the low

temperature feature is around 30-50 K, slightly warmer than the matrix temperature of 20 K. The ratio of low temperature component to high temperature shows large variation between rotational states, it is approximately 20-30% for fragments with high rotational energy. It increases up to 70% for fragments with low rotational energy. The low-temperature features may be attributed to NO_2 fragmentation occurring within the argon matrix. These NO molecules collide with the matrix, transferring translational and some rotational energy into the matrix. This not only slows the molecules down, but also thermalizes the rotational energy with to the matrix to a certain degree. As argon does not interact to a large amount with the fragments, the transfer of rotational energy is somewhat limited. Loss of rotational energy of these fragments results in the low temperature distribution being dominated by fragments with low rotational states. The high temperature case ranges roughly from 100K to 220K in both the R and P branch. The large uncertainties on the high temperature data make it difficult to identify a trend, but it appears that at higher rotational states of NO their translational temperature also increases. The high temperature features are caused by fragmentation of the NO_2 molecules near the surface of the argon matrix. These fragments undergo minimal collisions with the matrix. They retain most of their velocity and translational energy distribution that was imbued on them from the laser dissociation. These fragments undergo some collisions with the matrix which does cool them translationally, to a certain extent, but not nearly as much as the case in the low temperature profiles. Differences between the R and P branches are likely caused due to the fact that many of the pP1 lines for different *J* values overlap and thus the temperature distributions are the average of the overlapping states. Unfortunately, in the upper spin-orbit $^2\Pi_{3/2}$ state only the oP12 branch has enough intensity that time delay plots could be

analysed in a meaningful way. This branch exhibits similar behavior to the pP1, i.e. at high values of *J* two temperatures are present, while at low *J* values the lower temperature is dominant. The rR1 data shows that even at low *J* two temperature profiles are present.

The partitioning between the two NO spin orbit states can be estimate by analyzing the REMPI spectra and summing the total ion signal over each spin orbit state. This yields a ratio of 3:1 at short delay times, similar to that of the gas phase findings and closer to 1:1 at long delay times.

5.3 Quenching of Rotational and Translational Energy

The translational energy distributions of the NO photofragments along with the spectroscopic constants ω_e, $\omega_e x_e$, B_e, D_e, and the atomic energies of the oxygen fragment—obtained from NIST [8] can be used to estimate the energy that has been absorbed by the ice matrix following photolysis of NO_2.

$$\begin{aligned} h\nu &= D_o + E_{ex}(total) \\ E_{ex}(total) &= E_k(NO) + E_{in}(NO) + E_k(O) + E_{in}(O) \\ E_{ex}(total) - E_{in}(O) &= 3054,\ 2896,\ 2827\ cm^{-1} \end{aligned} \tag{5.5}$$

Here $h\nu$ at 355 nm is the photon energy used in dissociation (28182.5 cm^{-1}), D_o is the dissociation energy of NO_2 (25128.6 cm^{-1}),[9] and E_{ex} *(total)* is the total excess energy of both fragments which is dependent on the spin-state of the oxygen fragment formed. The E_{in} terms are the internal energies of the oxygen and NO fragments. For the oxygen fragment this is the electronic energy, and for NO it is the sum of the rotational, vibrational and electronic energies. The final line in Equation (5.5) represents the excess energy left depending on which oxygen spin state is formed, $^3P_2$, $^3P_1$, $^3P_0$ respectively. The term

$E_{ex}(total)$-$E_{in}(O)$ corresponds to the sum of the kinetic energies of the oxygen atom and NO fragments as well as the internal energy of the NO fragment.

The kinetic energy of the oxygen fragment can be estimated by conservation of momentum, such that the remaining energy describes the rotational, vibrational electronic and translational energy of the NO fragment. This is a very rough estimate and one might reasonably argue that – especially for translationally cold photofragments - the translational temperature of both photofragments following the quenching process should be identical instead of the momentum.

For the $^3P_2$ oxygen co-fragment this is described by

$$\begin{aligned} E_{ex}\left(total\right) - E_{in}(O_{^3P_2}) &= 3054\ cm^{-1} \\ E_{ex}\left(total\right) &= E_k(NO) + E_{elec}(NO) + E_{\text{int}}(NO) + E_k(O) + E_{ele}(O) \end{aligned} \tag{5.6}$$

The electronic energies of O-atoms are either 0 cm^{-1} ($^3P_2$), 158.265 cm^{-1} ($^3P_1$) or 226.977 cm^{-1} ($^3P_0$). The excited spin orbit state of NO is the $^2\Pi_{3/2}$ state lies 119 cm^{-1} above the ground state. The kinetic energies of NO and O are assumed to be related through conservation of momentum $m_{NO}\mathrm{v}_{NO} = m_O\mathrm{v}_O$. (see above)

$$\begin{aligned} E_k(O) + E_k(NO) &= \frac{1}{2} m_O \mathrm{v}_O{}^2 + \frac{1}{2} m_{NO} \mathrm{v}_{NO}{}^2 \\ &= \frac{1}{2} m_O \left(\frac{m_{NO}\mathrm{v}_{NO}}{m_O} \right)^2 + \frac{1}{2} m_{NO} \mathrm{v}_{NO}{}^2 \\ &= \frac{1}{2} m_{NO} \mathrm{v}_{NO}{}^2 \left(1 + \frac{m_{NO}}{m_O} \right) \end{aligned} \tag{5.7}$$

Equation (5.6) now becomes:

$$3054\ cm^{-1} = E_k\left(NO\right)\left(1+\frac{m_{NO}}{m_O}\right)+E_{in}\left(NO\right) \tag{5.8}$$

Equation (5.8) yields the total energy released in terms of the measured kinetic and rotational energies of the NO fragment. The same calculation can be done for the other oxygen electronic states, yielding values of 2895.63, and 2826.9 cm^{-1} for the sum of internal and kinetic energy of the fragments. The values given above are for the $^2\Pi_{1/2}$ NO fragment. The $^2\Pi_{3/2}$ state lies 119.84 cm^{-1} higher and thus the total E_{ex}*(total)* will be lower by the same amount.

Since we only detect NO in its vibrational ground state (v=0) the internal energy of the NO fragment is simply

$$E_{in}(NO) = E_{rot} = BJ(J+1) - D_e J^2(J+1)^2 \tag{5.9}$$

and E_{in} can be calculated for each value of J. Using (5.9) and the data from the translational energy distributions obtained from the time delay plots, the total energy of the NO fragment can be calculated. Any difference between the total energy imparted on the system and the energies of the O and NO fragments is given to the matrix. Because the translational energy of the oxygen fragment is not measured we can only determine the amount of quenching for the NO fragment. If we assume that the oxygen fragment is quenched in the same way as the NO fragment we can determine approximate the amount of quenching into the matrix. Figure 5.17 illustrate the energy quenching for the two temperature profiles for each of the three rotational branches investigated. The amount of quenching occurring within the matrix seems to vary greatly, supporting the notion that excitation of NO_2 molecules occurs over a range of depths within the argon matrix. When both average

rotational and translational energies are low, a large amount of energy is deposited into the matrix through collisions, whereas near surface molecules undergo little energy transfer and thus little quenching.

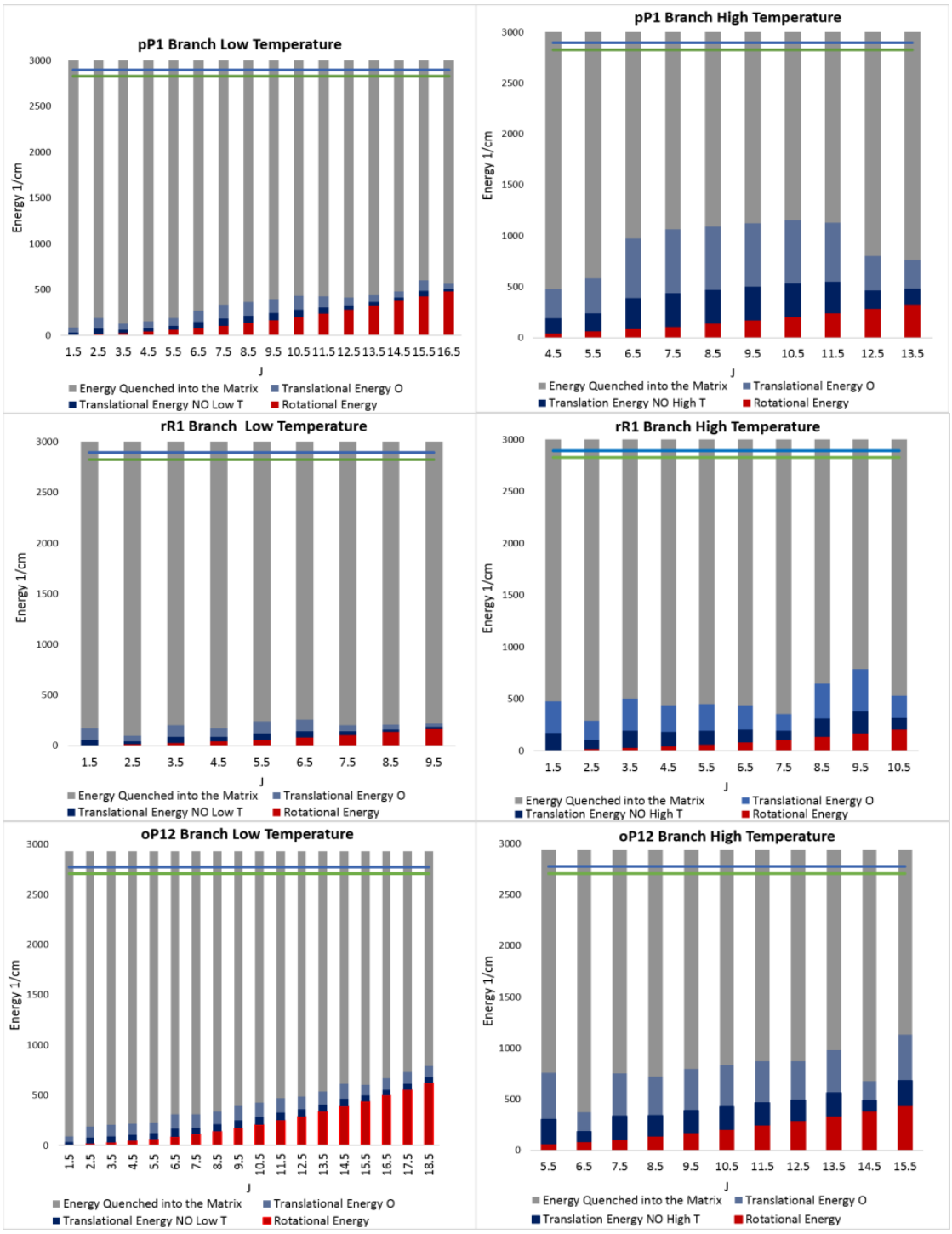

Figure 5.17: Energy partitioning for the high and low translational temperatures for the three branches. Grey bars indicate the amount of energy that is deposited into the matrix for that particular rotational state of NO. Faded blue bars indicate the translational energy of the oxygen fragment assuming the oxygen fragment is quenched in a similar fashion to that of the NO fragment. Dark blue, illustrate the amount of average translational energy for the NO fragment. Finally, the red bars indicate the amount of rotational energy. The blue and green horizontal lines represent the maximum available energies if the oxygen $^3P_1$ or $^3P_2$ spin states are formed respectively. If there was no population in a given rotational state at that translational temperature it has been omitted.

5.4 Discussion

The REMPI spectra illustrate this apparatus' ability to generate high resolution state specific rotational populations of fragmented molecules. The time-delay data illustrate this machine's ability to investigate translational energy distributions as well. Vibrational distributions while not investigated in this work could be easily obtained, if the appropriate REMPI transitions are accessible, by integrating the total rotational ion intensity for each vibrational state.

The rotational population distributions of NO fragments resulting from dissociation within an argon matrix have two components, a "low-*J*" component with temperatures between 100 and 200K and a highly excited "high-*J*" component with temperatures which range from >1000K to a non-thermal distribution. The "low-*J*" component accounts for the majority of the ion signal up to 99% at long delay times between dissociation and ionization. By comparison, Yabushita et. al found that when NO_2 was deposited onto a solid gold or an amorphous water ice sample where conversion to N_2O_4 is highly likely, a thermal distribution was sufficient to describe the population (see also Chapter 4).[10] By contrast in the present study we find that for the low-temperature rotational distribution the rotational temperature falls between that of NO formed on a gold surface and that the rotational temperature of NO from photolysis of NO_2 and N_2O_4 on water ice (T=175 K). The authors do not attempt to assign a rotational temperature to the NO fragments from the gold surface, it is however, evident from the REMPI spectrum that it is highly excited. This is the first REMPI/Translational Energy study that the author is aware of in which the NO_2 molecules are doped into an inert gas matrix and dimerization is sufficiently suppressed, thereby simulating environmental conditions when NO_2 is gradually deposited into ice

from air. In previous gas phase studies [2, 3] a bimodal distribution of rotational states has also been found, however, the minor low-temperature component (at T=250K) has likely been formed through a different mechanism, as the ratio of "low-J" vs. "high-*J*" are drastically different and the rotational temperature in the present experiment is much lower. Translational energy distributions and quenching data are also bimodal with two distinct thermal distributions, one at a low temperature close to the temperature of the matrix and a higher temperature distribution. In combination with the bimodal rotational distribution this is highly suggestive of a two-step process where NO_2 is dissociated in the matrix and undergoes many collisions which quench the translational and rotational degrees of freedom simultaneously whereas those NO photofragments formed near the surface undergo few collisions and remain largely unquenched. As argon is an atomic gas/solid it has limited ability to quench the rotational energy of the NO fragment and, as a result, low and high rotational states can be found in both the high and low translational temperature distributions. We note nevertheless that the fraction of low rotational states is higher in the slow NO photofragments (Figure 5.16) and *vice versa*. Yabushita et al. recorded the NO translational distribution following photolysis of NO_2 in water ice. They also found a bimodal distribution and found a ratio of 99 (cold)-1(hot) in population of the two temperature profiles at 351 nm. This is consistent with our findings at low rotational energy, the difference for fragments at high rotational energy likely due to water's higher ability to absorbed rotational energy. Previous gas phase studies on the translational energy distribution for the $\nu = 0$ are described by a single distribution as one would expect.[11, 12]

CHAPTER 5 REFERENCES

[1] C.M. Western, PGOPHER, a Program for Simulating Rotational, Vibrational and Electronic Structure, 2015.

[2] H. Zacharias, M. Geilhaupt, K. Meier, K.H. Welge, Laser photofragment spectroscopy of the NO_2 dissociation at 337 nm. A nonstatistical decay process, The Journal of Chemical Physics 74 (1981) 218-225.

[3] M. Kawasaki, H. Sato, A. Fukuroda, T. Kikuchi, S. Kobayashi, T. Arikawa, Angular distributions of photofragments from NO_2 photodissociation, The Journal of Chemical Physics 86 (1987) 4431-4437.

[4] M. Hunter, S.A. Reid, D.C. Robie, H. Reisler, The monoenergetic unimolecular reaction of expansion-cooled NO_2: NO product state distributions at excess energies 0–3000 cm−1, The Journal of Chemical Physics 99 (1993) 1093-1108.

[5] S.A. Reid, D.C. Robie, H. Reisler, Fluctuations in the unimolecular decomposition of jet-cooled NO_2: Implications for overlapping resonances and the transition state, The Journal of Chemical Physics 100 (1994) 4256-4271.

[6] A. Yabushita, Y. Inoue, T. Senga, M. Kawasaki, S. Sato, Photodissociation of Chlorine Molecules Adsorbed on Amorphous and Crystalline Water Ice Films, The Journal of Physical Chemistry B 106 (2002) 3151-3159.

[7] A. Yabushita, T. Hama, D. Iida, N. Kawanaka, M. Kawasaki, N. Watanabe, M.N.R. Ashfold, H.-P. Loock, Release of hydrogen molecules from the photodissociation of amorphous solid water and polycrystalline ice at 157 and 193nm, The Journal of Chemical Physics 129 (2008) 044501.

[8] K.P. Huber, G. Herzberg, (data prepared by J.W. Gallagher and R.D. Johnson III), Constants of Diatomic Molecules, in: P.J. Linstrom, Mallard W.G. (Ed.), "Constants of Diatomic Molecules", NIST Chemistry WebBook, NIST Standard Reference Database Number 69, National Institute of Standards and Technology, Gaithersburg MD, (retrieved April 9, 2016).

[9] J.A. Mueller, S.A. Rogers, P.L. Houston, Zero Kinetic Energy Photofragment Spectroscopy: The Threshold Dissociation of NO_2, The Journal of Physical Chemistry A 102 (1998) 9666-9673.

[10] A. Yabushita, Y. Inoue, T. Senga, M. Kawasaki, S. Sato, Photodissociation of N_2O_4 Adsorbed on Amorphous and Crystalline Water−Ice Films, The Journal of Physical Chemistry A 108 (2004) 438-446.

[11] J.A. Harrison, X. Yang, M. Roesslein, P. Felder, J.R. Huber, Photodissociation of NO2 at 355 and 351 nm Investigated by Photofragment Translational Spectroscopy, The Journal of Physical Chemistry 98 (1994) 12260-12269.

[12] C.-H. Hsieh, Y.-S. Lee, A. Fujii, S.-H. Lee, K. Liu, Photodissociation of NO_2 at 355 nm: pair correlation, Chemical Physics Letters 277 (1997) 33-38.

Chapter 6
Velocity Map Imaging of 355 nm Photodissociation of NO_2 in an Argon Matrix

6.1 Introduction

Velocity map images of the ionized NO photofragment in selected rotational states have been acquired at different delay times between pump and probe laser pulses, corresponding to different axial translational energies. This experiment gives a series of images showing slices of the expanding fragment "sphere" as it grows in time. Our study is an attempt to obtain radial velocity distributions and angular distributions of NO photoions formed after dissociation of NO_2 in an Ar-matrix and state-specific delayed ionization using REMPI. Using radial velocities along with the time of flight data in Chapter 5, the *total* translational energy for a given rotational state can be obtained. Images of different delay times can be used to visualize slices of the fragments' dissociation expansion.

6.2 Images for Different Time Delays

Images were taken with the REMPI laser set at a wavelength corresponding to the Q-branch head transition at λ = 226.26 nm as this was the band with the largest intensity. Images were recorded at a DAQ frequency of 10 Hz. The camera (Point Grey, Flea 3) was timed to have a short exposure time of 20 ms to reduce background stray light. The MCP detector was time-gated for the NO^+ ion and a Time Delay Generator (Scientific Instruments DG535) was used to trigger the two laser pulses. A LabView program, built in-house, is used to control the camera and recorded the images. Unless otherwise stated 1000 images were taken at each time interval. Image-J, an image analysis software, freely available by

the National Institutes of Health, was used to average and analyze the resulting images.[1] The resulting images can be viewed as a collection of slices through the expanding dissociation envelope. This method is related to the DC slicing technique of Suits and co-works[2] and the ion slicing method of the Kitsopoulos and co-workers [3] involving image slicing of the centre part of a Newton sphere.

6.3 Delay Time Images

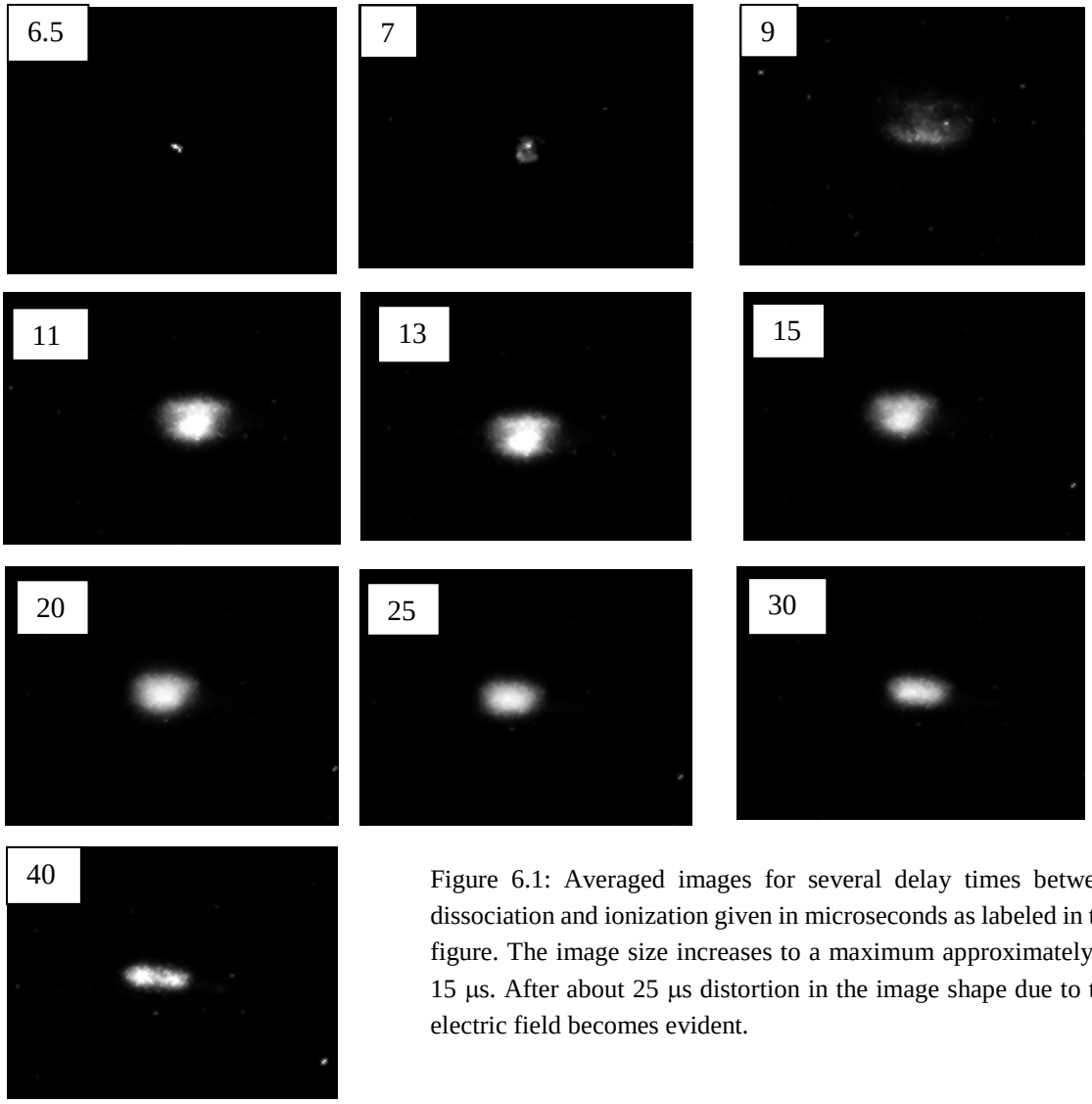

Figure 6.1: Averaged images for several delay times between dissociation and ionization given in microseconds as labeled in the figure. The image size increases to a maximum approximately at 15 μs. After about 25 μs distortion in the image shape due to the electric field becomes evident.

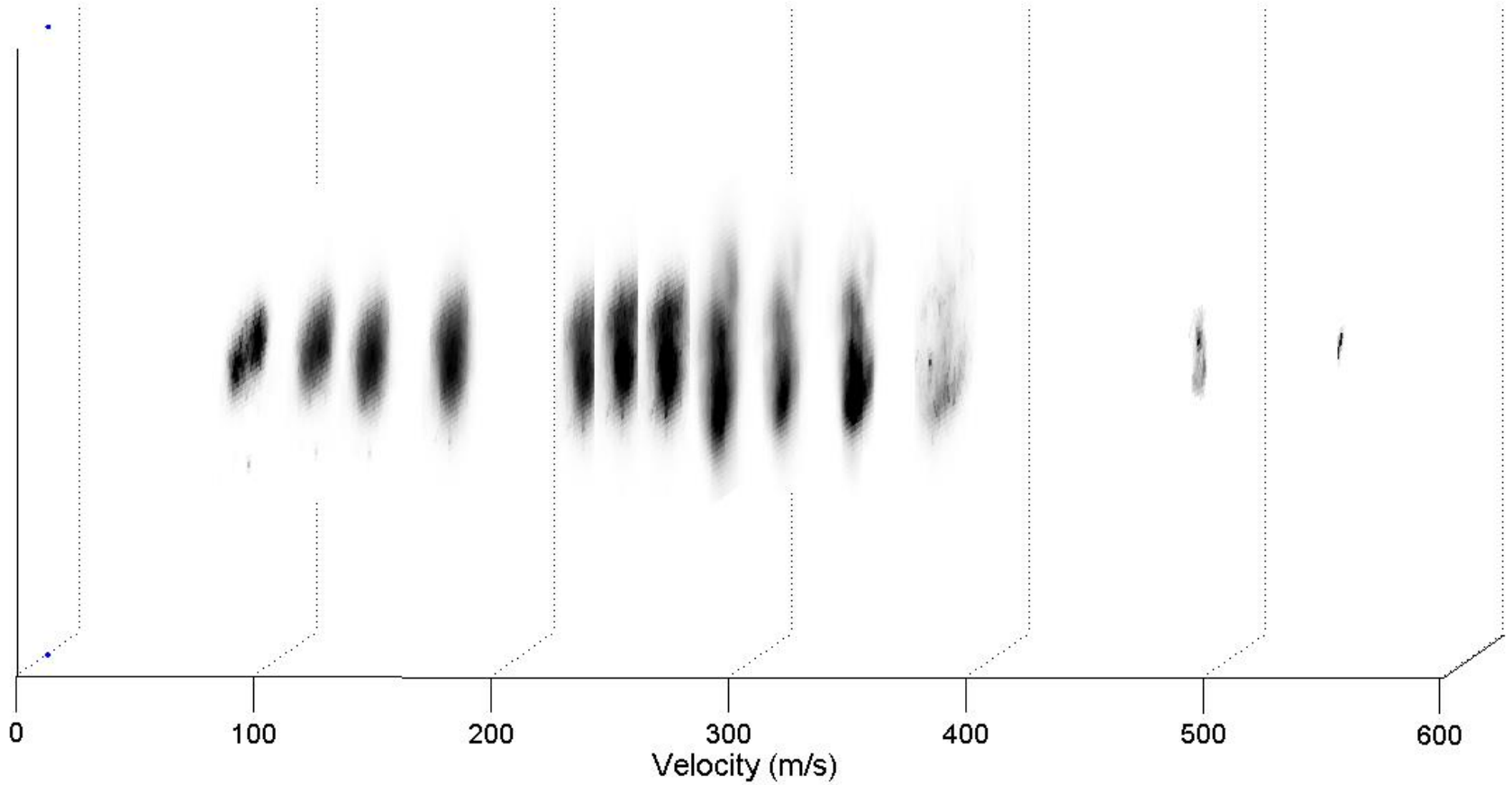

Figure 6.2:Velocity Map Images from the Q head plotted against their velocity along the time of flight axis. The collection of images, are slices through the expanding fragment cloud.

6.4 Measuring Image Size

It is evident from Figure 6.1 (40 μs) that at short delay times (high axial velocity) the image is small, i.e. the radial velocity component is small. At long delay times the images indicate a larger radial velocity which is eventually no longer circular. While the effect could indicate a non-uniform angular distribution, it is more likely that slow fragments are more affected by inhomogeneous electric fields in the acceleration region. To obtain an accurate description of the image size and therefore of the radial velocity distribution, each image was profiled along three axes, as shown in Figure 6.3. The length of the image along each axis was determined by measuring the full-width half-maximum (FWHM) of the intensity profile and by measuring the radius to the outer perimeter of the image to find the maximum radial velocity. Images were collected at a resolution of 1280×1024 pixels. In a calibration measurement we found that each pixel corresponds to a distance of 0.0649 mm.

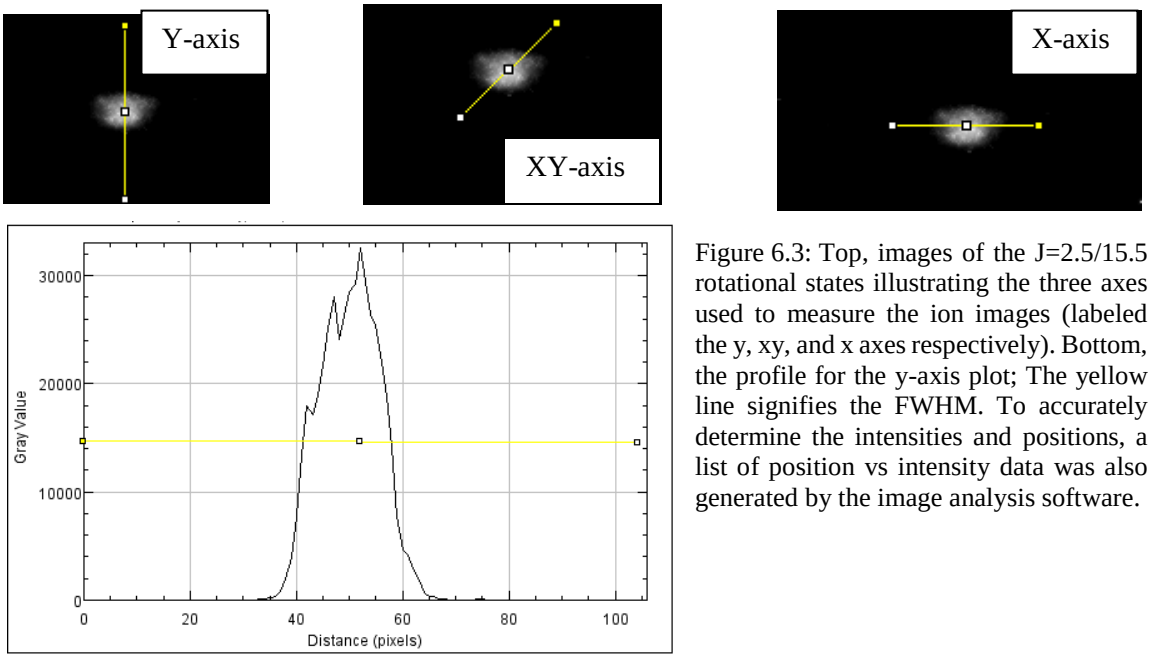

Figure 6.3: Top, images of the J=2.5/15.5 rotational states illustrating the three axes used to measure the ion images (labeled the y, xy, and x axes respectively). Bottom, the profile for the y-axis plot; The yellow line signifies the FWHM. To accurately determine the intensities and positions, a list of position vs intensity data was also generated by the image analysis software.

6.5 Radial Velocities from VM Images

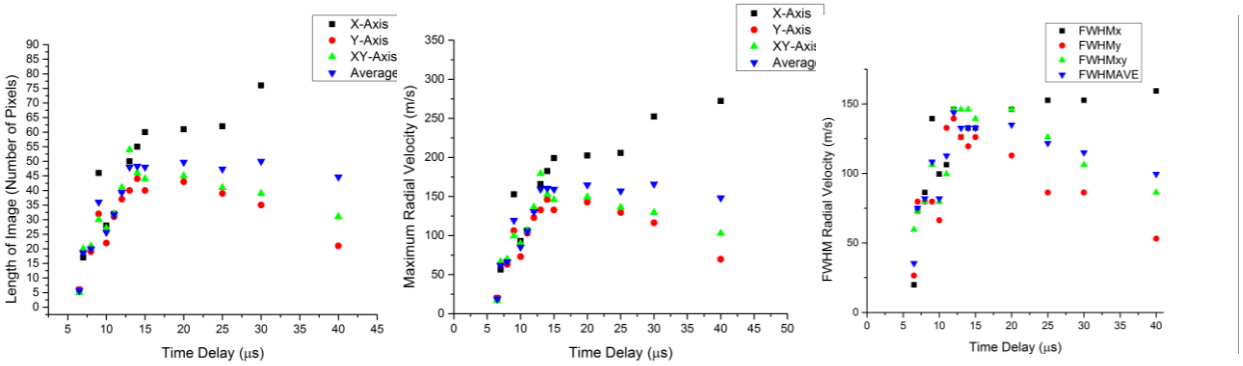

Figure 6.4: Left, Image size in number of pixels as a function of time delay between dissociation and ionization. The actual size of the images can be calculated by multiplying by a factor of 1 pixel to 0.065 mm and dividing by the magnification factor 1.37. The images increase in size as the delay is increased from 6.5 μs to 15 μs. After a 25 μs delay the image shrinks along the y axis but increases slightly along the x-axis. Right, Fragment velocities using full width half max of the image intensity distribution. Center, Maximum Radial velocities as a function of delay time, outer edge determined by threshold analysis of the outer image.

Figure 6.4 describes the image sizes as a function of time delay between the dissociation and ionization lasers. The images increase in size until the delay is 15 μs long. The images increase in size at a rate of 2.8 pixels/μs during the initial expansion period, corresponding to 1.8 mm/μs. The images are converted to velocities using the magnification factor, N = 1.37, given in Chapter 3, using the following formula.

$$\mathrm{v} = \frac{d}{N}\left(\frac{0.0000649\,pixels/m}{0.00000714s}\right) \tag{6.1}$$

Here, d is either the distance from the center of the image to the outer perimeter for maximum radial velocity analysis, or it is the FWHM given in pixels for the distribution velocity calculation. The fraction on the right of Equation (6.1) is the conversion from pixels to meter divided by the ion flight time. After 20 μs the velocity map imaging conditions begin to break down, distortions take hold and the images flatten shrinking in all directions except along the X-axis. The travel time for the ions from ionization to the

time they reach the detector is 7.14 μs. Using this number and the radii of the images at different delay times, the radial ion velocities, i.e. velocities in the plane perpendicular to the time of flight axis, can be obtained (Figure 6.4 right). Images after a time delay of 20 μs suffer from information loss explained in detail below. The shortest delay between dissociation and ionization at which an image was observed was 6.5 μs and corresponds to an axial velocity of 510 m/s. At this delay the fragments were seen to already have a speed of at least 20 m/s along the X, Y, and XY axes using the threshold velocity analysis. While some blurring due to space charge effects may have occurred, this should not affect the results to this degree. Additionally, when considering the delay time data in Chapter 5.3.2 (Figure 5.13) an ion signal can be observed at delays as short as 4 μs, i.e. for fragments that travel with 3.4mm/4μs = 850 m/s along the TOF axis. This suggests that if enough images were taken with a 4 μs delay then an image with an even lower velocity should have been observable. The largest velocity in the x or y direction was found to be close to 200 m/s (FWHM: 150 m/s) for images that were taken after a 15 μs delay i.e. when they have an axial velocity of about 230 m/s. The largest number of fragments therefore has radial and axial velocities around 230-170 m/s corresponding to a translational temperature around 100K.

In the imaging experiment there is a "cone of acceptance" for fragments which can reach the ionization region, which limits the maximal radial velocities of the fragments that can be detected. The distance between ionization and dissociation is 3.4 mm and the dissociation surface is at maximum 5 mm in diameter (diameter of the cold tip). Thus in order to be ionized, and therefore detected, the fragment must leave the cold tip surface at an angle higher than 54°. At any smaller angle the fragment will miss the ionization region

regardless of where it was fragmented. This means that we cannot detect fragments if their radial velocity is substantially larger than the axial velocity. This assessment does, of course, assume a point-like ionization region.

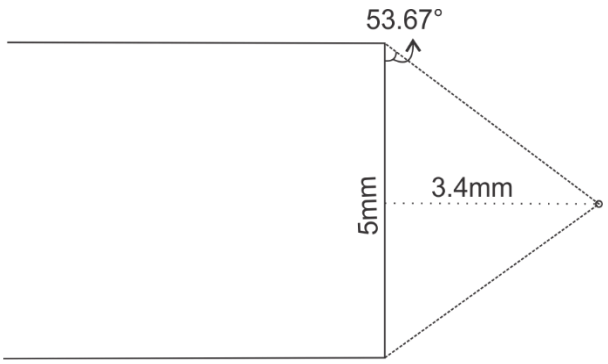

Figure 6.5: The ionization acceptance cone for the apparatus is given by the allowed angles for the fragments off-axis velocities. The distance between the cold finger and the ionization region is given by the dashed line, the angle 53.67° is the lowest angle that fragment can take on and be ionized.

At small time delays, only fragments which have the vast majority of their velocity along the time flight axis reach the ionization region yielding a smaller image. As the time delay increases, the size of the image increases as fragments which have components to their velocity along other directions are also ionized and imaged. After approximately 15 μs the images stop growing in size. This is because at this point, fragments with velocity components within the "cone of acceptance" have been imaged, and the images reach the maximum possible size. This is described in Figure 6.5.

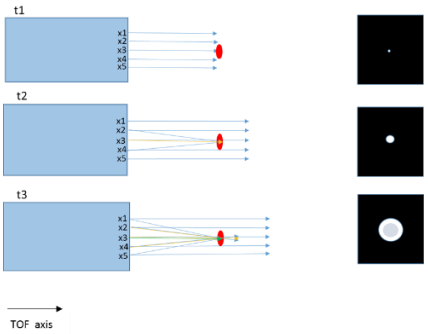

Figure 6.6: Simplified 2D view of dissociation and ionization process with fragments originating from five positions on the surface (x1 through x5). At a short time delay, t1, only fragments which originate at x3 and which have their velocities completely in line with the VMI (y) axis will reach the ionization region in time with the ionization laser pulse. At longer delay times, t2, particles which would have been imaged at delay time t1, now have too high a velocity in the y direction to be imaged. Now fragments at x3 with all of their velocity in the y direction must be moving slower in order to become ionized. Additionally at this point we see that some fragments originating at positions x2 and x3 may become ionized. The resulting image appears as a circle. At a much longer delay time, t3, the maximum image size has been reached as any fragments with larger x and y components of their velocities would miss the ionization region.

In any case, this issue is not of great concern, since the fragments' velocity distribution is such that in the case of high spatial anisoptropy ($\beta \approx 2$) the fragments formed by dissociating NO_2 in a parallel transition have a large axial velocity and a small radial velocity (the photolysis electric field vector is directed along the time of flight axis). In the other limiting case, the spatial anisotropy is $\beta \approx 0$. Radial and axial velocities are then approximately identical, as is indeed observed for the slow fragments.

6.6 Image Intensity as a Function of Time Delay

The ion image intensity in the center of the image can be used to find the axial velocity distribution as a function of delay time, this is known as "core-sampling".[2, 4] The image intensity directly in the center of the image is generated only by fragments traveling without radial velocity. The results from this experiment may be compared with the total velocity distributions in Chapter 5.

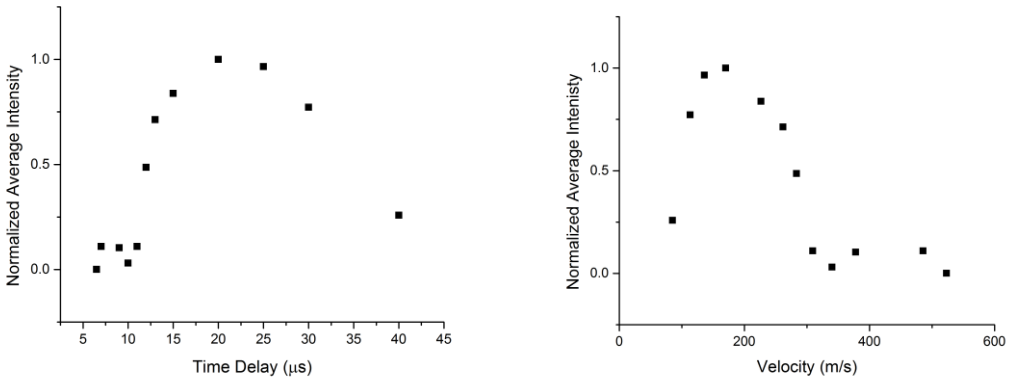

Figure 6.7: Left, Normalized image intensity of center 9 pixels for each time delay. Right, the same data plotted against axial velocity. It is clear that the distribution is bimodal in each plot, which matches the total ion intensity plots found in Chapter 5.3.2.

The core-sampled image intensity as a function of time delay (Figure 6.7) compares very well with the arrival time measurements in Chapter 5.3.2 which give the total ion intensity as a function of time delay. Figure 6.7 was generated using REMPI lines from the Q-branch head which contains several rotational states.

When we compare this velocity distribution to those in e.g. Figures 5.13 and 5.14 where the velocity distribution is also bimodal we see that the first NO photofragments arrive between 6 and 8 μs, and a second slower group peaks between 15 to 20 μs. This matches the data in Fig 6.7 which show two peaks at 8 μs and at 20 μs. This corresponds to a bimodal velocity distribution with peaks at v = 190 m/s and 450 m/s. As expected there is good agreement between the arrival time technique (e.g. Figures 5.15) and the core-sampling method used here. The ability to monitor axial, radial and total fragment velocities illustrates the utility of the condensed phase velocity map imaging apparatus described within this thesis.

6.7 Total Translational Energy

The translational energy along the time of flight axis can be obtained simply from the delay time between dissociation and ionization. The radial translational energy distribution along the perpendicular axes can be obtained from the images in Figure 6.1, the average distribution can be approximated by the FWHM velocities in Figure 6.4. The sum of the radial translational energy and translational energy along the TOF axis yields the total translational energy for each time delay. This is dependent on the total fragment distribution falling within the acceptance cone described in Figure 6.5, that is for the setup described here for time delays of 15 μs and shorter. At longer delay times not all of the fragments may be imaged and there is a maximum in the image size and thus radial translational energy.

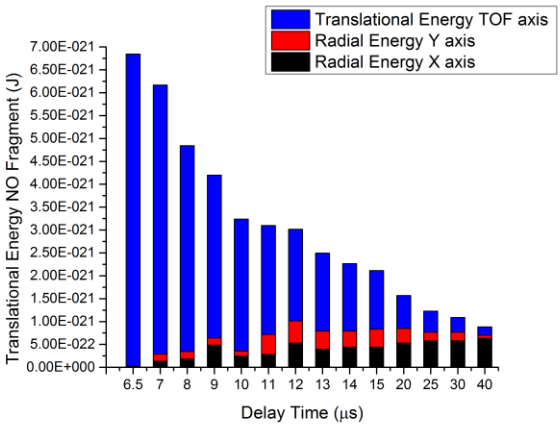

Figure 6.8:Total translational energy of the NO fragment from 6.5 to 40 μs delay times. Loss of energy along the time of flight direction correlates with an increase in radial translational energy. Additionally loss of total translational energy of the NO fragment at later delay times is due to possibly increased velocity of the oxygen cofragment and quenching into the ice matrix.

The translational energy components can be graphed against delay time. Figure 6.8 shows that loss of translational energy along the time of flight axis correlates with an increase in radial energy in both directions as expected until 15 μs, at which point the radial energy is

constant for a further 15 μs. After this time interval distortions take over, flattening the image, causing the apparent radial energy in the y direction to decrease and increase in the x direction. It is evident that the loss of translational energy along the TOF direction is not fully compensated for by the increase in energy in the radial directions. The energy lost at longer delay times is then partitioned into the kinetic energy of the oxygen co-fragment as well as being quenched into the argon matrix. The highest translational energy observed was at a delay time of 6.5 μs with an energy of 3.427×10^{-21}J or 163 cm^{-1}, while the lowest energy 1.97952×10^{-21} J (99.7 cm^{-1}) was observed at 15 μs.

6.8 Images as a Function of Rotational State

Images were taken for selected rotational states of NO by probing the pP1 branch (J = 1.5/16.5 to 6.5/11.5) at delay times of 15 μs and 20 μs in order to identify any effect of the rotational state on the velocity distributions. Images are shown in Figure 6.9.

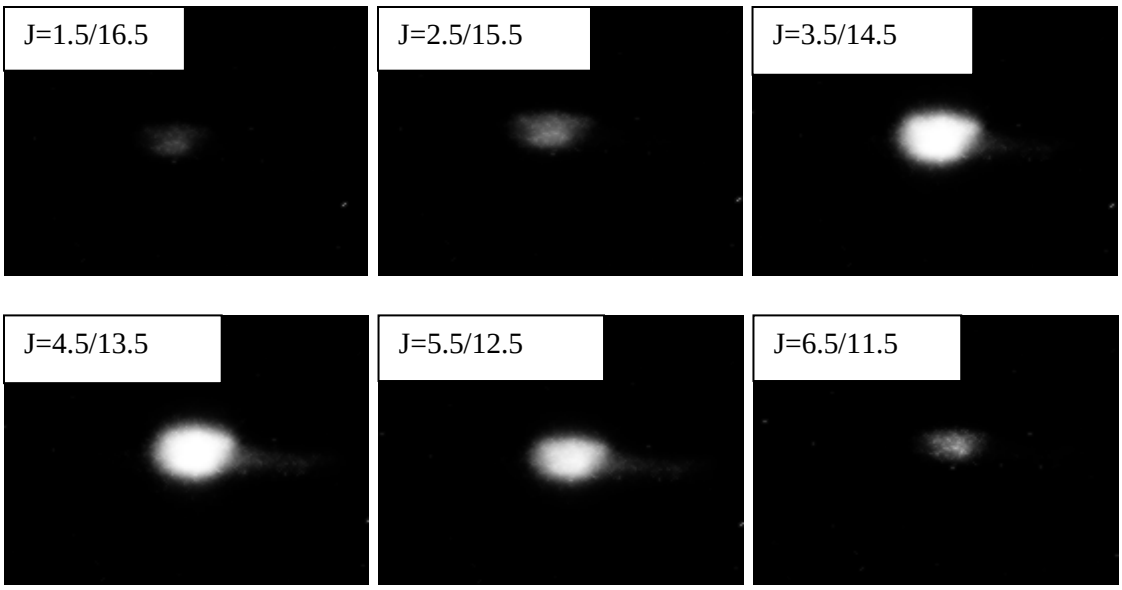

Figure 6.9: Ion images of the pP1 branch from J=1.5/16.5 to J=6.5/11.5 with a 15 μs delay between dissociation and ionization laser pulses. The images show little change in overall size, however the overall intensity mirrors the ion intensities seen in Chapter 5.2.2.1. The pP1 branch was chosen as it was intended to be used to identify and differentiate the overlapping rotational states. Unfortunately, due to the lack of difference in size between rotational states this was not possible.

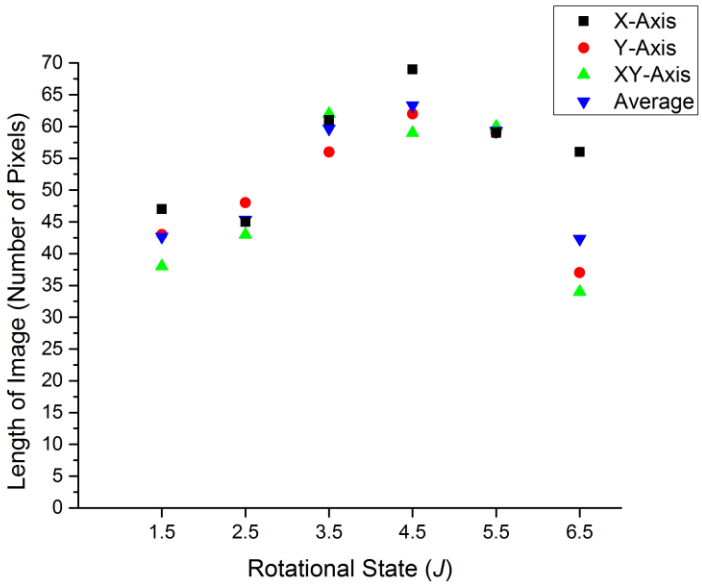

Figure 6.10: Image size for different rotational states of the pP1 branch again at a 15 μs delay. The size of the images does not vary between the individual states to a great extent. A slight increase in size can be seen between at larger J values peaking around J=4.5.

Image sizes (as determined by the FWHM) do not vary to a large extent with respect to rotational state. This indicates that the radial velocities of the fragments are not influenced by the given rotational state, and limits our ability to resolve overlapped rotational lines based on their radial velocity.

As expected the image intensities are dependent on the rotational state, though, and can be used to monitor ion intensities. Based on the results from the REMPI spectra in Chapter 5, the REMPI spectrum obtained with a 9 μs delay between pump and probe laser pulses shows that the lines have the same intensity (Figure 6.11). One would expect that at short time delay the J=1.5/16.5 and J=6.5/11.5 lines have similar intensities. Figure 6.11 indicates that this holds true also when recording images. At longer delay times one expects the intensity to increase from J = 1.5/16.5 to the higher levels peaking at J = 4.5 which is indeed observed in the images from Figure 6.9.

Figure 6.11: Ion images for J=1.5/16.5 and J=6.5/11.5. Fragments were ionized after a 10μs delay. The intensities of the two images are relatively similar at this time delay compared to that of the 15 μs delay data seen in Figure 6.9. This illustrates not only the ability of images as a rough guide of ion population but further supports the findings in Chapter 5 that the ion intensities of certain rotational states differs with delay time.

6.9 Summary

Condensed phase velocity map imaging, as described here, has been shown to be an effective method to determine the two radial velocities of different fragments from a

condensed material. The third velocity component, along the time of flight axis, can be obtained by measuring the arrival time distribution, i.e the signal intensity as a function of delay between pump and probe laser (Chapter 5). The total translational energy of the fragment can then be determined at each time delay by adding these energies. Total translational energy was found to decrease at longer delay times with the energy difference being partitioned into the oxygen co-fragment and quenching into the matrix.

When monitoring the image size with respect to time delay, we obtain slices along the radial velocity distribution. Images were seen to increase in size until 15 μs at which point the images remained constant until roughly 25 μs when distortions caused the images to "flatten" out and they can no longer be used for velocity analysis. The average maximum velocities of the fragments in the non-time of flight axes was found to be 225 m/s which corresponds well with average velocity found in Chapter 5. The discrepancies between the on axis and off axis velocities at long delay times is partly explained by the fact that not all off axis velocities can reach the ionization region and thus cannot be imaged. This could be mediated by future researchers by putting the ionization region closer to the cold finger. However, this would necessitate either moving the ionization region away from the centre of the repeller and extractor electrodes, or by extending the cold finger further into the acceleration region. Both techniques necessitate a much more difficult ion optic set-up to achieve VMI conditions.

The sizes of the ion images were not found to depend on *J* to a large extent. This limits the ability to resolve overlapping lines within a rovibrational spectrum. Some slight differences in the size of the images for different rotational states were found, which indicates that potentially with improvements to the ion optic design and longer image averaging it may

be possible to differentiate overlapping lines. As expected, image intensities were found to correlate well with the REMPI spectra generated in chapter 5, and supported the findings that different delay times between dissociation and ionization lead to different rotational state populations.

CHAPTER 6 REFERENCES

[1] W.S. Rasband, ImageJ, U. S. National Institutes of Health, Bethesda, Maryland, USA, 1997-2015.

[2] D. Townsend, M.P. Minitti, A.G. Suits, Direct current slice imaging, Review of Scientific Instruments 74 (2003) 2530.

[3] C.R. Gebhardt, T.P. Rakitzis, P.C. Samartzis, V. Ladopoulos, T.N. Kitsopoulos, Slice imaging: A new approach to ion imaging and velocity mapping, Review of Scientific Instruments 72 (2001) 3848-3853.

[4] C.-H. Hsieh, Y.-S. Lee, A. Fujii, S.-H. Lee, K. Liu, Photodissociation of NO_2 at 355 nm: pair correlation, Chemical Physics Letters 277 (1997) 33-38.

Chapter 7

Summary and Conclusions

This thesis describes the development of a new condensed-phase velocity map imaging apparatus for use in monitoring the dissociation dynamics of photoreactive species when trapped in and on frozen materials. We have shown that a perpendicular arrangement of the cold finger longitudinal axis with the time of flight axis leads to distortions which we were not able to correct. When the cold finger was placed along the time-of-flight axis, however, VMI images were produced both from gas phase experiments and from molecules doped into an argon matrix deposited on its surface. Ion trajectory calculations which included the dielectric correction for the coldfinger's sapphire rod were able to model our system well and produced a magnification factor of 1.37.

With the apparatus, we recorded REMPI spectra of the NO photofragment generated by dissociating at 355 nm NO_2 doped into an argon matrix at 20K. The distributions of the (v=0) NO photofragment over the many rotational states populated were found to change significantly when the fragments were detected with high or with low axial translational velocity, i.e. at different stages of the expanding NO fragment distribution. This was evident from the fragment spectra and also from the intensity of rotationally selected photofragments as a function of travel time from the matrix into the ionization region. Two rotational temperatures were found by fitting the properly weighted REMPI line intensities to a Maxwell-Boltzmann distribution. One rotational distribution was either non-thermal or had a temperature well above the matrix temperature. This distribution was dominant at short delay times, i.e. for fragments that leave the matrix with high velocity. The other rotational distribution was cooled to within 20 degrees of the matrix temperature and was

found to dominate at longer delay times, i.e. NO for fragments that leave the surface with low velocity. The translational energy distribution was found to reflect the rotational distribution and also showed a bimodal behavior, having one translational temperature near the matrix temperature and a second much higher temperature.

These observations agree well with the proposed mechanism of two distinct yet blended dissociation pathways. We propose that a small number of NO_2 molecules dissociate from surface sites or from sited near the surface of the argon ice matrix. They then leave the matrix after minimal interactions. These are rotationally and translationally hot molecules that have a large axial velocity and a comparably small radial velocity, i.e. they may retain some memory of a parallel transition. In general the hot NO photofragments have characteristics similar to those formed by gas-phase NO_2 photodissociation. Molecules dissociating from within the bulk matrix, however, are much slower, and have "cooler" rotational and translational energy distributions. These molecules undergo collisions within the matrix, which absorbs some of the rotational and translational energy from the fragments. The translational energy is reduced to near matrix temperatures whereas the rotational quenching is less efficient – likely due to the limited ability of argon to accept rotational energy.

The main novel aspect of the apparatus is its ability to image the radial velocities of the fragments. This allows us for the first time to image the radial and axial translational velocities as a function of delay time between dissociation and ionization from a condensed surface as well as a function of the internal state of the photofragments.

These experiments produce slices of the expanding fragmentation cloud. The intensity at the center of each image as a function of time was used to determine the axial velocity

distribution as the delay time changes, whereas the radius of the images gives the radial information. The axial velocity distribution matches the overall characteristics of the total translational energy from the arrival time data very well. The radial velocities were not found to vary to any great extent with respect to the different rotational states, however, the intensity data matches that found from the REMPI spectra well. Using energy balancing arguments we have shown that a large proportion of the fragmentation energy is either quenched into the matrix or is transferred directly to the oxygen co-fragment.

Future explorations into condensed phase velocity map imaging could include several different aspects as the machine operational principle is quite flexible. Future experiments on condensed phase NO_x species may include an investigation into the oxygen co-fragment or into the higher vibrational NO states. Of course using a different matrix material may be exciting to investigate e.g. reactions of H_2O with NO_2 or possibly with NO_3^-. Taking action spectra by monitoring the different fragmentation patterns as a function of dissociation wavelength with a tunable laser source is possible, as is monitoring matrix temperature effects. This is especially relevant to water ice matrices converting between low density amorphous ice to high density and finally into polycrystalline ice. It may even be possible to fragment non-cooled condensed phase matter, such as different matrix assisted laser desorption ionization (MALDI) matrices to investigate the different ionization processes.

Appendix

A.1 Programing Codes

This appendix describes the software codes that were built and used within this thesis. Codes were generated for Labview, and the graphical user interface (GUI), and the wire-diagram are both shown as well as a flowchart which describes the process that the program takes. For Matlab codes, the scripts are shown along with comments.

A.2 Labview Codes

Labview was used to control several aspects of the apparatus. The two main programs built were for data acquisition (DAQ). The first program, steppingnoscroll9.vi, also known as REMPIcontrol9 controls the dye laser's grating angle and BBO crystal orientation, which controls the output laser wavelength used for ionization. It also synchronizes the oscilloscope for data acquisition and saves the data. The second program TimeDelay.vi serves a similar purpose controlling the DG-535 delay generator which is used to change the time delay between the dissociation and ionization lasers. Additionally it also records the signal from the scope.

A.2.1 Steppingnoscroll9.vi

The REMPI Labview program GUI can be separated into three parts, A) Laser Control, B) Data Acquisition and file saving, C) Real Time Analysis of Signals.

A) Laser Control

This section is dominated by several selectors. Here we ensure that the motors that control the grating angle and the BBO crystal are initialized (Large button on the left) and are selected in the example to allow independent manipulation. To the right of these we have indicators showing the last known position of the Crystal and Grating, labeled 'crystal' and 'Position'.

To the far right we have several redundancy checks to ensure that the program runs smoothly as improper settings can cause large misalignment of the dye laser frequency and doubling crystal angle. These are the Remote Control and Execute buttons.

Finally in the lower part of Section A are the indicators labeled Current Position, these allow the user to select the desired wavelength (End nm) and view the current position (start nm). To the far left of the "# of loops" control is where the user selects the number of pauses between the initial position and the end position; this is the number of steps that will be recorded. Current Loop, Target Time and nm/loop are all indicators that illustrate the current loop of the scan that the system is on, the time the system takes per loop, and the resolution for each step of the loop.

B) DAQ and File Saving

This section allows the user to select the file path for saving of information, the main components to be saved are the REMPI signal, (REMPI Save?) the OPO laser intensity (OPO save) and the REMPI beam intensity (PD save). Additionally there is a selector to save each individual waveform from the scope along the run (Save Wave?). This is only used during troubleshooting the system.

C) Real Time Analysis and Intensity recording.

This section allows the user to analyze the ion signal Channel 1, the red and blue cursors allow the user to select the peak which will be integrated. Additionally, the program automatically will provide a second set of cursors with the same width as the former cursors, used for backgrounding.

Channel 2 and 3 are the photodiode signal from the REMPI laser and OPO laser (off in the current picture) respectively.

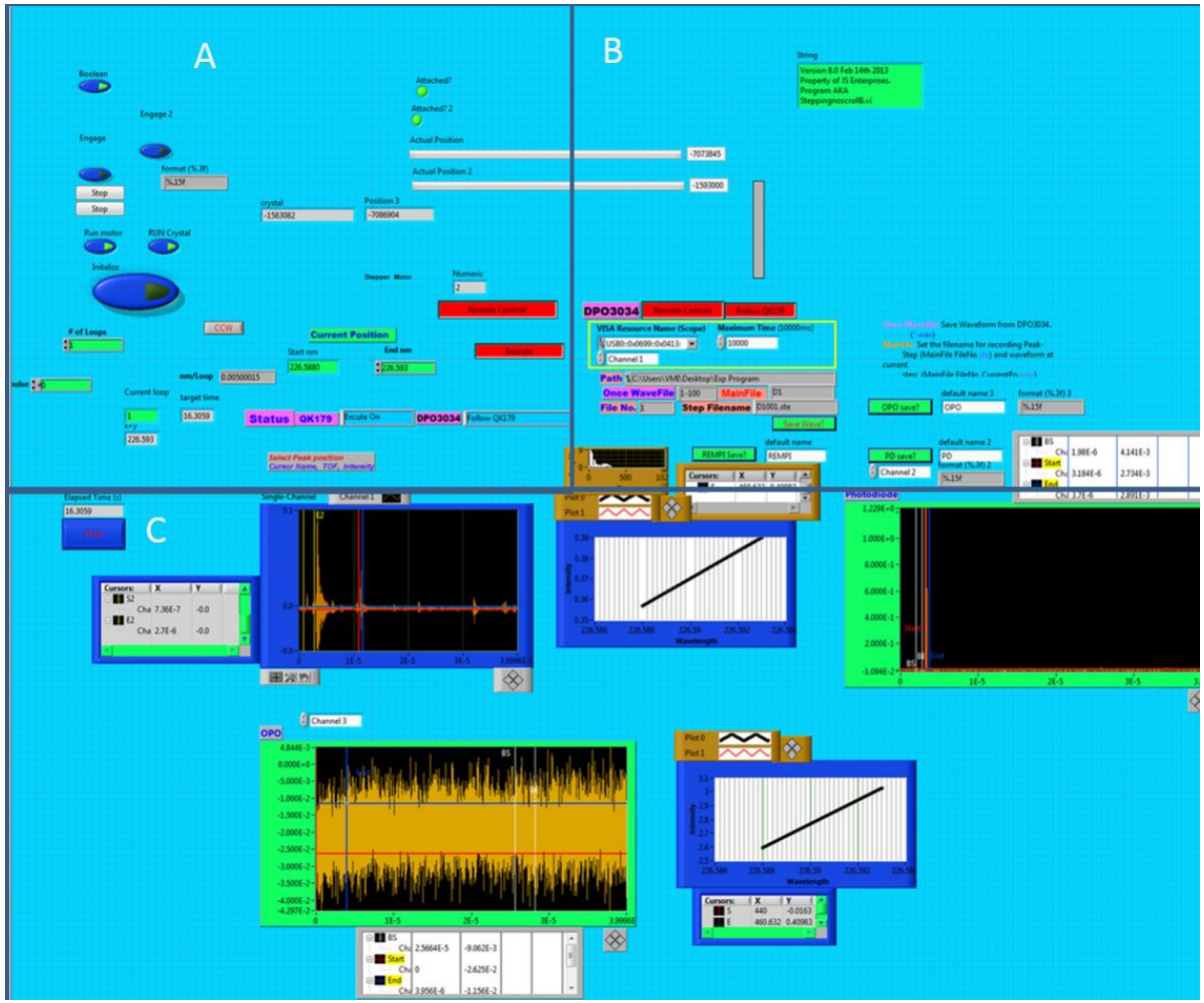

Figure A.1: Stepping motor GUI, used to scan REMPI laser, record ion signal, REMPI laser power, and YAG laser power.

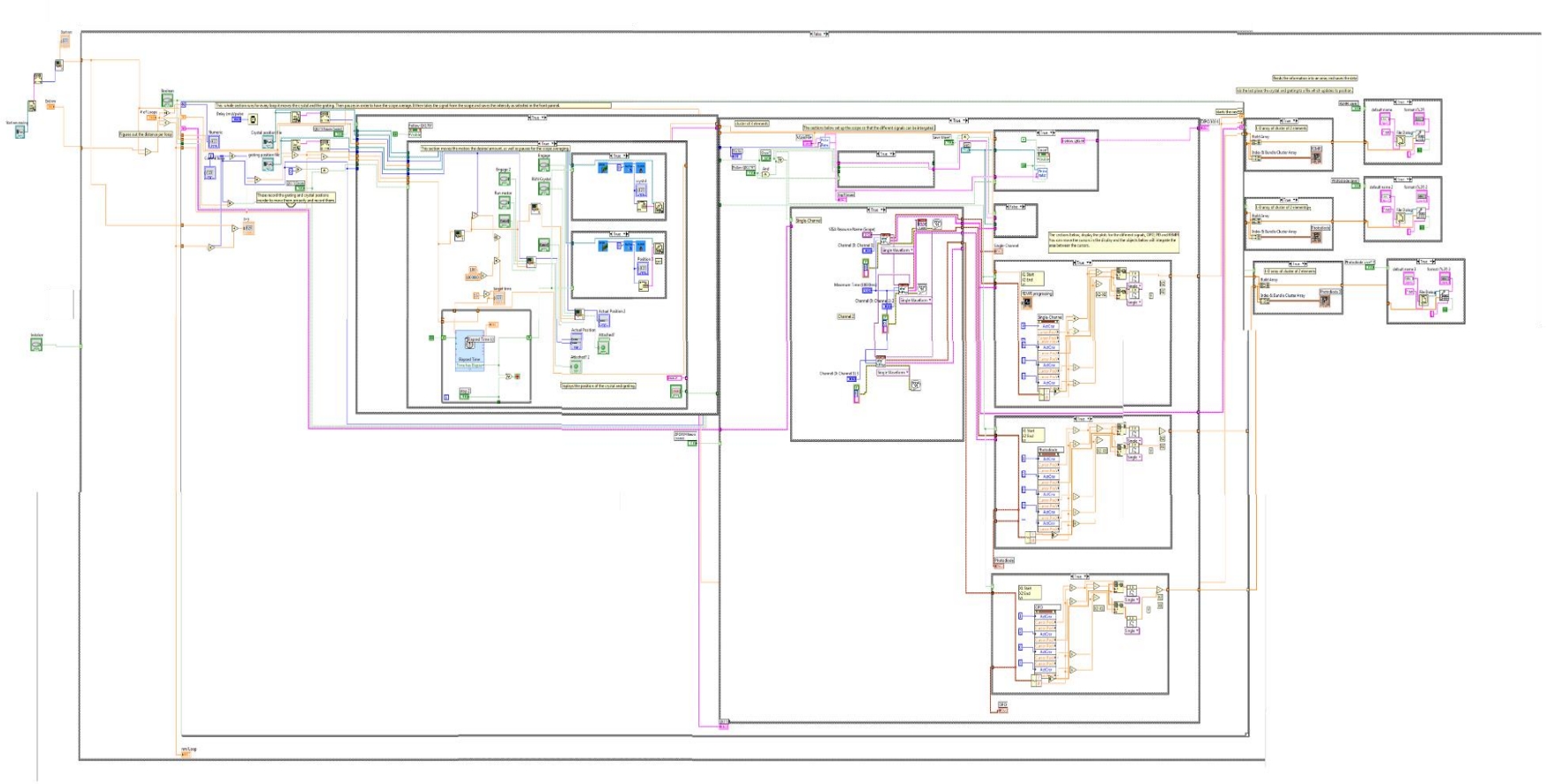

Figure A.2: Stepping motor wire diagram, see flowchart, figure A.3 for explanation.

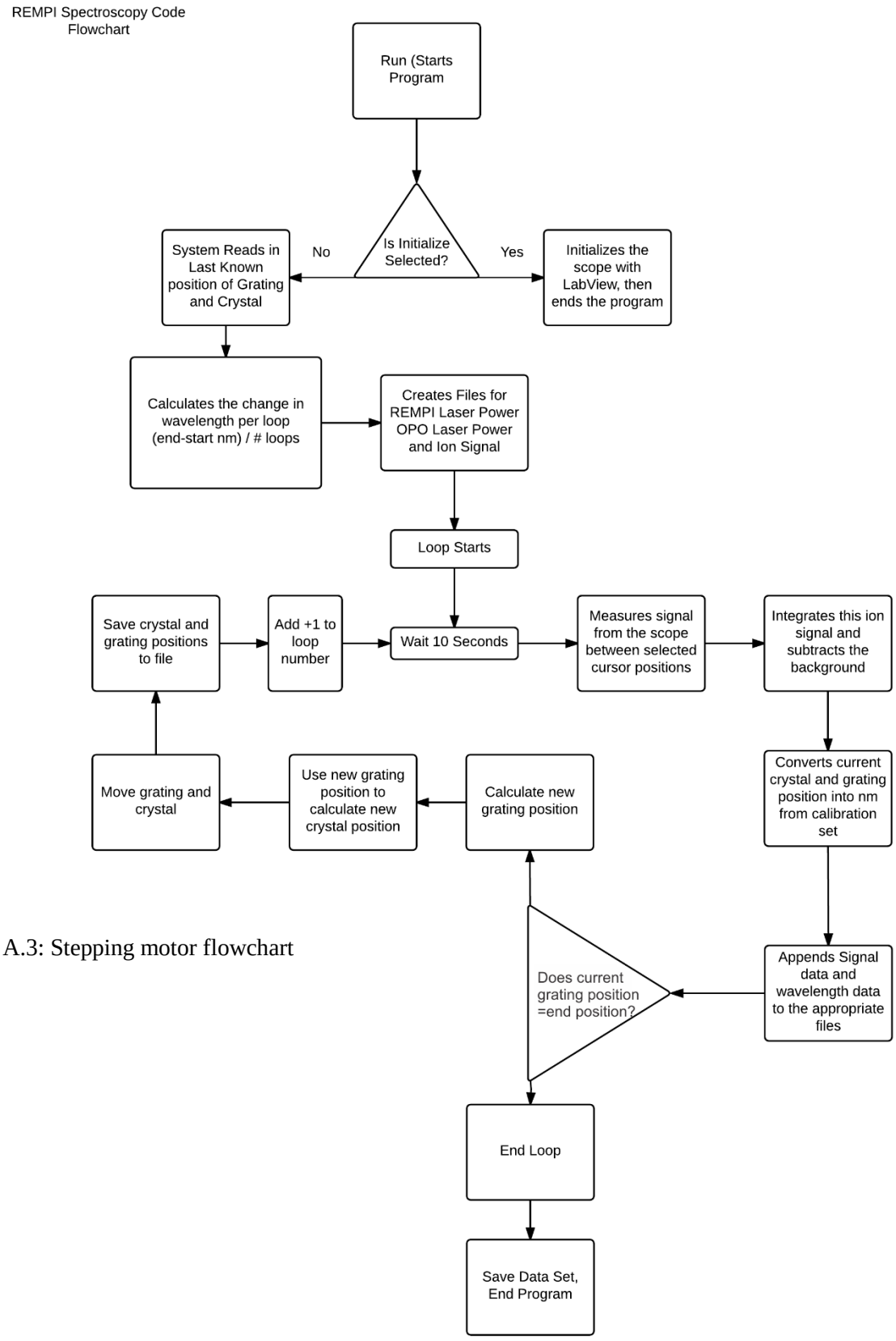

Figure A.3: Stepping motor flowchart

A.2.2 IntensityvsTimedelay2.vi

IntensityvsTimedelay2.vi program is used to generate the time delay plots, and works in a similar manner to the previous REMPI code. In this case rather than controlling the dye laser, the user selects a start time delay (Red box) and an End time delay (Blue box) as well as the total number of loops. Again, the user is able to monitor the laser intensities and the ion signal. The selected signals are integrated and recorded as a function of time delay.

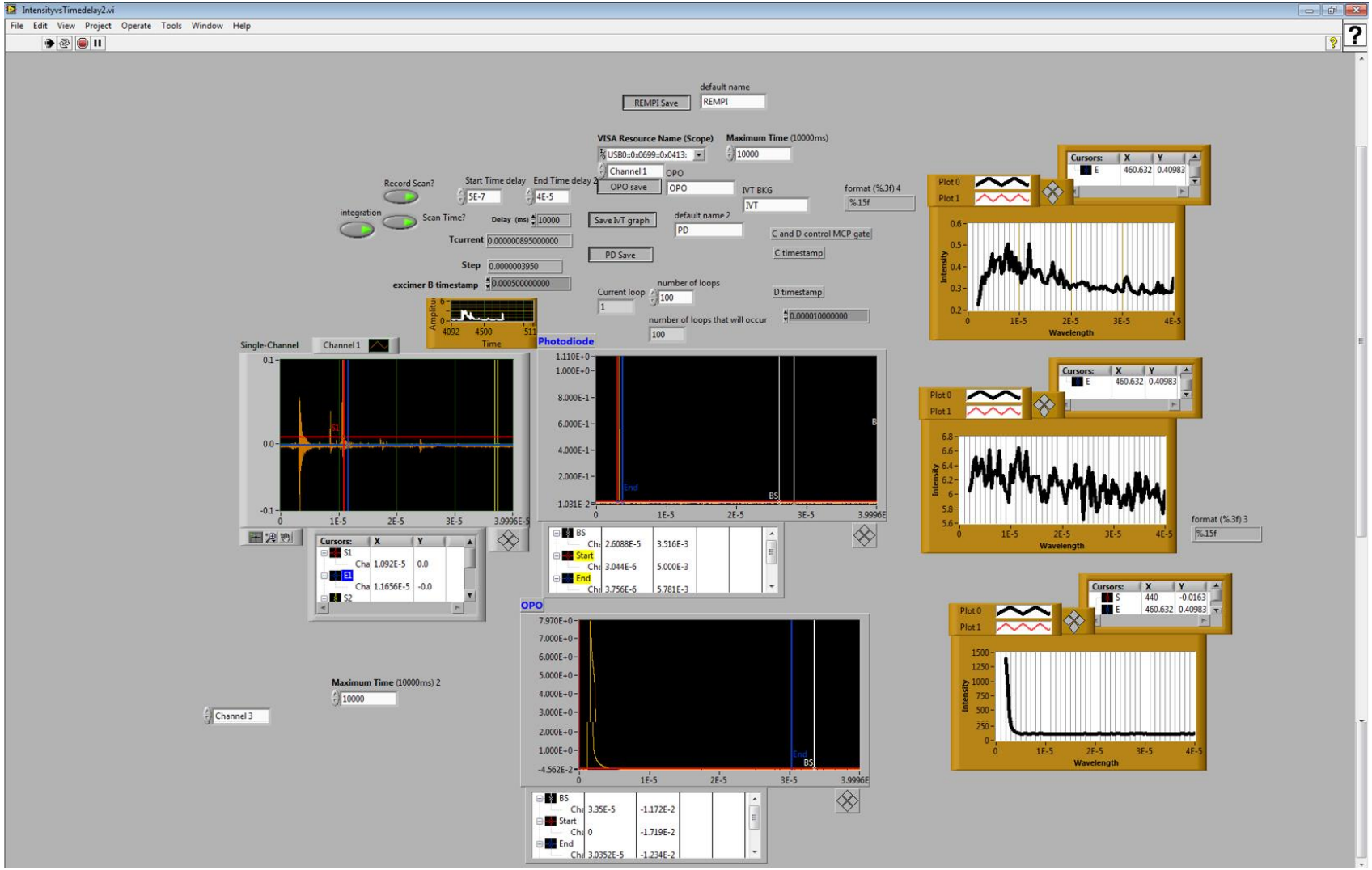

Figure A.4: Time Delay GUI, used to scan delay time between dissociation and ionization lasers as well as record ion signal and laser powers

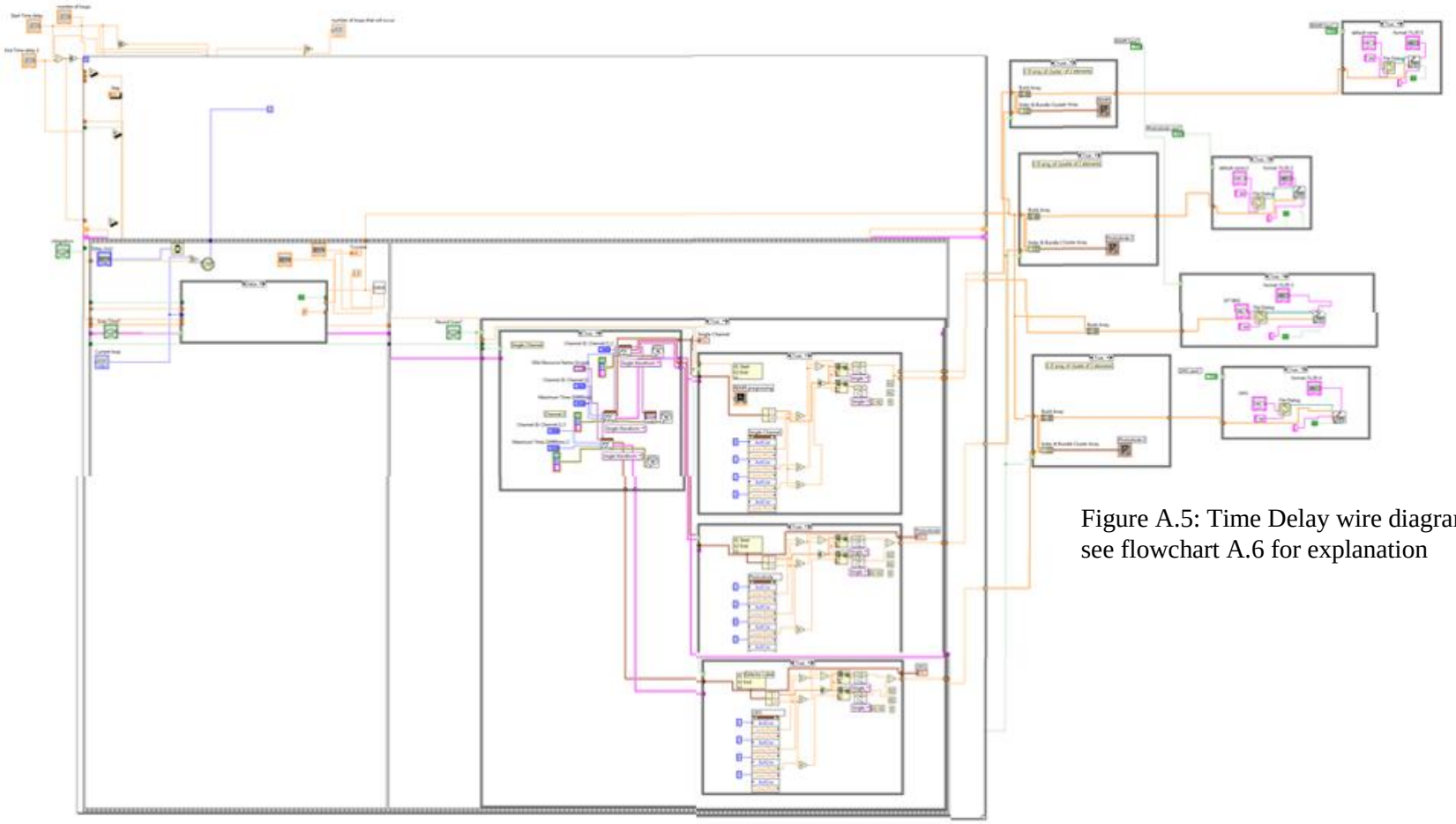

Figure A.5: Time Delay wire diagram, see flowchart A.6 for explanation

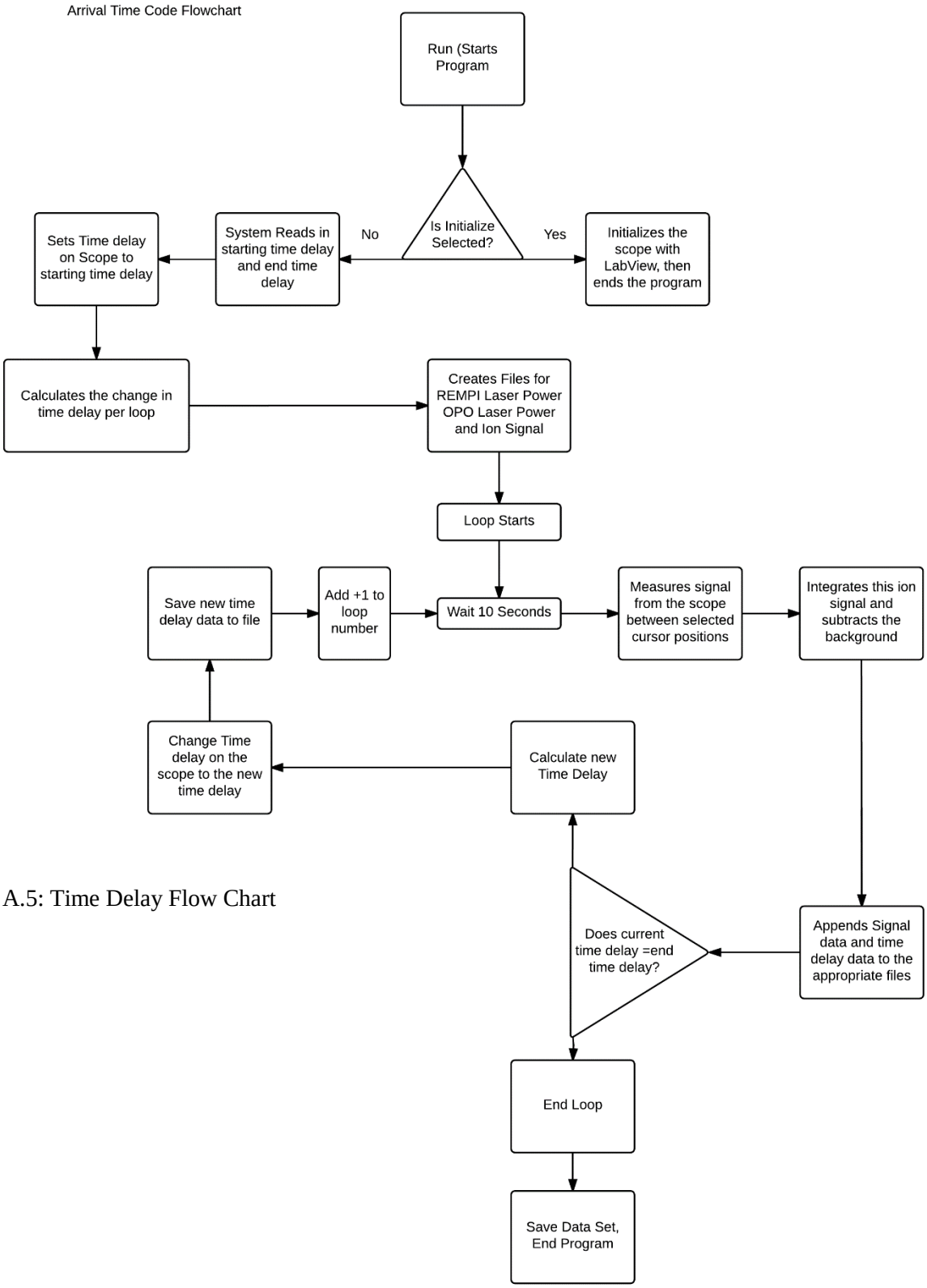

Figure A.5: Time Delay Flow Chart

A.3 Data Analysis Programs

A.3.1Appending Data from Scans and Laser Power Scaling

The ion signal data is from the REMPI experiment, is exported from the Labview program in a series of wavelength, intensity datasets. These are appended to each other using a Labview code, which also calibrates the intensity for the laser intensity.

```
REMPIDatawave=zeros(1,1); %Makes zero, to attach the data to the top of
file
REMPIDatasig=zeros(1,1); %same
for i=1:2
    filename=['REMPI' num2str(i) '.txt'];
    REMPIDat=dlmread(filename); %reads the files from the labview code
    fid = fopen(filename, 'rb');
%# Get file size.
fseek(fid, 0, 'eof');
fileSize = ftell(fid);
frewind(fid);
%# Read the whole file.
REMPIdata = fread(fid, fileSize, 'uint8');
%# Count number of line-feeds and increase by one.
numLines = sum(REMPIdata == 10);
halfnumlines = numLines/2;
fclose(fid);
    REMPIwave=REMPIDat(1:halfnumlines,1);%Selects  the  Wavelength  for
each set of data and adds the offset
    REMPIDatawave=cat(1,REMPIDatawave,REMPIwave);%sticks new data to the
previous loop ie file

    REMPIsig=REMPIDat(halfnumlines+1:end,1);% Selects the signal data for
each file
    REMPIDatasig=cat(1,REMPIDatasig,REMPIsig);%same as datawave
REMPIDatawave(1,:)=[];%deletes the first row, ie 0
REMPIDatasig(1,:)=[];%deletes the first row, ie 0
end
REMPIData=cat(2,REMPIDatawave,REMPIDatasig); %joins the two files as one
filename=['REMPIappend.txt']; %saves file for later
dlmwrite(filename,REMPIData,'precision',10); %saves file for later

wave=zeros(1,1); %Makes zero to attach the data to
sig=zeros(1,1); %same
for i=1:2
    filename=['PD' num2str(i) '.txt'];
    REMPIDat=dlmread(filename); %reads the files
    fid = fopen(filename, 'rb');
%# Get file size.
fseek(fid, 0, 'eof');
```

```
fileSize = ftell(fid);
frewind(fid);
%# Read the whole file.
PDdata = fread(fid, fileSize, 'uint8');
%# Count number of line-feeds and increase by one.
numLines2 = sum(PDdata == 10);
halfnumlines2 = numLines2/2;
fclose(fid);
   PDwave=REMPIDat(1:halfnumlines2,1)  +  997E-9  ;%Selects  the  first  51
wavelengths
    wave=cat(1,wave,PDwave);%sticks new data to the previous loop ie file

    PDsig=REMPIDat(halfnumlines2+1:end,1);% Selects the signal data for
each file
    sig=cat(1,sig,PDsig);%same as datawave
wave(1,:)=[];%deletes the first row, ie 0
sig(1,:)=[];%deletes the first row, ie 0
end
PDData=cat(2,wave,sig); %joins the two files as one
filename=['PDappend.txt']; %saves file for later
dlmwrite(filename,PDData,'precision',10); %saves file for later
%%
RCal=zeros(1,2);
    filename=['REMPIappend.txt'];
    REMPIDat=dlmread(filename); %reads the files
    fid = fopen(filename, 'rb');
%# Get file size.
fseek(fid, 0, 'eof');
fileSize = ftell(fid);
frewind(fid);
%# Read the whole file.
REMPId = fread(fid, fileSize, 'uint8');
%# Count number of line-feeds and increase by one.
numLines3 = sum(REMPId == 10);
halfnumlines3 = numLines3/2;
fclose(fid);
for  i=1:numLines3; %# this section catenates the data and calibrate for
the laser power
     num=REMPIData(i,2)./(PDData(i,2).^0.88);
      wav=REMPIData(i,1);
      Brick=cat(2,wav,num);
  end
  RCal=cat(1,RCal,Brick);
end
RCal(1,:)=[];
filename=['REMPICal.txt'];
dlmwrite(filename,RCal,'precision',10);  %# exports the newly corrected
data.
%%
```

A.3.2REMPI Spectra Code

Once the data has been zeroed and corrected for background the data is used to produce the REMPI spectra and Boltzmann plots show in chapter 5. The exact same code is used for the time delay data. In this case one would use time delay / intensity pairs rather than wavelength / intensity pairs.

The corrected REMPI data is fit to the Boltzmann plots using a second Matlab code,

```
kB = 1.3806485e-23; %kB
xData=rotEcal;%Data label for the rotational energy which is converted
from the wavelength data.
yData=pop;% intensity data
options = optimset('TolFun', 1e-20, 'MaxFunEvals',9000)% options for the
fitting parameters
x=[-0.00052 1.5 5e-04 7]; % Fitting guesses
lb=[-Inf -Inf -Inf 3 ];% lower Bounds for fitting parameters
ub=[0 Inf Inf 10];% upper bounds
F1=@(x,xData) ((exp((x(1).*xData) -x(2)))+(exp((x(3).*xData) - x(4))))%
Expression for the sum of the two fluxweighted Boltzmann fits
F2=@(x,xData) ((exp((x(1).*xData) - x(2))))%The first term
F3=@(x,xData) ((exp((x(3).*xData) - x(4))))%the second term
[x,resnorm,residual,exitflag,output,lambda,jacobian]                    =
lsqcurvefit(F1,x,xData,yData,lb,ub,options);% fittign procedure
conf = nlparci(x,residual,'jacobian',jacobian,'alpha',0.05)% Confidence
interval data
semilogy(xData,yData,'.',xData,   F1(x,xData),xData,   F2(x,xData),xData,
F3(x,xData)); %Plotting data
axis([0,2500,.00001,1])%axes for plot
```

A.3.3Boltzmann Code

The Boltzmann fits for the time delay data are done in a similar way to the REMPI spectra.

```
kB = 1.3806485e-29; % Boltzmann in corrected units
m = 4.9844*10^-26; %NO mass
xData=Dat(:,1)*1000000; %conversion
yData=Dat(:,2);%
r =3.4; % distance from finger to tip
x=[100 27 0.02]; % Input parameters
F1=@(x,xData)(x(1).*(r^3          .*          xData.^(-4).*          exp(-
m.*r^2./(2.*kB.*x(2).*xData.^2))))+x(3); % The fit for one Boltzmann

[x,resnorm,~,exitflag,output] = lsqcurvefit(F1,x,xData,yData)
```

```
hold on;
plot (xData,yData,'.',xData,F1(x,xData));
hold off;
max=1/((4*kB*x(2))/(m*r^2))^0.5
%%Section 4
x1=[20 105 800 0 0.0];
lb=[0 0 0 0 0];
%x1(3)=a1(fitting parameter see Yabushita  JCP 129 044501 2008 doi:
%10.1063/1.2953714)
Smb1                        =@(x1,xData)(x1(3).*(r^3.*xData.^(-4)).*exp((-
m.*r^2)./(2*kB.*x1(1).*xData.^2))+x1(5)); % Fit for individual Boltzmann
that makes up the first Term
Smb2=@(x1,xData)(x1(4).*(r^3.*xData.^(-4)).*exp((-
m.*r^2)./(2*kB.*x1(2).*xData.^2))+x1(5)); % Fit for individual Boltzmann
that makes up the second Term
S=@(x1,xData)(((x1(3).*((r^3.*xData.^(-4)).*exp((-
m.*r^2)./(2*kB.*x1(1).*xData.^2))))+(x1(4).*((r^3.*xData.^(-4)).*exp((-
m.*r^2)./(2*kB.*x1(2).*xData.^2)))))+x1(5)); % Sum of the two Boltzmann
Terms
[x1,resnorm,~,exitflag,output] = lsqcurvefit(S,x1,xData,yData,lb)
hold on; % Fit settings
figure,plot(xData,yData,'.',xData,S(x1,xData),xData,Smb1(x1,xData),xDat
a,Smb2(x1,xData));
hold off;
```